UNIVERSITY OF CALIFORNIA,
IRVINE

Advanced Polymeric Materials via Manipulation of Dynamic Molecular Interactions

DISSERTATION

submitted in partial satisfaction of the requirements
for the degree of

DOCTOR OF PHILOSOPHY

in Chemistry

by

James A. Neal

Dissertation Committee:
Professor Zhibin Guan, Chair
Assistant Professor Shane Ardo
Professor Elizabeth R. Jarvo

2018

DEDICATION

To

Hanna and Ellie

I am so lucky to have you both

To

the Rest of My family

Mom, Dad, Smom, Zach, Eli, Joe, Jamie, and Natalie

I am lucky to have you too

TABLE OF CONTENTS

CHAPTER 1: Dynamic Chemical Bonds in Advanced Materials

1.1 The Background of Advanced Materials

1.2 Self-Healing Materials

1.3 Tunable Materials

1.4 Gradient Materials

CHAPTER 2: Enhancing Mechanical Performance of a Covalent Self-Healing Material by Sacrificial Noncovalent Bonds

2.1 Introduction

2.2 Results and Discussion

CHAPTER 3: Tuning Dynamic Mechanical Response in Metallopolymer Networks through Simultaneous Control of Structural and Temporal Properties of the Networks

3.1 Introduction

3.2 Results and Discussion

CHAPTER 4: Large Continuous Mechanical Gradient Formation via Metal–Ligand Interactions

4.1 Introduction

4.2 Results and Discussion

CHAPTER 5: Progress Towards Silyl Ether Vitrimers for Commodity Polymers

5.1 Introduction

5.2 Results and Discussion

LIST OF FIGURES

LIST OF TABLES

LIST OF SCHEMES

ACKNOWLEDGMENTS

First, I would like to thank Professor Zhibin Guan for giving me an opportunity to join his exciting lab. I had identified his lab before arriving at UC Irvine and his mentorship and support throughout my Ph.D. studies were more than I could have hoped for. His scientific stamina, discipline, and drive to explore new, challenging problems were an absolute inspiration. These principles, combined with Professor Guan's high standards, are what pushed me toward a successful Ph.D. career and I am extremely grateful. I would also like to thank my thesis committee: Professor Shane Ardo and Professor Elizabeth R. Jarvo. Shane, your kindness and passion for science should be a model for all aspiring scientists to follow. Liz, your mentorship early in my Ph.D. career through Mech 1 and Advancement was pivotal in my growth as a chemist, thank you.

I would also like to thank members from the Guan Group. First, Dr. Davoud Mozhdehi, Dr. Olivia Cromwell, and Dr. Jaeyoon Chung. I could not think of a better mentorship group to have as an incoming Ph.D. student. Your patience, support, and comedic relief helped more than I can express. Davoud, you are the smartest person I have ever met, and I feel fortunate to have met you at a time when you tolerated first years. Otherwise the rest of our beautiful relationship would not have been possible. Olivia, you will always be my chemistry mom, thank you for taking such good care of me: from the very beginning to hopefully decades into the future. Jae, I feel like I can go to you with any problem, science or not, and get a thoughtful response. Not much more I could ask for from a great friend. To you three, I could write endlessly about your impacts on my career and life, but I don't have the space, call me anytime. Nathan Oldenhuis, Justin Crumrine, Mark Johsnon, Tobias Friedberger, Miguel

Fernandez, Hanxiang Zeng, and Yi-Xuan Lu, I was the only baby in lab when I met you and thanks for taking me under your wings.

To the younger students of the Guan Lab, I hope you know I did my absolute best to provide guidance, support, and humor to our lab. Good luck with the rest of your careers, only call me if you've exhausted all other options (mostly kidding). Alex, I view you as my younger brother. Billy, you're one of a kind and I appreciate that. Dongchu, good morning, I am glad you were on my side of the lab, I would have gotten sick of everyone else. Hurik, I am so happy that you joined the Guan Lab, working with you kept me sane. Chase, good luck on all your silly endeavors.

Thank you to Emil Samson for your enthusiasm and passion joining the Guan Group and working with me. Training and working with you was, clearly, the highlight of my Ph.D. career. I have never felt more accomplished than when you were accepted to graduate school. You deserve everything that comes your way in science and I am so happy that I could be a part of your journey. Thank you, sir.

Thank you to all my friends and peers in the Chemistry Department at UC Irvine. Thank you for your patience and help, I took more, than I gave back. Sorry. Thank you to the UCI chemistry facilities directors and staff, including Dr. Phil Dennison, Dr. Dima Fishman, Tenley Dunn, Jaime Albano, and Laura Donaldson.

Last, but not least, thank you to my family. Hanna Neal, I could not have done any of this without you. You are my rock, you mostly put up with my long nights, lack of weekends, and fits of anxiety. I could write 200 pages about just your role in my Ph.D. career. Thank you for agreeing to be pregnant while I was in grad school. Wow. Ellie, you just caught the tail end of this thing, and you should feel very fortunate for that. I love you more than I thought possible. Try to grow up slow. Mom, I love that you are my #1 cheerleader and you know it. Dad and rose, thank you for making me the man I am today. Zach, Eli, Joe, Jamie, and Nan; you guys can make me laugh like no one else can, I needed that a lot throughout the process. Thank you.

CURRICULUM VITAE

JAMES A. NEAL

6215 Adobe Circle (206)-384-8329
Irvine, CA 92617 neal.jamesa@gmail.com

WORK EXPERIENCE

Graduate Student Researcher – Guan Research Group *September 2013 – August 2018*
University of California, Irvine: Irvine, CA

- Designed, synthesized, and characterized multi-functional 'smart' polymeric materials (self-healing, mechanical property tunability, mechanical gradient formation, thermoplastic toughening)
- Connected molecular properties of dynamic crosslinks to performance of bulk materials
- Combined small molecule synthesis of designer monomers with various polymerization techniques (RAFT, free radical, ATRP, ROMP, etc.) for next-gen materials
- Investigated the structure/property relationship of metal-ligand dynamic crosslinks to widely tune mechanical properties and create mechanical gradients spanning 100-fold difference in stiffness
- Employed sacrificial hydrogen bonds to drastically improve the toughness of a self-healing material
- Supervised and trained PhD and undergrad students while PI completed 1-year international sabbatical
- *Technical skills:* organic synthesis, polymerizations, rheology, DMA, TGA, DSC, Instron, NMR, GC-MS, FTIR
- Performed laboratory maintenance of GPC, auto-column, TGA, DSC, rheometer

Associate Engineer – SpaceX *January 2017 – March 2017*
Hawthorne, CA

- Participated in competitive 12-week internship program
- Designed and implemented the evaluation of epoxy adhesives for next-gen pressure vessels
- Initiated a plan to bring pressure vessel supply chain in-house to minimize cost and maximize efficiency
- Directed a team of technicians to prioritize and complete tasks

EDUCATION AND TRAINING

Ph.D. Candidate, Chemistry, *University of California, Irvine, Irvine, CA* *August 2018*
Thesis Advisor: Professor Zhibin Guan GPA 3.98
Thesis: Advanced Polymeric Materials via Manipulation of Dynamic Molecular Interactions

B.A. with Honors, Chemistry, *Willamette University, Salem, OR* *May 2012*
Advisor: Professor Sarah R. Kirk, Minor in Physics GPA 3.7
Thesis: The Design and Synthesis of Small Molecule Ion Channel Blockers

PUBLICATIONS

Neal, J.A.;* Oldenhuis, N.J.;* Novitsky, A.L.; Samson, E.; Thrift, W.J.; Ragan, R.; and Guan, Z. “Large Continuous Mechanical Gradient Formation via Metal-Ligand Interactions” [co-first author, commun.] *Angew. Chem. Int. Ed.* **2017**, 56, 15575-15579.

Neal, J. A.;* Mozhdehi, D.;* Gringy, S.; Cordeau, Y.; Ayala, S.; Holten-Anderson, N.; Guan, Z. “Tuning Mechanical Response in Self-Healing Metallopolymer Networks Through Metal-Ligand Complex Geometry and Exchange Dynamics” [co-first author, article] *Macromolecules* **2016**, *49*, 6310-6321.

Neal, J. A.; Mozhdehi, D.; Guan, Z. “Enhancing Mechanical Performance of a Covalent Self-Healing Material by Sacrificial Noncovalent Bonds” [article] *J. Am. Chem. Soc.* **2015**, *137*, 4846-4850.

PRESENTATIONS

- Frontier in Soft Matter and Macromolecular Networks, San Diego, CA, September 2017 [oral]
- 133rd BASF International Summer Course, Ludwigshafen, Germany, August 2017 [Poster]
- Gordon Research Conference Bioinspired Materials, Les Diablerets, Switzerland, June 2016 [Poster]
- UC Irvine, Associated Graduate Students Symposium, Irvine, CA, April 2016 [Oral]
- American Chemical Society National Meeting, San Diego, CA, March 2016 [Oral]
- International Conference on Self-Healing Materials, Durham, NC, June 2015 [Oral]
- UC Irvine Graduate Symposium, Irvine, CA, March 2015 and October 2016 [Oral]
- Student Scholarship Recognition Day, Willamette University, April 2012 – Keynote Speaker [Oral]
- Murdock College Science Research Conference, Seattle University, November 2011 [Poster]

AWARDS AND HONORS

University of California, Irvine

- Allergan Graduate Research Fellowship (Oct. 2016): excellence in research and unusual future promise
- Michael E. Gebel Award (May 2015): excellence in graduate research and community service
- GAANN Fellow (Aug. 2013 – May 2015): given to students of merit with financial need
- Department of Chemistry Travel Fund Award (March 2015)

Kindercare Learning Center

- Rookie of the Year (2012): for outstanding classroom leadership by a new teacher

Willamette University

- Peterson Chemistry Scholarship (2011): dedication to chemistry, academics, and pursuit of PhD
- Willamette University Merit Scholarship (2011): earned for sustained academic merit
- Nancy K. Detering Waechter Chemistry Scholarship (2010): brilliance in organic chemistry
- OICF Bend Research Scholarship (2009, 2010): superior organic chemistry laboratory technique
- Willamette University Academic Leadership Award (2008 – 2010): overall academic excellence

TEACHING EXPERIENCE

Undergraduate Research Mentor	*September 2015 – August 2017*
Guest Lecturer: UC Irvine (graduate and undergraduate courses)	*Winter, Spring 2016*
Graduate Teaching Assistant: UC Irvine	*January 2013 – August 2018*
Private Tutor: Irvine, CA	*October 2015 – May 2016*
Preschool Teacher: Kindercare Learning Center	*September 2012 – June 2013*

ADDITIONAL EXPERIENCES

- *Guan Research Group Safety Representative* – Coordinated with EH&S/Cal-OSHA regarding safety issues
- *Guan Research Group Collaboration* – Pursued and negotiated with private company for instrument use
- *133rd International Summer Course: BASF* – Program to learn about the strategies for innovation at BASF
- *TA Instruments Training Courses* – Attended lecture series on TGA, DSC, DMA, Rheology
- *Mentoring Excellence Program: UC Irvine* – Six modules focusing on skills related to mentorship
- *Chemistry Outreach Program: UC Irvine* – Promote Science to students through chemistry demonstrations
- *Affiliations:* American Chemical Society

ABSTRACT OF THE DISSERTATION

Advanced Polymeric Materials via Manipulation of Dynamic Molecular Interactions

By

James A. Neal

Doctor of Philosophy in Chemistry

University of California, Irvine, 2018

Professor Zhibin Guan, Chair

Tremendous synthetic advances in the fields of organic and polymer chemistry have created new opportunities to design advanced, new polymeric materials. Empowered with a suite of advanced synthetic tools, researchers have looked to nature for new inspiration in materials design. Nature has provided a near endless stream of ideas to draw upon for new advanced materials. The goal of this dissertation is to use lessons learned from nature to create cutting-edge, advanced polymeric materials that rely on dynamic molecular interactions. The thesis begins, in Chapter 1, with the background of each individual chapter, including both a guiding principle from nature, as well as, examples of selected previously published work in the field.

In Chapter 2, I draw on lessons learned from the human bone to incorporate sacrificial hydrogen bonds into a covalently crosslinked self-healing material. This work addresses the long-standing challenge in the field of self-healing materials by combining robust mechanical and efficient self-healing properties. Specifically, the toughness of the material is increased 7-fold.

In Chapter 3, I draw from the observation that nature displays remarkable ranges in mechanical properties from simple building blocks to create a widely tunable metallopolymer system. Specifically, the mechanical performance of the system is tuned from viscous oils to stiff plastics by careful selection of type and amount of added metal. This behavior is explained via ligand exchange mechanism, where associative and dissociative mechanisms are leveraged to achieve widely different properties.

In Chapter 4, I imitate the mechanical gradients commonly observed in nature that protect biological materials from damage. Through a sophisticated understanding of metal-ligand crosslinks, I develop a novel approach to generating stiffness gradients in polymeric materials. The result is a mechanical gradient that spans over a 200-fold difference in stiffness.

In Chapter 5, I attempt to duplicate the impressive moldability of silicate glass in covalently crosslinked polymer networks. Towards this goal, I have identified the silyl ether motif as a potential key to creating commercially-relevant vitrimer materials. If successful, these vitrimeric materials could replace thermosets in a variety of applications.

Chapter 1: Dynamic Chemical Bonds in Advanced Materials

1.1 The Background of Advanced Materials

1.1.1 A brief history of synthetic plastics

The first synthetic polymer was developed in 1907 by Leo Baekeland.[1] This first plastic was a thermosetting resin that was obtained through the condensation reaction of phenol and formaldehyde. Dubbed “Bakelite”, this material had the unique properties of being highly resistant to electricity, heat, and chemical reactions. Bakelite was first commercially used as an electrical insulator, but its commercial uses quickly grew to include various parts of telephones and radios, billiard balls, and kitchenware. Bakelite was clearly the first step of ushering in the Age of Plastic, but World War II was the driving force needed to expand the plastic industry into what it is today.

In World War II, the rapid amount of building put an unsustainable burden on natural resources such as cellulose and natural rubber. When a new building material was clearly needed, plastics took center stage. Synthetic plastics have the desirable traits of being light, tough, and made from cheap, oil-derived feedstocks. In the United States during World War II, the plastics industry grew 3-fold.[2] Major players included Nylon, a “synthetic silk,” and plexiglass, a more durable substitute for glass. The uses for Nylon included parachutes and body armor, while plexiglass was used for aircraft windows. The large amounts of money and research efforts that were invested during this time, along with the wide variety of chemical feedstocks, resulted in an industry where a material could be custom manufactured and tuned based on the desired end-use properties. After the war, the fruits of this work were released on the public.

With the technical ability to control the properties of plastics in hand, and the plastics manufacturing infrastructure already in place, the post-World War II climate left plastics in a great position to grow. An executive at the time summed up the situation well, after the war "virtually nothing was made of plastic and anything could be."[2] As a result, plastics quickly took the place of previously established and ubiquitous materials. For example, plastics replaced steel in cars, wood in furniture, and paper in packaging.

As the use of plastics in society grew, they were most often used as a light-weight, inexpensive replacement for insulation and structural applications. That said, due to the tunability and wide-range of components that plastic can contain, the next advancement for the plastics industry is the development of multi-functional and advanced materials. To identify opportunities for growth in the field of advanced materials, we often turn to nature for inspiration.

1.1.2 Using nature to inspire the next generation of advanced materials

Polymer science is no longer restricted to the "common" plastics of the previous generation. Beginning in the 1970s, the idea of biomimetic chemistry began to take hold. Ronald Breslow defined biomimetic chemistry as "the branch of organic chemistry which attempts to imitate natural reactions and enzymatic processes as a way to improve the power of organic chemistry."[3] This same concept of borrowing from nature fits perfectly with the field of polymer science. Constant developments in the synthetic control over polymeric architectures have radically changed the possibilities of these materials and pushed the boundaries so far that advanced materials hardly resemble their Bakelite ancestors from 100 years ago.[4]

Using nature as inspiration provides a near endless stream of ideas to draw upon for new advanced materials. This inspiration can come from the visual observation of a surface, as in the structure color relationship of the butterfly wing.[5] On the other hand, inspiration can come from observing a function and researchers can creatively mimic this function through a completely different pathway, as is the case with self-healing synthetic systems.[6] The work in this dissertation uses lessons learned from nature to create cutting-edge, advanced polymeric materials.

For the remaining sections in this introduction, we will cover the background on each individual chapter. This background will contain both a guiding bioinspired principle from nature, as wells as, examples of meaningful, previously published work in the field. These topics will include: for chapter 2, self-healing materials; for chapter 3, tunable materials; for chapter 4, gradient-containing samples; for chapter 5, vitrimer materials.

1.2 Self-healing Materials

1.2.1 Biological self-healing mechanisms

The ability to repair damage is one of nature's most important traits. The increased lifespan that comes from damage mitigation allows organisms the opportunity for further reproduction. Biological healing typically follows the same pathway regardless of specific organism (Figure 1.1, right).[7] First, an injury triggers the initial response and the resulting wound is addressed with an immediate inflammatory action. This blood clotting and inflammation is used to bring the cut interfaces together and limit bacterial infection.[8,9] Next, over the course of days, cell growth occurs to fill any missing material and begin the healing process.[10] Finally, the last stage of healing is matrix remodeling which returns initial function to the damaged area.

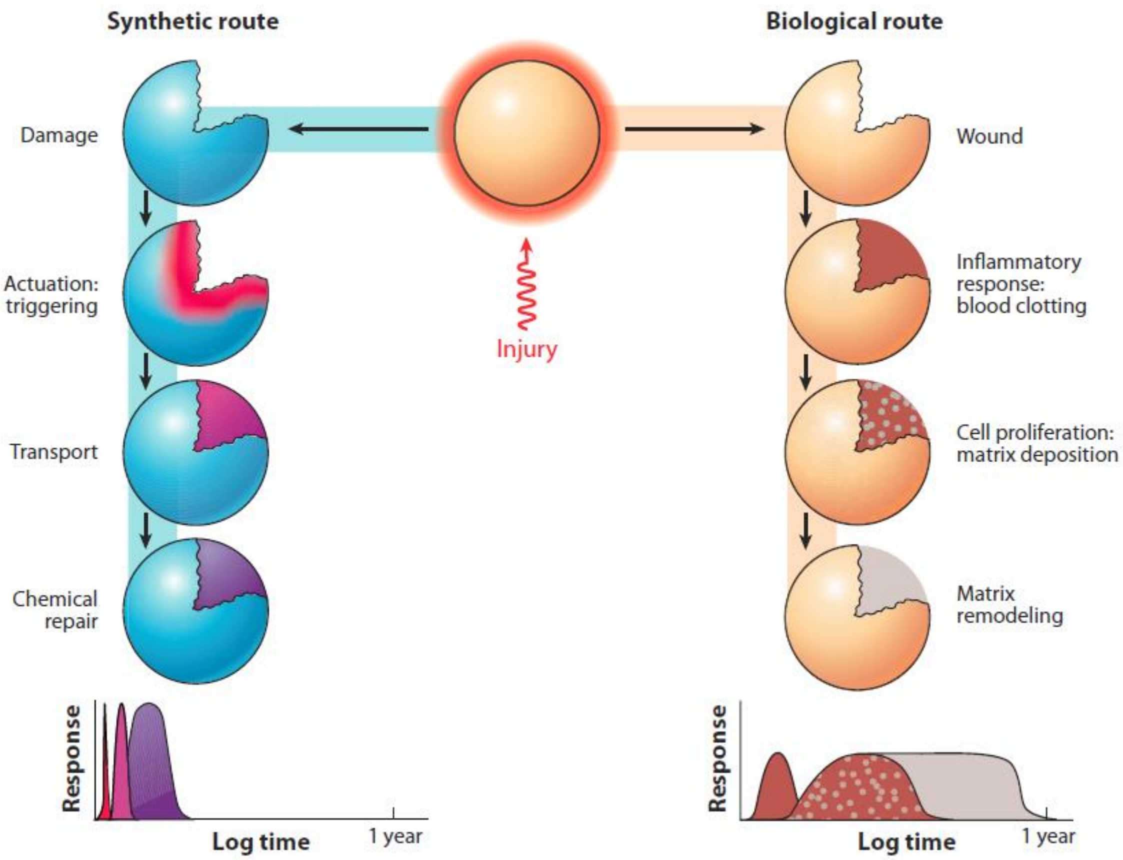

Figure 1.1 Comparison of healing in synthetic and biological systems. Both systems undergo an initial, intermediate, and long-term approach. Typically, synthetic efforts aim to speed up the process compared to the biological template. Reprinted from ref.[7]

Synthetic materials mimic nature's ability to heal through a drastically different mechanism. Synthetic materials that can heal are attractive due to the improved safety and durability that they would possess. That said, the complexities of nature are seemingly impossible to be closely imitated. Instead, researchers have often looked to the lessons of nature for inspiration (Figure 1.1, left). As in the biological pathway, the healing of synthetic systems is triggered by an initial damage event that creates an active site in the material. Next, material transport occurs either through polymer chain relaxation or the flowing of monomers. Finally, chemical repair can occur through a host of different mechanisms. Unsurprisingly, due to the synthetic flexibility of modern-day organic and polymer chemistry, researchers have used a wide variety of chemical motifs for healing. Additionally, scientists are able to control the rate of healing based on application, rather than settling for the long healing times of biological systems.

A long-standing issue with the current state of synthetic self-healing materials is the combination of efficient healing and robust mechanical properties (*vide infra*). Nature, too, has been tasked with this challenge of achieving improved mechanical properties while working under strict design rules. One route that nature commonly uses to improve mechanical properties is the incorporation of sacrificial non-covalent bonds.[11] In biological systems, sacrificial non-covalent bonds are used to efficiently dissipate large amounts of energy through bond cleavage.[11–13] That said, the reversible nature of these bonds, means that no permanent damage is done. This imparts a combination of high toughness and reversible recovery to the specific material.

Sacrificial bonds are observed in the protein *Titin*. *Titin* is an enormous 3 MDa protein, made up of 244 individually folded protein domains, that is known to be responsible for the elasticity of muscle.[14] *Titin* is especially known for its mechanical properties being strong, stretchable, and tough. It is made up of immunoglobulin and fibronectin-III modules. A tremendous amount of work has been done to understand the toughening mechanism of the *Titin* protein. Through atomic force microscopy (AFM),[15] protein nanomechanics,[16] and computational work,[17] the load bearing protein domains have been identified. Specifically, immunoglobulin I27 has been identified as a unit that directly impacts the mechanical behavior of *titin* (Figure 1.2). I27 contains nine, load-bearing hydrogen bonds. These cooperative hydrogen bonds are split between beta strand interactions A/B and A'/G. As force is applied, the rupture of these hydrogen bonds, along with the unveiling of hidden length, results in a massive amount of energy dissipation.[18] This lesson of programming non-covalent interactions is also observed in the toughening of bone.

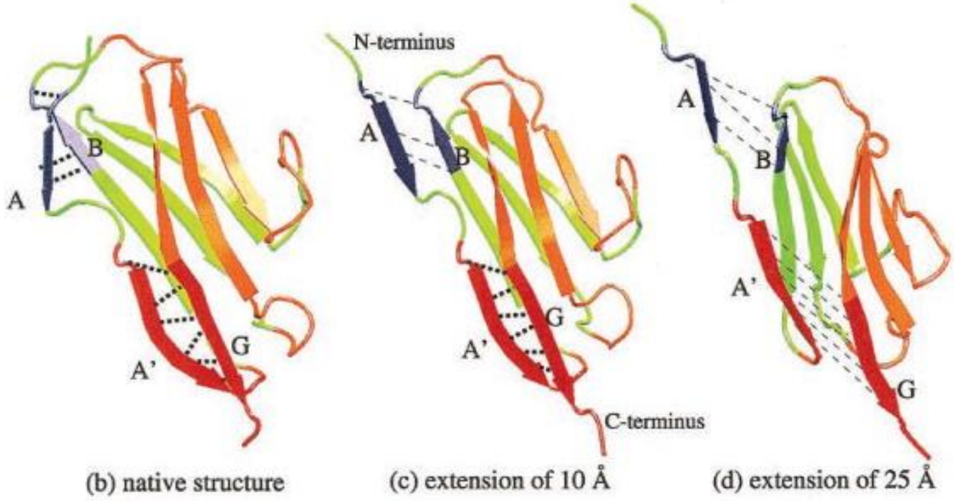

Figure 1.2 Secondary structure of immunoglobulin domain I27. Three different snap shots during force induced unfolding are depicted: (b) native structure, (c) 10 Å unfolding, (d) 25 Å unfolding. Reprinted from ref.[18]

Bone is another example of biological systems using non-covalent bonds to boost mechanical properties.[19] The matrix of bone is made up of 90-95% collagen fibers.[20] These collagen fibers consist of amino acids with the secondary structure of a triple-helix. While teasing out the exact mode of energy dissipation is difficult, research has been done to show the existence of calcium-mediated sacrificial bonds.[19] Hansma and co-workers have shown that bone consists of both mineralized collagen fibrils and a non-fibrillar matrix that acts as a glue to hold the fibrils together (Figure 1.3). Their work highlights the importance of Ca^{2+} ions and points to their likely role in the “glue” of bones (Figure 1.3a). Specifically, that many weak sacrificial bonds between Ca^{2+} ions and biopolymers cooperate to achieve a non-catastrophic toughening mechanism (Figure 1.3b). The lessons from biological systems in the case of toughening materials, as observed in *titin* protein and bone, is a concept that should stay in the forefront as we begin to study the attempts that researchers have made to achieve self-healing, synthetic materials.

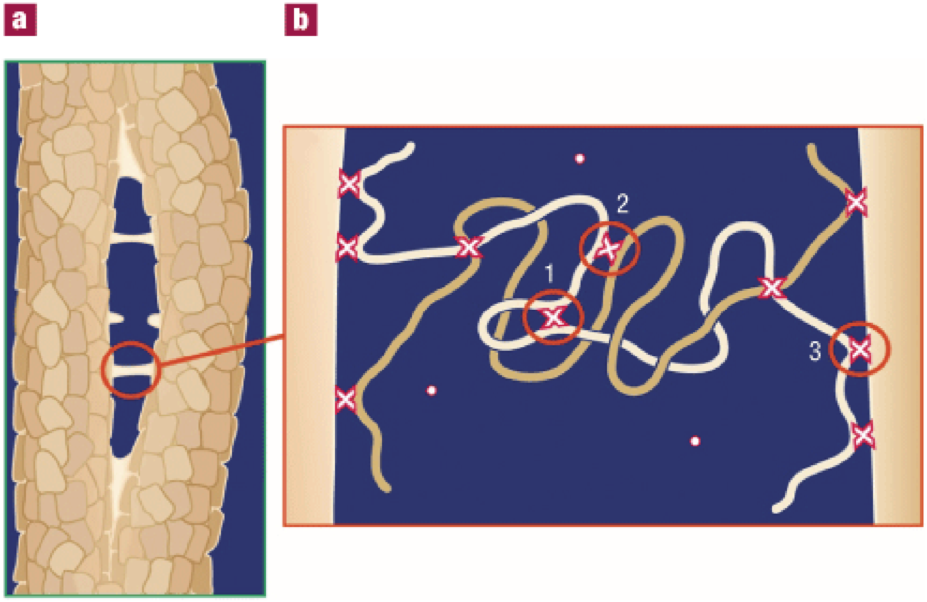

Figure 1.3 Sacrificial bonds in bone. Hypothesized role of calcium-mediated sacrificial bonds as the (a) glue between collagen fibrils. (b) Potential sacrificial bond formation can occur between (1) a single biopolymer, (2) different biopolymers, or (3) a polymer and a collagen fibril. Reprinted from ref.[19]

1.2.2 The landscape of self-healing materials

Biological materials possess an increased lifespan and resilience to damage due to their ability to spontaneously self-repair. In contrast, most current and commonly-used synthetic materials cannot heal. Mimicking nature's ability to heal would result in manufactured materials with improved durability and safety. A variety of systems have been developed to recover mechanical integrity after structural failure. Again, while this function of healing is mimicking nature, the actual mechanism is completely different. Most broadly, self-healing materials can be divided into two main categories: extrinsic and intrinsic self-healing (Figure 1.4).[7,21] Looking deeper into these categories, extrinsic self-healing systems rely on the availability of unreacted molecules to flow to an active site and react upon a damage event. Extrinsic self-healing materials are typically separated into capsule-based or vascular-based self-healing. Alternatively, intrinsic self-healing relies on functionality already linked to the polymer. These can include thermally reversible reactions,[22] hydrogen bonding,[23] and metal-ligand interactions.[24] These classes of self-healing materials has their own pros and cons.

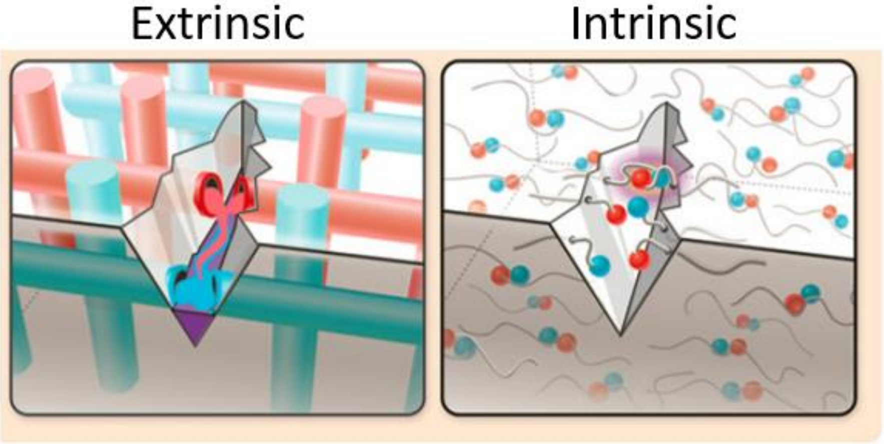

Figure 1.4 Two broad approaches to self-healing materials. They are separated into extrinsic and intrinsic self-healing. Adapted and reprinted from ref.[7]

1.2.3 Capsule-based self-healing materials

In 2001, White *et al.* developed an early example of a self-healing, capsule-based system. Here, a catalyst was embedded into the material, along with monomer-containing microcapsules (Figure 1.5).[25] When the capsule was broken due to force, the monomer is released and flows into voids in the material (Figure 1.5a). As the unreacted monomer flows, it encounters the imbedded catalyst, leading to polymerization.

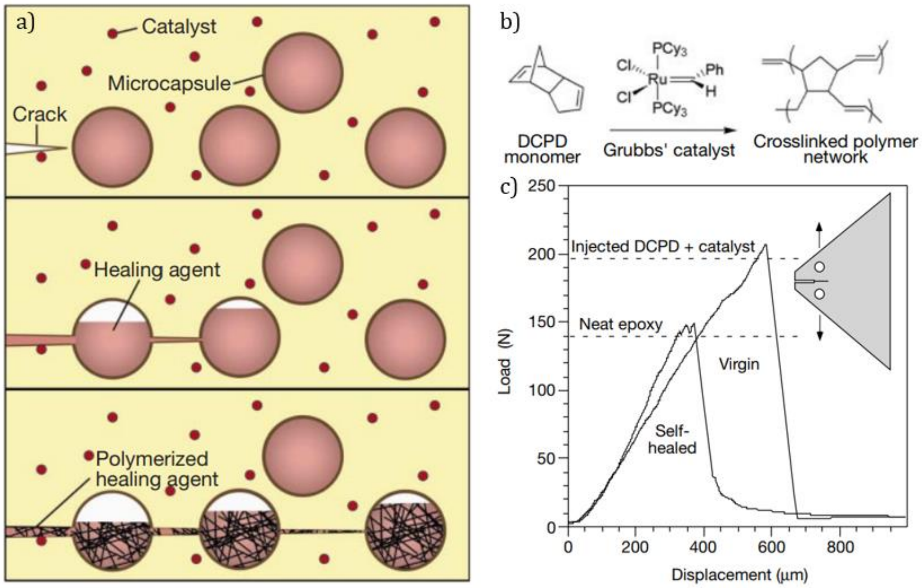

Figure 1.5 A capsule-based self-healing material. (a) The material relies on the release of healing agent (monomer) via crack propagation to fill cracks through polymerization. (b) The healing agent reaction is the ring-opening metathesis polymerization of DCPD via Grubb's catalyst. (c) Self-healing analysis of the epoxy-based self-healing system showing 75% recovery of toughness. Adapted and reprinted from ref.[25]

In this first example of a capsule self-healing system, the researchers imbedded monomer and catalyst into a commercially-available epoxy matrix. Specifically, the material relied on the highly exothermic ring-opening metathesis polymerization of dicylopentadiene (DCPD). DCPD was polymerized with Grubb's first generation catalyst to yield a crosslinked filler upon damage (Figure 1.5b). Overall, the material was able to recover 75% of its initial toughness.

A major benefit of the capsule-based self-healing system is the autonomous nature of damage recognition. Due to the dispersed nature of healing agent throughout the material, microcracks can quickly be filled before propagation or catastrophic failure can occur. That being said, a drawback of most capsule self-healing materials is the reliance on a sensitive, and expensive, catalyst to be incorporated throughout the system. First, this makes the material prohibitively expensive for most applications. Second, these catalysts usually have a limited lifetime that is not on the order of commercial relevance.

1.2.4 Vascular-based self-healing materials

As previously mentioned, self-healing vascular systems are similar to capsule-based materials because they both typically contain unreacted monomer. In vascular systems, unreacted monomer is delivered to damaged sites through hollow tubes or channels in the material, reminiscent of how blood travels through the human body. This flow of unreacted monomer can be driven by capillary action, gravity, or a separate pump.[7] A major drawback of most vascular designs is the demanding front-end engineering that is need to design a hollow network through the material. Additionally, when damage occurs, the vascular design can be blocked, shutting down the flow of monomer and resulting in a one-time healable material. Finally, many vascular self-healing systems cannot heal large damage due to the complete destruction of the vascular network and the inability for healing agent to span the newly formed gap.

An initial proof-of concept for vascular-based self-healing materials was performed in 1996 by Carolyn Dry.[26] Here, the researcher filled glass pipets with a one-component cyanoacrylate adhesive and they were cured within an epoxy matrix. This extremely simple design led to the release of the healing agent upon damage to the glass pipets. Through optical microscopy, bend tests, and impact tests the researcher was able to show the flow of healing agent into the cracks and subsequent healing. Further work on this simple design was done to control the size of the healing agent reservoir,[27] the type of healing agent,[28] and the strength of the glass which creates the vascular network.[27] Since these initial studies, more complex vascular networks have been designed.

In 2014, White and coworkers created a vascular self-healing material that can heal large-scale damage (Figure 1.6).[29] Here, a pump was used to flow healing agents through a vascular network, in a similar manner to blood pumping through the human body. The key to this system was the use of a two-component, two-stage system. Upon damage, the two components mix to form a self-supporting gel to fill large scale damage. Over time, this gel continues to polymerize and solidify to restore 62% of the initial mechanical properties. The system is an exceptional example of biomimicry, as the gelation and polymerization stages closely mirror the cell proliferation and matrix remodeling of biological systems.

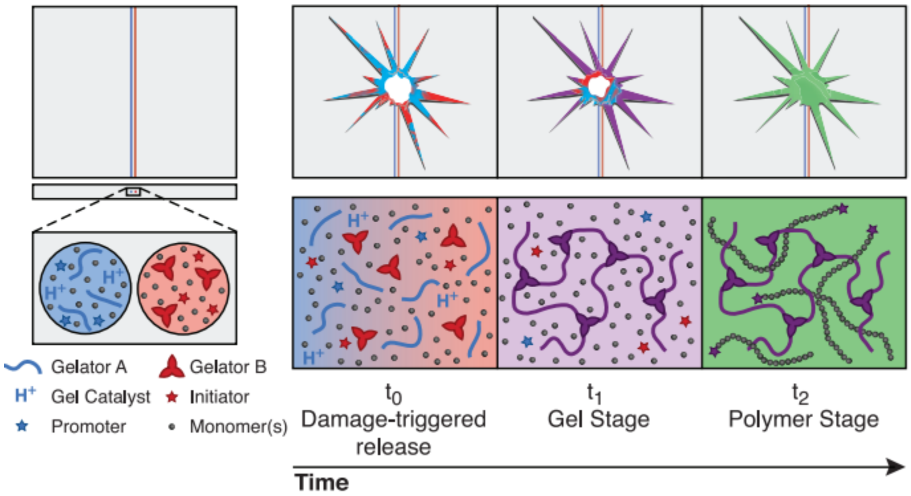

Figure 1.6 Large damage healing via vascular motif. Vascular self-healing system that relies upon a two-component, two stage cure. First, gelation occurs to fill a created void. Next, polymerization occurs to restore initial mechanical properties. Reprinted from ref.[29]

1.2.5 Intrinsic self-healing materials

Intrinsic self-healing materials rely on intrinsic molecular interactions already incorporated into the polymer system. This category of self-healing materials is the most broad and all encompassing. Some systems take advantage of relatively weak, but noncovalent bonding such as reversible hydrogen-bond[23,30] or metal-ligand[31,32] interactions to heal after mechanical failure. While other intrinsic self-healing systems rely on reversible, dynamic covalent that usually require large amounts of thermal or light energy to trigger healing to occur. Here, the selection of healing motif can be driven by the end-use of the material.

An early example of an energy-intensive, intrinsic self-healing system was designed by Wudl and coworkers.[22] A crosslinked material was designed based on the Nobel Prize winning, thermo-reversible Diels-Alder reaction (Figure 1.7). Specifically, a tetrafunctional furan monomer was combined with a trifunctional maleimide molecule (Figure 1.7a). Upon reaction, a highly crosslinked material, comparable to commercially-available resins, was formed. Then, upon heating to 150 °C for 15 min, the material depolymerized and began to flow. Subsequent cooling, reformed the crosslinks and recover the much of the initial mechanical properties (Figure 1.7b).

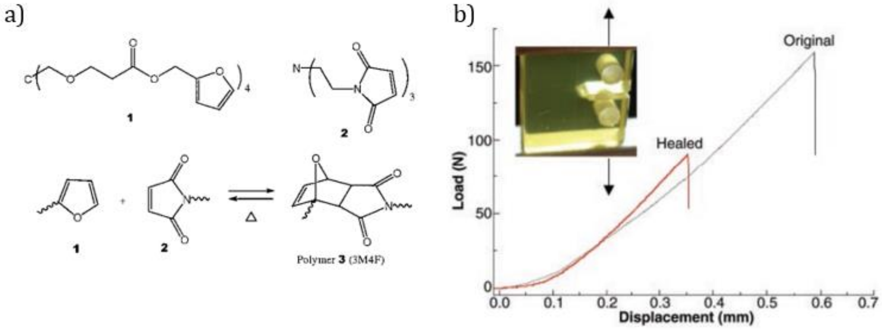

Figure 1.7 Intrinsic self-healing based on the Diels-Alder reaction. (a) Crosslinking reaction between multifunctional furan and maleimide molecules. (b) Mending efficiency measured by fracture toughness. Adapted and reprinted from ref.[22]

There are a couple major drawbacks associated with energy-intensive, intrinsic self-healing systems. These include the loss of material mechanical properties during healing. For example, when heat is applied to the Diels-Alder system, the material loses its structure due to depolymerization. Also, the high amount of energy needed for healing makes this system unrealistic for some applications due to limitations in surrounding environment. These issues are not reserved for only Diels-Alder based systems, but are also observed in metallo-polymer systems where high intensity UV light is used to promote self-healing.[33]

Another type of intrinsic self-healing systems relies on weaker, but easily reversible interactions. An early example of this relied upon hydrogen-bonding rich components to develop a self-healing rubber from supramolecular assembly (Figure 1.8a).[30] Here, researchers mixed varying amounts of urea containing molecules to create a hydrogen-bonding network. Upon damage, a statistical distribution of covalent and hydrogen-bonds are broken. This portion of broken hydrogen bonds are able to reassociate with other hydrogen-bond acceptors and donors when he material is brought back together. This resulted in a material that could be self-healed under moderate (40 °C) conditions. An important observation for this system, which holds true for many other low energy intrinsic self-healing materials, is the importance of polymer chain mobility for self-healing. Polymer chains must have enough thermal energy to be mobile and a driving force to interdigitate across a cut interface. This point is emphasized by the difference in healability based on time separated after damage (Figure 1.8b and Figure 1.8c).

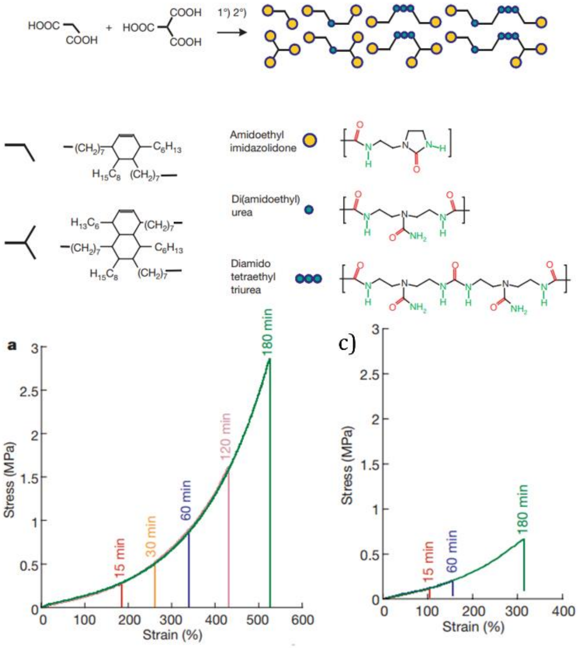

Figure 1.8 Intrinsic self-healing based on urea hydrogen-bonding. (a) Synthesis of urea components through condensation reaction of carboxylic acids and amines. (b) Self-healing behavior of bulk material after being cut and immediately brought back together. (c) Self-healing behavior of bulk material after being cut, kept apart for 6 h, and then mended. Adapted and reprinted from ref.[30]

The urea materials healability is greatly diminished when cut samples are kept separate for 18 h (Figure 1.8c) compared to less than 5 min (Figure 1.8b). This difference in healing is attributed to the need for a driving force to bridge the cut interface. When samples are initially cut with a razor blade, the polymer chains at the cut interface are pushed out of equilibrium. If the samples are quickly brought back together, polymer interdigitation will occur as the polymer chains relax. On the other hand, if the cut interface is not brought back together, equilibrium will be met by each cut piece separately and there will no longer be a driving force to promote healing when the cut samples meet again. This example underscores the importance of cut interfaces being brought back together immediately after damage occurs for low energy, intrinsically self-healing systems.

Another type of intrinsic self-healing material depends on incorporating a catalyst into a crosslinked material. This catalyst incorporation mirrors the previously mentioned capsule based healing systems. The key difference in this intrinsic system is that healing occurs through catalyst-backbone reactions, rather than a catalyst interacting with separately released monomers. In the Guan group, Grubbs' second generation ruthenium catalyst (G2) was incorporated into a cross-linked polybutadiene network (Figure 1.9a).[34] After catastrophic failure, the network recovered via cross-metathesis of olefin bonds across the cut interfaces, thereby healing the network. While the activity of G2 allowed the material to heal with pressure at subambient temperature, the network exhibited relatively weak mechanical properties with low initial stiffness and a maximum extensibility of only 100% (Figure 1.9b).

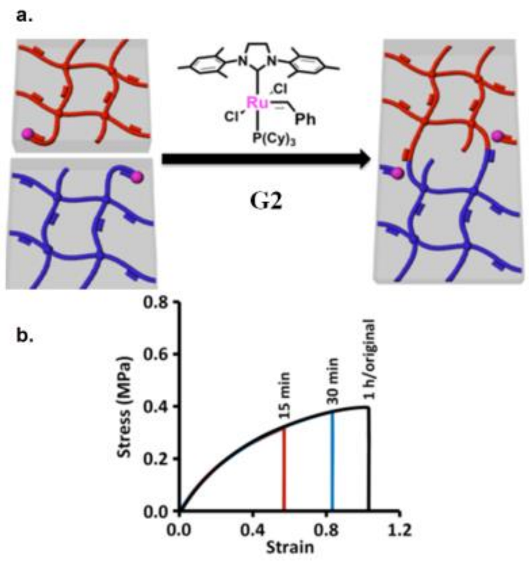

Figure 1.9 Olefin metathesis based healing of covalently crosslinked polybutadiene. (a) G2 mediated self-healing via olefin shuffling. (b) Mechanical properties of the self-healing network at various healing time points. Adapted and reprinted from ref.[34]

For many applications, it is beneficial for polymers to combine high initial stiffness (Young's modulus), extensibility (strain), and toughness (ability to dissipate energy). A common goal in the expanding field of self-healing polymers is to combine robust mechanical properties and healing efficiency under mild conditions.[35] Currently, many self-healing materials have been limited to relatively weak polymeric architectures due to the necessity for polymer chain mobility. Correspondingly, the weak mechanical properties of efficient self-healing materials limit their potential applications.[35,36] This fundamental challenge gives the opportunity to look to nature for inspiration to solve this issue.

1.3 Tunable Materials

1.3.1 Tunable materials in nature

The diversity of biological materials is breathtaking. Even more impressive, is the fact that this diverse family of materials are mostly made from proteins and protein composites. Proteins are the primary workhorse of living organisms and form the basis for biological materials such as hair, skin, bone, and cells.[37] This variety of strength, robustness, and adaptability is rooted in the 20 naturally-occurring amino acids that constitute the monomeric units of proteins. This lesson from nature, that diversity of mechanical properties can be achieved from a limited library of simple building blocks,[38] should be a guiding principle for synthetic organic chemists that too often design complex and overengineered systems to achieve a specific function.

The mechanical properties of proteins are governed by two main factors: amino acid incorporation and structural assembly. The relationship between protein structure and protein function is an extremely complex problem because a 200-residue protein can have 20^{200} different possible combinations of amino acids and each combination of amino acids will lead to various plausible conformational states.[39] While impressive work has been to address this challenge,[40] it is difficult to envision a time when *de novo* proteins can be designed by materials chemists for specific functions. Instead, it is likely wise to cede to nature's complex protein system and find guiding principles that can be adapted to fit synthetic systems.

A commonly observed route to tune the mechanical properties of biological materials is the fine control over weak molecular interactions. Hydrogen bonds are much weaker than traditional covalent bonds, but when combined, can see a tremendous increase in strength.

Keten and Buehler systematically calculated the shear strength for beta strands that contain different numbers of residues (Figure 1.10a).[41] They found that 3-4 hydrogen bonding units achieve the highest shear strength and additional residues offer limited strength due to a combination of shear localization and steric interference. The importance of this critical number of residues is echoed by how often 3-4 residues are used in common protein secondary structures (Figure 1.10b). For ∝-helices, β-sheets, and β-helices, nature takes advantage of this critical residue number. Mechanical properties can also be tuned by controlling the amount of incorporation of different specific amino acids.

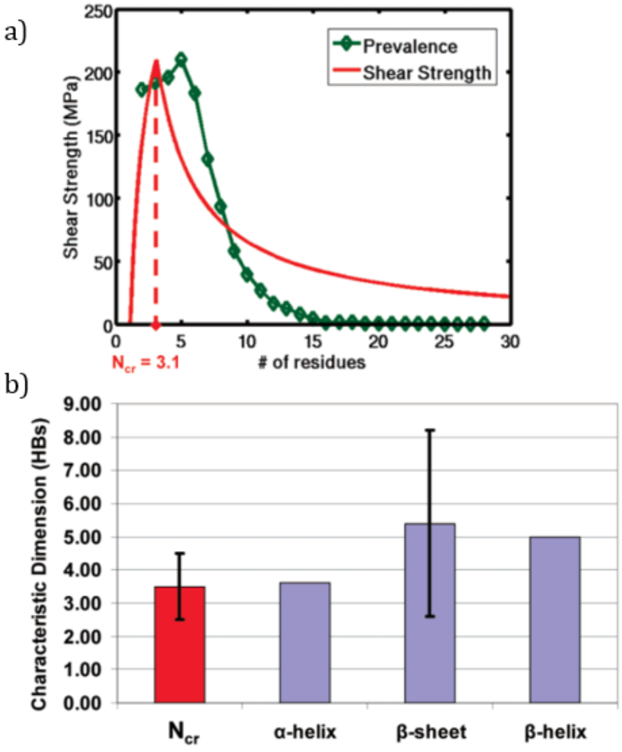

Figure 1.10 Relationship between number of residues and structure of protein. (a) Shear strength of beta-sheets as a function of strand length. (b) Average residue length of ∝-helices, β-sheets, and β-helices compared to the calculated critical residue length of 3-4. Adapted and reprinted from ref.[41]

The foot of a mussel is used to attach it to rock. The foot must be extremely robust to withstand the constant crashing of waves. Here, nature shows the ability to tune mechanical properties via incorporation of specific amino acids.[42] Specifically, the tip of the footpad (distal) is much stronger than the base (proximal) (Figure 1.11). To achieve this difference in stiffness, collagenous byssal proteins (precol) are incorporated in different amounts. The three main types of precol are preCol-NG, preCol-D, and preCol-P. PreCol-D is composed of polyalanine repeats separated by short glycine-rich spacers, while preCol-P is rich in glycine and proline and form loosely-packed coils. The distal region contains ~80% preCol-D, while the proximal region contains much more preCol-P (Figure 1.11b, inset). Tensile analysis of distal and proximal threads show that distal thread exhibits high Young's modulus, yield strength near 75 MPa, and strain-at-break 100% (Figure 1.11b). In contrast, proximal thread is much weaker (maximum stress near 25 MPa) and more extensible (strain-at-break 200%). This large difference in mechanical properties emphasizes the sophisticated tunability that biological materials employ to achieve robust function.

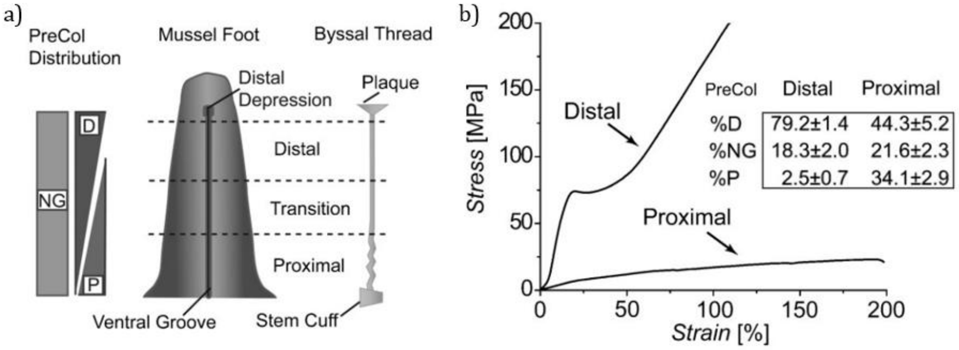

Figure 1.11 Analysis of mussel foot. (a) Schematic of foot and indication of preCol distribution. (b) Tensile properties of distal vs. proximal thread and (inset) analysis of preCol components via SDS-PAGE. Adapted and reprinted from ref.[42]

1.3.2 Tunable metallopolymers

Borrowing from biological systems, manufacturing of commercial products would be simplified if a host of properties and functions were accessible from a small library of starting materials. Towards this goal, a variety of motifs have been created to tune a material's response to static and dynamic load. Usually, these materials rely on control over reversible interactions, such as hydrogen bonding, ionic, or metal-ligand interactions.

Metal-ligand interactions are of unique interest for tunable materials because metal complexes are predictable, controllable, and the ligand exchange can be tuned based on type of metal ion and oxidation state. As a result, using metal-ligand complexes as crosslinks between polymer chains is an exciting opportunity for tunable materials. Based on these facts, one can envision the mechanical properties of a metallopolymer being closely tied to the identity of a metal center.

In 2016, Wegner and coworkers developed a cobalt-containing hydrogel that displayed drastically different properties based on the oxidation state of the cobalt atom (Figure 1.12).[43] Specifically, a 4-arm histidine-capped macromonomer was synthesized (Figure 1.12a). Upon dissolution in water and addition of cobalt salt, the material would be crosslinked (Figure 1.12b), but the strength of the crosslink was governed by the cobalt oxidation state. In this case, Co^{2+} weakly interacts with histidine, resulting in a viscous liquid. On the other hand, the histidine-Co^{3+} interaction is kinetically inert, and thus, an elastic solid is formed. Satisfyingly, under appropriate conditions, the material can be reversibly tuned between a solid and liquid state.

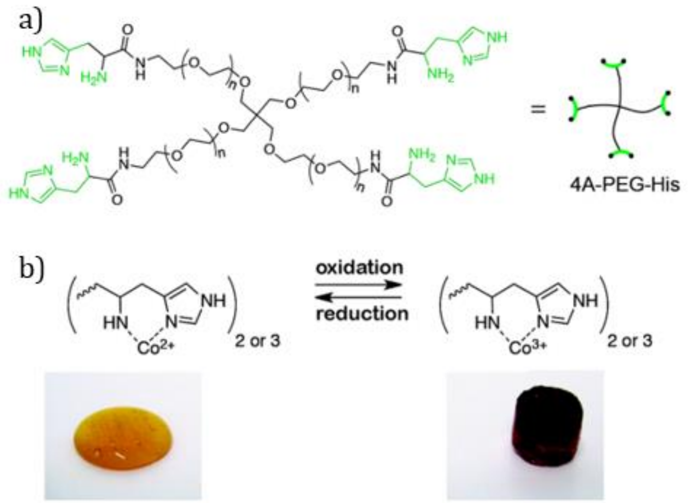

Figure 1.12 Tunable mechanical properties based on the oxidation state of cobalt salt. (a) 4-arm, histidine-capped macromonomer. (b) Cobalt-histidine interaction that governs the hydrogel strength. Co^{3+} results in elastic solid, while Co^{2+} results in a viscous liquid. Adapted and reprinted from ref.[43]

An early example of tuning a metallopolymer gel via metal crosslink was completed by Loveless *et al* in 2005.[44] Here, a poly(4-vinylpyridine) was dissolved in DMSO and a metal containing crosslinker was added (Figure 1.13). The mechanical response of this gel was tuned with two controls: identity of metal and steric bulk of crosslinker molecule. The identity of metal was either Pd or Pt, with Pd crosslinkers exhibiting faster exchange. The steric bulk of the pincer ligand on the difunctional crosslinker was tuned between methyl and ethyl, with the smaller substituent leading to a faster exchange rate. These two controls allowed for fine tuning of the storage modulus and dynamic viscosity of the solution because the gel properties directly reflect crosslinker kinetics. That said, a major drawback of this system, and the previous cobalt-containing system, is that they contain a large amount of solvent, limiting their potential applications.

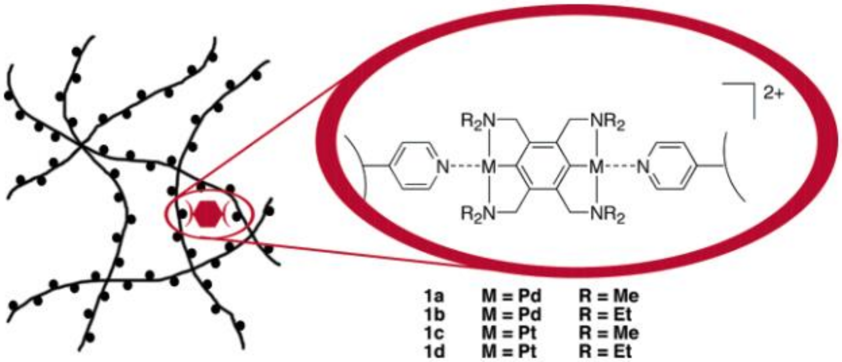

Figure 1.13 Tuning of a poly(4-vinylpyridine) gel through use of metal crosslinks. Exchange rate of metal crosslinks are tuned by identity of metal (Pd vs. Pt) and steric bulk on pincer ligands (Me vs. Et). Adapted and reprinted from ref.[44]

Polymeric materials that are crosslinked by metal centers typically rely on the incorporation of solvent to facilitate ligand exchange, as shown above. Removal of solvent often diminishes the ligand exchange rate, which in turn, requires external energy to facilitate ligand exchange. In 2011, Weder and coworkers designed a solvent-free material that was held together by metal complexes.[33] Specifically, telechelic 2,6-bis(1′-methylbenzimidazolyl)pyridine (Mebip) ligands were linked by a hydrophobic backbone and bound with Zn^{2+} salt (Figure 1.14a). Due to the combination of tridentate ligands and lack of solvent, stimulus is needed to facilitate ligand exchange and tune the material's response. Upon UV irradiation, the material quickly heats to 225 °C, providing enough energy for the metal complexes to dissociate (Figure 1.14b). In turn, the material begins to flow, drastically changing the bulk mechanical properties of the system. For sample $3\bullet[Zn(NTF_2)_2]_{0.7}$ the modulus decreases by one order of magnitude when heating from room temperature to 100 °C (Figure 1.14c). This Mebip-containing material is promising for a variety of applications because it does not contain a liquid phase. That said, this system requires high energy to modulate its mechanical properties and there is no ability to fine tune the mechanical response with UV light. More work must be done to combine the fine tuning of mechanical response that is achieved in the poly(vinylpyridine) system, but in a bulk material that does not have the drawbacks of a gel.

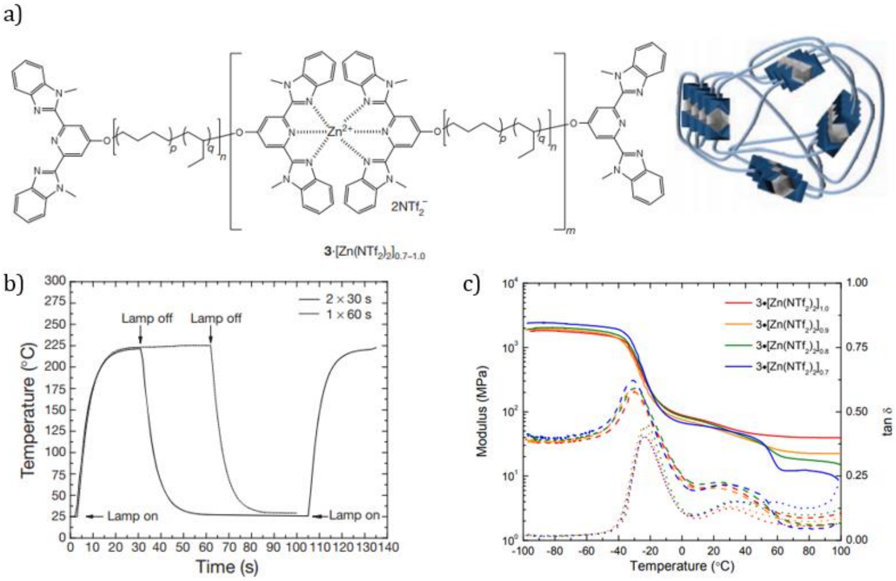

Figure 1.14 Solvent-free metallopolymer. (a) Structure of Zn^{2+} complex with telechelic Mebip ligand. (b) Surface temperature of 3•[Zn(NTF$_2$)$_2$]$_{0.7}$ upon irradiation of UV light as a function of time. (c) Modulus of Zn-Mebip materials as a function of temperature. Adapted and reprinted from ref.[33]

1.4 Gradient Materials

1.4.1 Gradient materials in nature

Biological materials must endure a constant onslaught of physical damage without loss of function to survive. These damages can come from a crashing wave, a predator, or can be self-inflicted during the pursuit of food. Regardless, nature uses creative solutions to mitigate the forces from these ubiquitous events. For example, stiffness gradients are observed throughout nature to minimize the buildup of force and catastrophic damage. A stiffness gradient allows for force to be distributed evenly across a wide area of material, thus minimizing stress on the system.[45] Another important benefit of natural gradients is the ability to connect dissimilar materials. If a strong and weak material are directly connected, they are likely to shear at that interface. However, if the material has no clear interface, but instead slowly transitions, the material is protected from this catastrophic event.

The beak, or jaws, of a cephalopod is its lifeline for survival. These marvels of biological engineering are responsible for the squid's and octopus' ability to penetrate the hard shells of crabs, clams, and other animals on the sea floor. The beak of the Humboldt squid represents one of the hardest and stiffest organic materials known (Figure 1.15a).[46] The connection of its stiff beak with its soft, pliable body is an amazing feat of nature. To understand how this is achieved, Miserez *et al* dissected the beak into various sections based on pigmentation and tested the mechanical properties via tensile testing. They observed an unmistakable gradient pattern where the heavily tanned section was most stiff, followed in stiffness by moderately tanned, light tanned, and untanned sections (Figure 1.15b). Overall, the observed difference in stiffness for these samples was 100-fold.

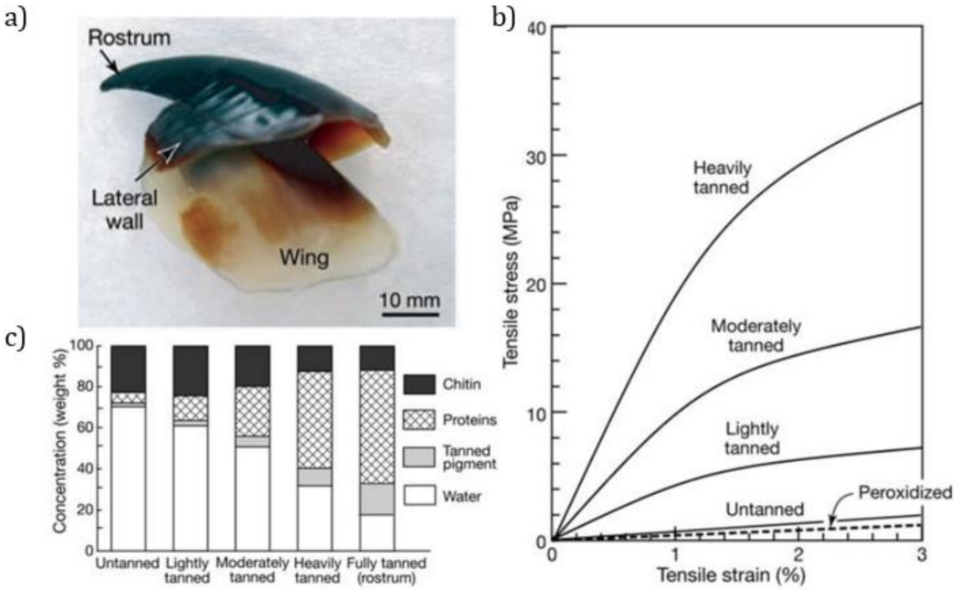

Figure 1.15 Analysis of Humboldt squid beak. (a) Side view of upper beak. (b) Tensile analysis of hydrated beak samples. (c) Gravimetric analysis of beak contents divided into chitin, proteins, tanned pigments, and water. Adapted and reprinted from ref.[46]

The researchers also investigated the formation mechanism of this gradient. While the protein composition of individual sections varied slightly, the most important factor that correlated with stiffness was water content (Figure 1.15c). Each section was gravimetrically analyzed to understand the weight fraction of chitin, proteins, pigment, and water. Interestingly, water content shows an inverse relationship with stiffness, i.e. softer segments contain more water. Gratifyingly, upon drying of these samples, they exhibit similar Young's modulus. Lending more support that the stiffness gradient of the squid beak comes from a softening mechanism via hydration.

The polychaete worm is another animal that relies upon a mechanical gradient for survival. The polychaete worm uses the rigid tip of its jaw to inject venom into its prey. Here, the tip is twice as stiff as the base and the gradient is formed through fine control of two different variables: metal and histidine content (Figure 1.16).[47] X-ray absorbance was used to analyze zinc content of the polychaete jaw (Figure 1.16a). The darker tip shows that more zinc is localized in the tip compared to the rest of the specimen. Histidine is a common amino acid that binds to metal atoms in proteins. Analysis of the amino acid content of different jaw sections shows that there is a clear trend between histidine content and mechanical strength (Figure 1.16b). The authors hypothesize that gradient formation is based on this strong histidine-zinc interaction, but that the majority of the mechanical strength comes from the varying zinc concentration. These lessons from nature are prime examples for the researchers to borrow the gradient motif to create synthetic materials with exceptional mechanical properties.

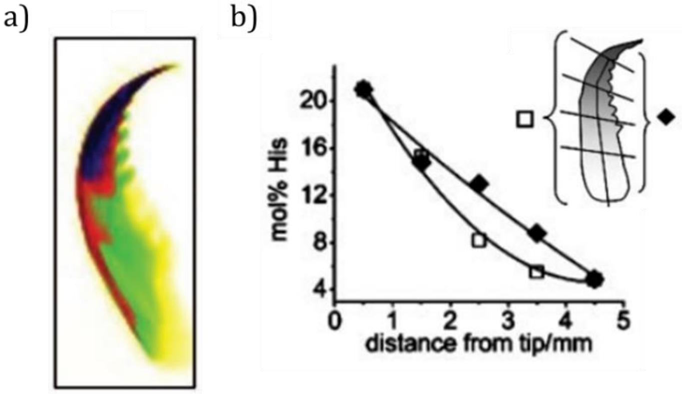

Figure 1.16 Analysis of polychaete worm jaw. (a) Zinc distribution in worm jaw via x-ray absorption. Darker region indicates higher zinc content. (b) Amino acid analysis of worm jaw shows higher abundance of histidine closer to the tip of the jaw. Adapted and reprinted from ref.[47]

1.4.2 Synthetic mechanical gradients

In a quest to mimic nature's ability for advanced function, researchers have started work to emulate the gradients seen in nature. Synthetic mechanical gradients are typically made via two main pathways. First, layer-by-layer designs which are formed through multiple depositions of material on top of a surface.[48–50] Alternatively, lateral gradients can be made in a variety of ways and are a more broadly defined class.[50–53] Layered gradients have the inherent issue that they are not continuous and stress often builds at the interfaces between layers. Additionally, layers can have adhesion issues that limit their overall robustness. Generally, lateral gradients exhibit more smooth transitions in mechanical properties, but often require complex synthetic efforts to be achieved. A general issue with the fabrication of mechanical gradients is that they often suffer from small spans of stiffness.

Stuart Rowan and coworkers took direct inspiration from the squid beak when they designed and fabricated a mechanical gradient based on the variable hydration of a synthetic matrix.[51] Specifically, a poly(vinyl acetate) (PVAc) matrix was used and combined with cellulose nanocrystal filler and thiol-ene crosslinks (Figure 1.17a). During fabrication, a photomask was used to vary the exposure of different parts of the sample to UV irradiation. UV light was used to trigger a thiol-ene crosslinking reaction. After completion of the cure step, the PVAc matrix was soaked in water, leading to less crosslinked sections of the material possessing higher water content. This fabrication technique resulted in a material that contained a fairly continuous mechanical gradient with a 5-fold mechanical contrast between the stiffest and weakest sections (Figure 1.17b). This example highlights the difficulty that researchers have had achieving the 100-fold mechanical contrast of the squid beak.

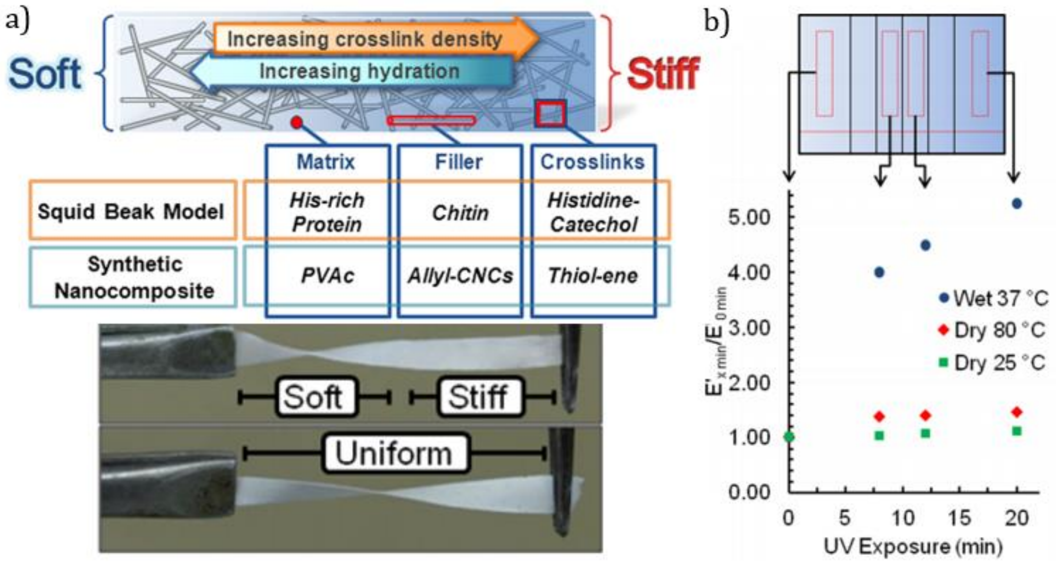

Figure 1.17 Synthetic fabrication of squid beak inspired material. (a) Mechanical gradient component comparison between squid beak and synthetic nanocomposite (above) and twisted gradient samples (below). (b) Tensile testing of specific gradient sections under various conditions. Adapted and reprinted from ref.[51]

1.5 Vitrimer Materials

1.5.1 Vitrimer materials in nature

The term vitrimer was defined in 2011 by Leibler and co-workers. It is defined as a material with a permanent organic network that is able to flow above a certain temperature.[54] The key trait of a vitrimer is that above this transition temperature the sample turns to a semi-liquid state without losing network integrity. While this property is not mirrored often in biological materials, the term “vitrimer” comes rooted in inspiration from nature due to their glass-like fluidity.

Glass is a non-crystalline, amorphous solid that is used broadly in day-to-day life.[55] More specifically, the common term ‘glass’ often refers to silicate glass, made of silica (SiO_2). Silica is the main constituent of sand and silicate glass can naturally be formed when lighting strikes a beach. Silicate glass can also form naturally during a volcanic eruption if conditions are suitable. Due to the availability of silica and simple processing conditions, the history of silicate glass is thought to be traced back to 3500 BC. This natural product has proved useful to humanity due to its ease of molding. It is the goal of researchers to bring the same characteristic of material processing to thermoset materials.

1.5.2 Synthetic vitrimer materials

Thermoset materials are used for their mechanical durability, creep resistance at service temperature, and robust solvent resistance. A major drawback with thermosets is that they cannot be reprocessed. This limits their lifetime and increases their impacts on the environment. Vitrimers promise to take the place of traditional thermoset materials by maintaining the positive properties of thermosets, while becoming thermally reprocessable.

To qualify as a vitrimer, a material must possess two main traits.[56] First, the material must possess a latent dynamic chemistry that is invisible at service temperature (i.e. no creep), but leads to malleability at elevated temperature. Second, the material must exhibit solvent resistance at all temperatures. A vitrimer typically undergoes two important thermal transitions. First, the glass transition temperature(T_g), when a material transitions from a glassy to rubbery state. Second, a topology freezing transition temperature (T_v), when the crosslinks transition from locked to mobile. Typically, $T_g < T_v$, but this is not always the case.[57] Above T_v, the material's flow is governed by the exchange kinetics of the dynamic covalent crosslink. As a result, the Arrhenius law can be used to fit the flow behavior and, important for processing conditions, these exchange reactions stop the material from turning to a typical fluid. For a material to exhibit solvent resistance at all temperatures, the dynamic chemistry must undergo an associative exchange mechanism. This associative mechanism ensures that the overall crosslink density of the material is maintained throughout the process and dissolution cannot occur.

The first material described as a vitrimer was designed and fabricated in 2011.[54] Here, an epoxy network crosslinked via ester motif was combined with a zinc transesterification catalyst (Figure 1.18a). At service temperatures, the catalyst was inactive, but > 100 °C network relaxation was observed (Figure 1.18b). This network relaxation fit the Arrhenius equation because the relaxation rate was governed by the transesterification reaction. As a result, the material could be reprocessed from a powder at 240 °C for three minutes (Figure 1.18c). This robust material began a research resurgence into dynamically crosslinked materials.[56] A major drawback with this system is the limitation to ester crosslinked materials. A step forward from this work would be to bring the vitrimer concept to a variety of commercially-relevant polymer backbones.

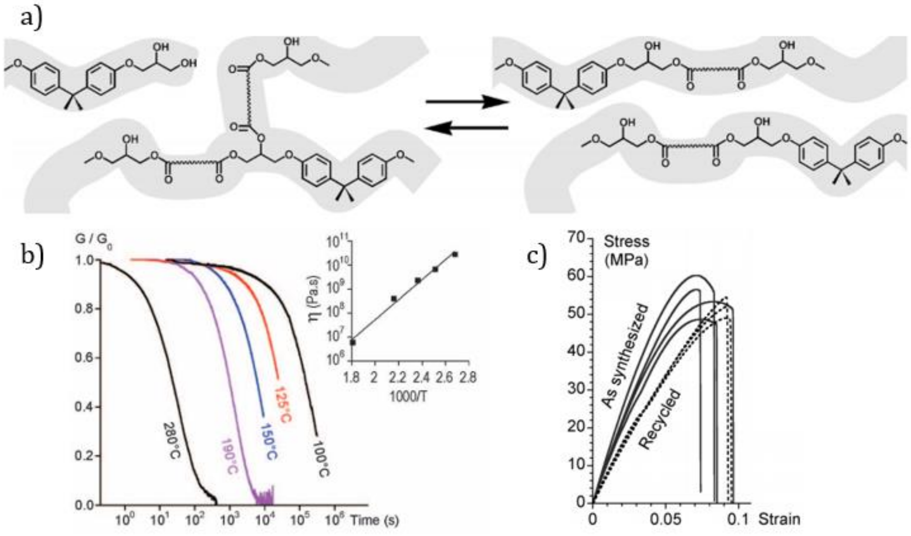

Figure 1.18 Vitrimer design based on transesterification of epoxy network. (a) Exchange reaction via transesterification. (b) Stress relaxation behavior at various temperatures, showing higher temperature leads to faster relaxation. (c) Tensile testing to compare as synthesized and reprocessed samples. Adapted and reprinted from ref.[54]

Professor Zhibin Guan's group at UC Irvine has designed and synthesized multiple materials that fit the definition of a vitrimer. These systems were based on dynamic motifs that included olefin metathesis,[34] silyl ether exchange,[57] and boronic ester exchange.[58] The boron-based vitrimer was first described in 2015.[58] Here, researchers synthesized a diol containing polymer via ring-opening metathesis polymerization of a cyclooctene derivative (Figure 1.19). Next, a diboronic ester cross-linker was added to the material. The dynamic properties of this crosslinker were attributed to the neighboring tertiary amines that were hypothesized to stabilize the transition state of diol exchange. This work was highlighted the usefulness of boron crosslinkers and their tunability based on functional groups built into the crosslinker. Additionally, this report demonstrated the ability to transfer small molecule kinetics to dynamic properties of bulk solids.

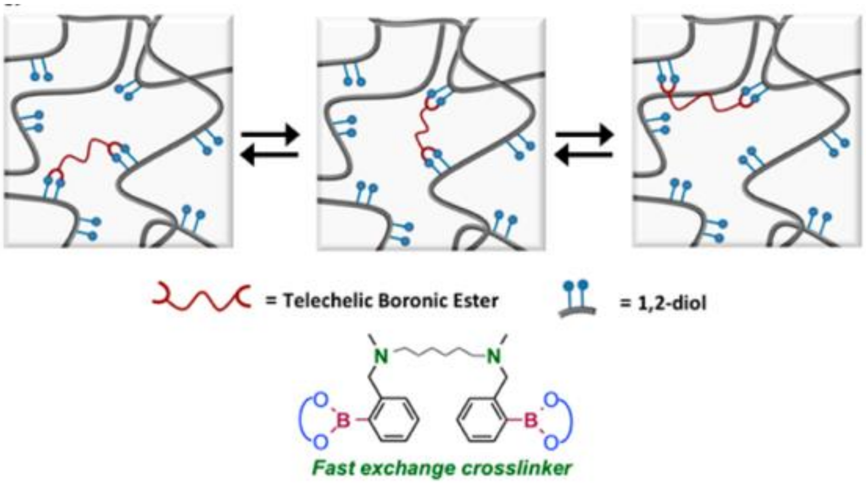

Figure 1.19 First vitrimer design based on diboronic ester crosslinkers. Neighboring tertiary amines promote crosslinker exchange to give the material vitrimeric properties.[58]

As a follow-up to work completed with boron crosslinkers in 2015, the boron vitrimer concept was brought to commodity thermoplastics in 2017.[59] To incorporate dynamic crosslinks into commodity materials, researchers took advantage of a mild dioxaborolane metathesis reaction. Surprisingly, this metathesis reaction was observed to react at the mild temperature of 60 °C. The low T_v of this system led to the rare case where $T_g > T_v$. In this case, minimal creep is observed at service temperatures, when service temperature < T_g, because diminished polymer mobility keeps the material creep resistant. In this system, dioxaborolanes were incorporated into polystyrene (PS), poly(methyl methacrylate) (PMMA), and polyethylene (HDPE) backbones (Figure 1.20a). Next, the material was crosslinked through incorporation of bis-dioxaborolane. Overall, vitrimer formation in the HDPE matrix had no effect on tensile strength and decreased elongation-at-break by 33%. The material was able to be reprocessed three times with no effect on tensile strength or elongation-at-break. An added property from the incorporation of boron-containing crosslinks was the ability to weld together dissimilar materials. Interestingly, the researchers were able to 'glue together' PMMA and HDPE at 190 °C due to the boron-mediated crosslinking reaction across the material interface (Figure 1.20b). A double lap joint tensile test of the material compared the robustness of adhesion between materials without crosslinker (black), materials in contact for 10 min (blue), and materials in contact for 20 min (red). Incredibly, after contact for 20 min, failure occurred in the bulk of the PMMA sample instead of adhesive failure. While this material was able to bring vitrimer technology to commodity thermoplastics, a major drawback with this system is the reliance on thermally and oxidatively unstable boron crosslinks. The reliance on the dioxaborolane motif will limit its potential application.

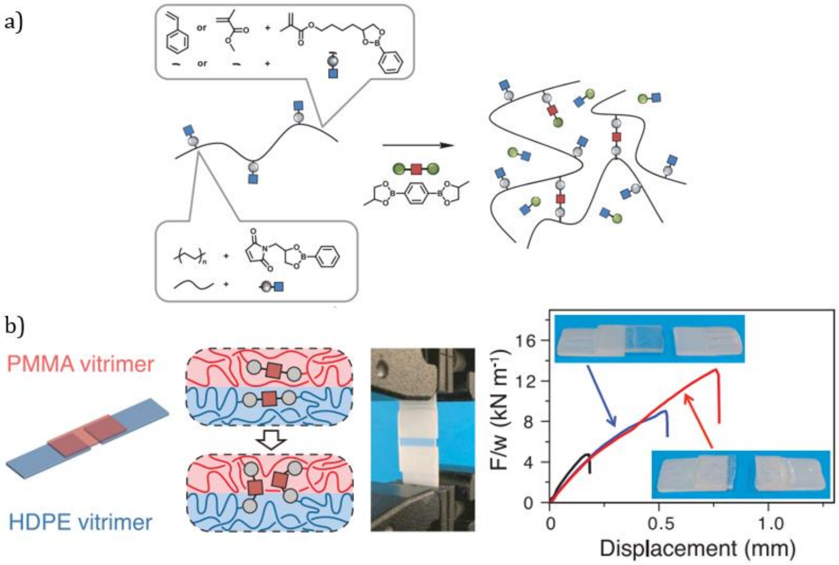

Figure 1.20 Vitrimer design based on dioxaborolane metathesis reaction. (a) Incorporation of dioxaborolane monomers into commercial (PS, PMMA, HDPE) polymers and subsequent crosslinking by di-functional dioxaborolane. (b) Improved adhesion of PMMA and HDPE via boron crosslinks. Double lap joint test (right) of adhesion (190 °C, 11 kPa) without crosslink (black), contact time 10 min (blue), contact time 20 min (red). Adapted and reprinted from ref.[59]

1.6 References

(1) American Chemical Society National Historic Chemical Landmarks. Bakelite: The World's First Synthetic Plastic http://www.acs.org/content/acs/en/education/whatischemistry/landmarks/bakelite.html (accessed Jul 20, 2018).

(2) Nicholson, J. L.; Leighton, G. R. *Harper's Magazine*. 1942.

(3) Breslow, R. *Chem. Soc. Rev.* **1972**, *1* (4), 553.

(4) Pasparakis, G.; Krasnogor, N.; Cronin, L.; Davis, B. G.; Alexander, C. *Chem. Soc. Rev.* **2010**, *39* (1), 286–300.

(5) Zheng, Y.; Gao, X.; Jiang, L. *Soft Matter* **2007**, *3* (2), 178–182.

(6) Zhao, Y.; Sakai, F.; Su, L.; Liu, Y.; Wei, K.; Chen, G.; Jiang, M. *Adv. Mater.* **2013**, *25* (37), 5215–5256.

(7) Blaiszik, B. J.; Kramer, S. L. B.; Olugebefola, S. C.; Moore, J. S.; Sottos, N. R.; White, S. R. *Annu. Rev. Mater. Res.* **2010**, *40* (1), 179–211.

(8) Diegelmann, R. F.; Evans, M. C. *Front. Biosci.* **2004**, *9*, 283–289.

(9) Han, R.; Campbell, K. P. *Curr. Opin. Cell Biol.* **2007**, *19* (4), 409–416.

(10) París, R.; Lamattina, L.; Casalongué, C. A. *Plant Physiol. Biochem.* **2007**, *45* (1), 80–86.

(11) Smith, B. L.; Schäffer, T. E.; Viani, M.; Thompson, J. B.; Frederick, N. A.; Kindt, J.; Belcher, A.; Stucky, G. D.; Morse, D. E.; Hansma, P. K. *Nature* **1999**, *399* (6738), 761–763.

(12) Thompson, J. B.; Kindt, J. H.; Drake, B.; Hansma, H. G.; Morse, D. E.; Hansma, P. K. *Nature* **2001**, *414* (6865), 773–776.

(13) Oroudjev, E.; Soares, J.; Arcidiacono, S.; Thompson, J. B.; Fossey, S. A.; Hansma, H. G.

Proc. Natl. Acad. Sci. **2002**, *99* (Supplement 2), 6460–6465.

(14) Granzier, H. L.; Labeit, S. *Circ. Res.* **2004**, *94* (3), 284–295.

(15) Rief, M. *Science.* **1997**, *276* (5315), 1109–1112.

(16) Li, H.; Oberhauser, A. F.; Fowler, S. B.; Clarke, J.; Fernandez, J. M. *Proc. Natl. Acad. Sci.* **2000**, *97* (12), 6527–6531.

(17) Lu, H.; Schulten, K. *Proteins* **1999**, *35* (4), 453–463.

(18) Lu, H.; Schulten, K. *Biophys. J.* **2000**, *79* (1), 51–65.

(19) Fantner, G. E.; Hassenkam, T.; Kindt, J. H.; Weaver, J. C.; Birkedal, H.; Pechenik, L.; Cutroni, J. A.; Cidade, G. A. G.; Stucky, G. D.; Morse, D. E.; Hansma, P. K. *Nat. Mater.* **2005**, *4* (8), 612–616.

(20) Burr, D. B. *Bone* **2002**, *31* (1), 8–11.

(21) Hager, M. D.; Greil, P.; Leyens, C.; van der Zwaag, S.; Schubert, U. S. *Adv. Mater.* **2010**, *22* (47), 5424–5430.

(22) Chen, X.; Dam, M. A.; Ono, K.; Mal, A.; Shen, H.; Nutt, S. R.; Sheran, K.; Wudl, F. *Science* **2002**, *295* (5560), 1698–1702.

(23) Chen, Y.; Kushner, A. M.; Williams, G. A.; Guan, Z. *Nat. Chem.* **2012**, *4* (6), 467–472.

(24) Mozhdehi, D.; Ayala, S.; Cromwell, O. R.; Guan, Z. *J. Am. Chem. Soc.* **2014**, *136* (46), 16128–16131.

(25) White, S. R.; Sottos, N. R.; Geubelle, P. H.; Moore, J. S.; Kessler, M. R.; Sriram, S. R.; Brown, E. N.; Viswanathan, S. *Nature* **2001**, *409* (6822), 794–797.

(26) Dry, C. *Compos. Struct.* **1996**, *35* (3), 263–269.

(27) Pang, J. W. C.; Bond, I. P. *Compos. Sci. Technol.* **2005**, *65* (11–12), 1791–1799.

(28) Bleay, S. .; Loader, C. .; Hawyes, V. .; Humberstone, L.; Curtis, P. . *Compos. Part A Appl.*

Sci. Manuf. **2001**, *32* (12), 1767–1776.

(29) White, S. R.; Moore, J. S.; Sottos, N. R.; Krull, B. P.; Santa Cruz, W. A.; Gergely, R. C. R. *Science* **2014**, *344* (6184), 620–623.

(30) Cordier, P.; Tournilhac, F.; Soulié-Ziakovic, C.; Leibler, L. *Nature* **2008**, *451* (7181), 977–980.

(31) Burnworth, M.; Tang, L.; Kumpfer, J. R.; Duncan, A. J.; Beyer, F. L.; Fiore, G. L.; Rowan, S. J.; Weder, C. *Nature* **2011**, *472* (7343), 334–337.

(32) Mozhdehi, D.; Ayala, S.; Cromwell, O. R.; Guan, Z. *J. Am. Chem. Soc.* **2014**, *136*, 16128–16131.

(33) Burnworth, M.; Tang, L.; Kumpfer, J. R.; Duncan, A. J.; Beyer, F. L.; Fiore, G. L.; Rowan, S. J.; Weder, C. *Nature* **2011**, *472* (7343), 334–337.

(34) Lu, Y.-X.; Guan, Z. *J. Am. Chem. Soc.* **2012**, *134* (34), 14226–14231.

(35) Wool, R. P. *Soft Matter* **2008**, *4* (3), 400–418.

(36) Murphy, E. B.; Wudl, F. *Prog. Polym. Sci.* **2010**, *35* (1–2), 223–251.

(37) Buehler, M. J.; Yung, Y. C. *HFSP J.* **2010**, *4* (1), 26–40.

(38) Fratzl, P.; Weinkamer, R. *Prog. Mater. Sci.* **2007**, *52* (8), 1263–1334.

(39) DeGrado, W.; Wasserman, Z.; Lear, J. *Science.* **1989**, *243* (4891), 622–628.

(40) Baker, D. *Science.* **2001**, *294* (5540), 93–96.

(41) Keten, S.; Buehler, M. J. *Nano Lett.* **2008**, *8* (2), 743–748.

(42) Harrington, M. J.; Waite, J. H. *Adv. Mater.* **2009**, *21* (4), 440–444.

(43) Wegner, S. V.; Schenk, F. C.; Witzel, S.; Bialas, F.; Spatz, J. P. *Macromolecules* **2016**, *49* (11), 4229–4235.

(44) Loveless, D. M.; Jeon, S. L.; Craig, S. L. *Macromolecules* **2005**, *38* (24), 10171–10177.

(45) Suresh, S. *Science.* **2001**, *292* (5526), 2447–2451.

(46) Miserez, A.; Schneberk, T.; Sun, C.; Zok, F. W.; Waite, J. H. *Science.* **2008**, *319* (5871), 1816–1819.

(47) Lichtenegger, H. C.; Schoberl, T.; Ruokolainen, J. T.; Cross, J. O.; Heald, S. M.; Birkedal, H.; Waite, J. H.; Stucky, G. D. *Proc. Natl. Acad. Sci.* **2003**, *100* (16), 9144–9149.

(48) Libanori, R.; Erb, R. M.; Reiser, A.; Le Ferrand, H.; Süess, M. J.; Spolenak, R.; Studart, A. R. *Nat. Commun.* **2012**, *3*, 1265.

(49) Ionov, L. *Mater. Today* **2014**, *17* (10), 494–503.

(50) Claussen, K. U.; Giesa, R.; Schmidt, H.-W. *Polymer.* **2014**, *55* (1), 29–38.

(51) Fox, J. D.; Capadona, J. R.; Marasco, P. D.; Rowan, S. J. *J. Am. Chem. Soc.* **2013**, *135* (13), 5167–5174.

(52) Kim, J.; Mok, M. M.; Sandoval, R. W.; Woo, D. J.; Torkelson, J. M. *Macromolecules* **2006**, *39* (18), 6152–6160.

(53) Zhang, X.; Hassanzadeh, P.; Miyake, T.; Jin, J.; Rolandi, M. *J. Mater. Chem. B* **2016**, *4* (13), 2273–2279.

(54) Montarnal, D.; Capelot, M.; Tournilhac, F.; Leibler, L. *Science* **2011**, *334* (6058), 965–968.

(55) Glass https://en.wikipedia.org/wiki/Glass (accessed Jul 20, 2018).

(56) Denissen, W.; Winne, J. M.; Du Prez, F. E. *Chem. Sci.* **2016**, *7* (1), 30–38.

(57) Nishimura, Y.; Chung, J.; Muradyan, H.; Guan, Z. *J. Am. Chem. Soc.* **2017**, *139* (42), 14881–14884.

(58) Cromwell, O. R.; Chung, J.; Guan, Z. *J. Am. Chem. Soc.* **2015**, *137* (20), 6492–6495.

(59) Röttger, M.; Domenech, T.; van der Weegen, R.; Breuillac, A.; Nicolaÿ, R.; Leibler, L.

Science. **2017**, *356* (6333), 62–65.

Chapter 2: Enhancing Mechanical Performance of a Covalent Self-Healing Material by Sacrificial Noncovalent Bonds

2.1 Introduction

2.1.1 The current state of self-healing materials

In contrast to biological systems that can spontaneously self-repair, most synthetic materials cannot self-heal following mechanical damage. Mimicking nature's ability to heal would result in new materials with improved durability and safety. A variety of self-healing polymers have been developed. Healing agents[1] as well as reversible covalent[2–11] and noncovalent bonds,[12–18] with stimuli such as heat[19] and light,[14,20] have been used to promote healing. A major challenge in the expanding field of self-healing polymers is to combine robust mechanical properties and high healing efficiency under mild conditions.[21,22] Currently, most spontaneous and intrinsically self-healing materials are limited to relatively weak polymeric systems due to the necessity of high chain dynamics required for healing. The weak mechanical properties of efficient self-healing materials will limit their potential applications.

An important strategy employed in biological materials to enhance mechanical properties is incorporation of sacrificial noncovalent bonds.[23] Noncovalent sacrificial bonds in polymeric materials can efficiently dissipate large amounts of energy through reversible bond rupture, affording a unique combination of high toughness and the ability to reversibly recover after large strain.[24,25] Reversible sacrificial bonds commonly used as transient cross-linkers in synthetic materials include ionic,[26] metal–ligand,[27] and hydrogen-bonding interactions.[28–31] Whereas a few covalent self-healing polymers contain sacrificial bonds,[11] to the best of our knowledge, such sacrificial bond strategy has not been carefully studied nor purposely used to enhance the mechanical properties of self-healing polymers.

2.1.2 Our design for a sacrificial bond containing self-healing material

Herein, we demonstrate that incorporation of a simple, sacrificial hydrogen-bonding amide functionality dramatically enhances the mechanical performance of a covalent self-healing polymeric network (Figure 2.1).

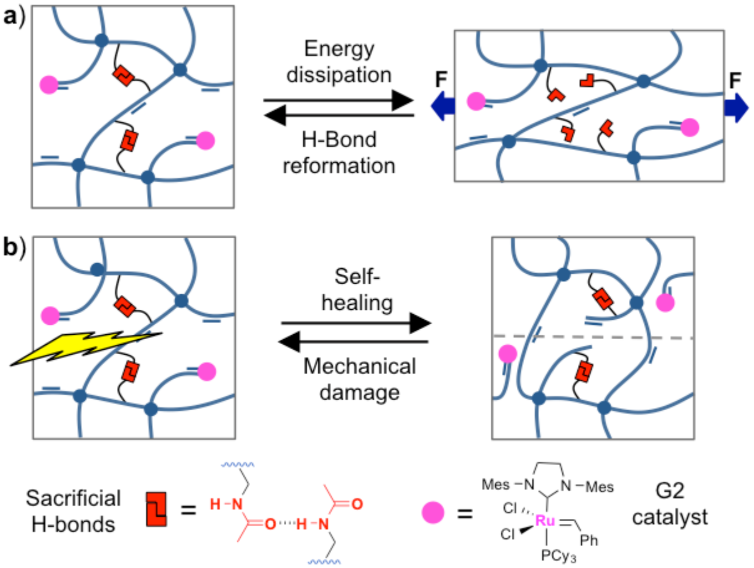

Figure 2.1 Design concept. (a) Reversible, energy dissipative rupture of sacrificial hydrogen bonds in a (b) G2-mediated self-healing olefin-containing network.

The covalent self-healing system we used to illustrate this concept is based on the dynamic olefin metathesis reaction that our laboratory has previously demonstrated for efficient covalent self-healing.[4] Specifically, we introduced secondary amide side chains into a cyclooctene (CO)-based, olefin-containing polymer backbone. After cross-linking the polymer and incorporating the Grubbs' second-generation ruthenium catalyst (G2), a self-healing network was created with both transient and covalent cross-links. Upon stress, the hydrogen bonds are broken to dissipate energy, which results in an increased overall toughness of the material. Due to the reversibility of hydrogen bonds, unloading of stress allows hydrogen bonds to re-form, thereby increasing toughness over multiple loading cycles (Figure 2.1a). Following mechanical damage, G2-mediated olefin metathesis at the fracture interface results in self-healing (Figure 2.1b). A secondary amide was used for its dynamic hydrogen-bonding capability,[12] compatibility with G2,[32] and synthetic simplicity.

2.2 Results and Discussion

2.2.1 Synthesis and characterization

The synthesis of secondary amide-containing CO networks (ACON) is summarized in Scheme 2.1. First, hydroxylated CO (**2**) was synthesized from cyclooctadiene (COD) via stoichiometrically controlled epoxidation[33] followed by epoxide opening with DIBAL-H (Scheme 2.1a).[34] From precursor **2**, we prepared the secondary amide-functionalized CO derivative (**3**) via carbodiimide coupling with N-acetylglycine.[35] An analogous control monomer was synthesized with the hydrogen-bonding capability blocked through *N*-methylation of the amide group (**4**).

ACON was synthesized from monomer **3** via ring-opening metathesis polymerization with G2, a robust and functional group-tolerant catalyst.[32,36,37] We chose to copolymerize **3** with CO to control the amide mole fraction in ACON (Scheme 2.1b). Following our reported protocol,[38] the ACON polymer was cross-linked by radical reaction and G2 was incorporated by swelling ([olefin]/[G2] = 2000) to form the ACON network. For comparison, we synthesized a control CO network with the amide hydrogen bond blocked (BACON) through copolymerization of **4** with CO. The properties of both polymer networks are summarized in Table 2.1. The molecular weights for the hydrogen bonding and control polymers are very close. The small differences in molecular weight should not significantly affect the mechanical properties of the networks because the polymers are covalently cross-linked.[39] ACON was synthesized with incorporation of **3** at 20 mol % because this composition affords a combination of enhanced mechanical properties and efficient healing. Non-cross-linked prepolymers of ACON and BACON possess identical melting transitions (Tm) of ~20 °C. Furthermore, the similar swelling ratios of ACON and BACON indicate that cross-linking densities are nearly identical.

Scheme 2.1 Synthesis of cyclooctene derivatives and olefin-containing polymers[a]

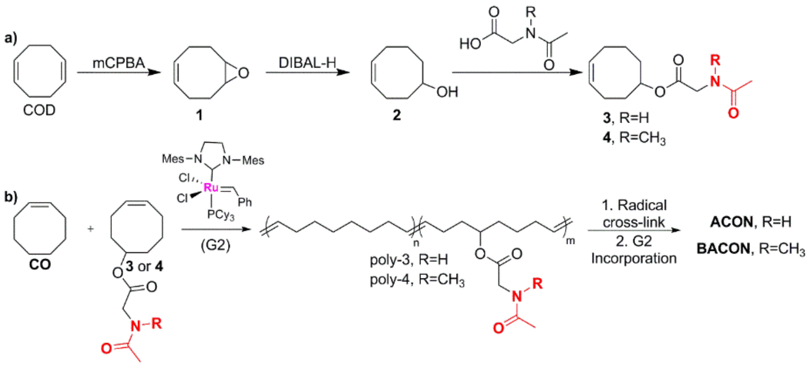

[a](a) Synthesis of hydrogen-bonding cyclooctene derivative **3** and the blocked control derivative **4**. (b) Synthesis of the amide-containing CO network (ACON) and hydrogen-bond-blocked control network (BACON).

Table 2.1 Molecular and physical characterization of ACON and BACON

sample	mol % **3** or **4**[a]	M_n[b] (kDa)	M_w/M_n[b]	T_m[c] (°C)	swelling ratio[d]
ACON	20 (**3**)	155	1.69	21.89	4.39 ± 0.07
BACON	20 (**4**)	157	2.10	19.70	4.85 ± 0.08

[a]Estimated from ^{1}H NMR. [b]Estimated from size exclusion chromatography (SEC) using polystyrene standards in THF. [c]Determined via differential scanning calorimetry (DSC) of polymers before cross-linking. [d]Calculated using ASTM protocol D2765 - 11.[40]

2.2.2 Mechanical properties via uniaxial tensile testing

The mechanical properties of ACON and BACON were characterized via static uniaxial tensile testing (Figure 2.2 and Table 2.2). We observe a dramatic increase in maximal strain-at-break and toughness after the incorporation of sacrificial hydrogen bonds (Figure 2.2a). ACON was over 7-fold tougher than the analogous control polymer, illustrating the energy dissipative capability of sacrificial hydrogen bonds. ACON achieved a significantly higher strain-at-break near 950%, while the control network, BACON, extended to only 150%. Interestingly, the sacrificial bonds do not contribute to the initial stiffness, as the Young's moduli of both networks are near 2.50 MPa. This is in agreement with a previous study on "mechanically invisible" cross-linked gels[27] in which Craig et al. explored transient metal–ligand cross-links that did not contribute to the initial stiffness of the sample but sufficiently dissipated energy to increase the strain-at-break of the material. Presumably, the lifetime for monodendate hydrogen bonds of amides in our system is very short, making them "mechanically invisible" at the time scale of the tensile experiment. Therefore, the transient hydrogen bonds do not contribute to the Young's modulus but increase the strain-at-break and toughness through energy dissipation.

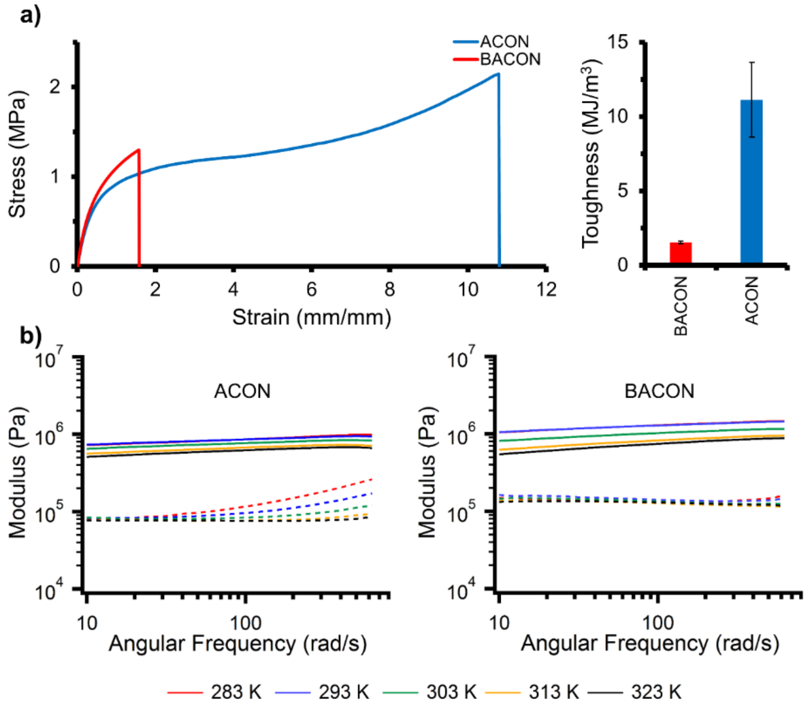

Figure 2.2 Mechanical analysis. (a) Representative stress−strain curves for ACON and BACON (strain rate: 100 mm/min, 25 °C). Bar graphs summarize the toughness of each sample (three measurements). (b) Isotherm of the storage (solid) and loss (dash) moduli at various frequencies and temperatures for the non-cross-linked ACON (left) and BACON (right) prepolymer samples.

Table 2.2 Summary of mechanical and self-healing properties[a]

sample	*E*[b] (MPa)	tensile strength (MPa)	ε[c] (%)	toughness[d] (MJ/m^3)
ACON	2.34 ± 0.22	1.66 ± 0.35	938 ± 101	11.13 ± 2.51
BACON	2.51 ± 0.10	1.31 ± 0.01	167 ± 9	1.513 ± 0.09
ACON 1 h[e]	2.15 ± 0.12	1.14 ± 0.15	408 ± 132	3.67 ± 1.57
ACON 3 h[e]	2.32 ± 0.28	1.65 ± 0.26	835 ± 66	9.75 ± 2.06

[a]All tensile tests were conducted at strain rate of 100 mm/min, at 25 °C. [b]Young's modulus. [c]Maximum strain-at-break. [d]Calculated by integration of the area under stress-strain curves. [f]Self-healed samples after the designated time.

2.2.3 Investigation of dynamic sacrificial bonds via melt rheology

To further understand the effect of hydrogen bonds on the dynamic mechanical properties of our system, we surveyed the rheological properties of both non-cross-linked ACON and BACON prepolymers by measuring the storage and loss moduli at various frequencies and temperatures under constant low strain (0.1%). While the storage modulus for both samples remained relatively constant across the frequency range, the loss modulus exhibited a clear frequency-dependent behavior for ACON samples at lower temperatures (Figure 2.2b, left). Given the high degree of polymerization for both polymers and the relatively low number of hydrogen bonds along the backbone, the storage modulus should be mainly determined by the modulus of the entangled polymer chains.[41,42] However, the sacrificial hydrogen bonds have a more pronounced effect on the frequency dependence of the loss modulus. At low frequencies, hydrogen-bonding kinetics are too fast for efficient energy dissipation. As the frequency is increased to approach the hydrogen-bonding kinetics, dissociation of transient hydrogen bonds and subsequent chain relaxation provides energy dissipation under shear stress, thus contributing to the observed increase in the loss modulus of ACON (Figure 2.2b, left). A temperature increase perturbs the equilibrium and kinetics of the hydrogen bond association, therefore, reducing their effect on energy dissipation and loss modulus. Consistent with previous reports of functionalized polybutadiene with hydrogen-bonding units,[28,42] the upward transition of loss modulus is shifted to lower frequency by incorporation of hydrogen-bonding units.

2.2.4 Analysis of sacrificial bond recovery via cyclic tensile testing

In practical applications, materials often undergo repeated stress cycles. Therefore, the reversibility and recovery of the sacrificial hydrogen bonds in ACON were probed through cyclic tensile testing (Figure 2.3). For this study, G2 was not incorporated into the samples to avoid the complication of plastic deformation due to olefin metathesis. ACON was pulled to an extensibility (300%) that would be catastrophic for the control network which breaks at 167% strain. The ACON sample was loaded, unloaded, and immediately reloaded 10 times. Significant hysteresis was observed in the first loading−unloading cycle, indicating a large amount of energy dissipation through rupture of multiple hydrogen bonds. However, 80% of the energy dissipation observed in cycle 1 was lost in cycle 2. A similar phenomenon has been observed in other systems containing both hydrogen bond and covalent cross-links[29] and is attributed to the buildup of elastic deformation, which cannot relax to equilibrium on the time scale of individual cycles. Over subsequent cycles (cycles 3−10), the amount of energy dissipation continued to slightly decrease, which we attribute to additional elastic deformation. After 10 cycles, ACON was allowed to relax under ambient conditions for 30 min to recover its original length. Cycle 11 shows that ~90% of the original energy dissipation observed in cycle 1 was recovered in this short time. We propose that the excellent recovery of energy dissipative properties is due to the survival of covalent cross-links, which prevent permanent deformation and assist in the re-formation of sacrificial hydrogen bonds.

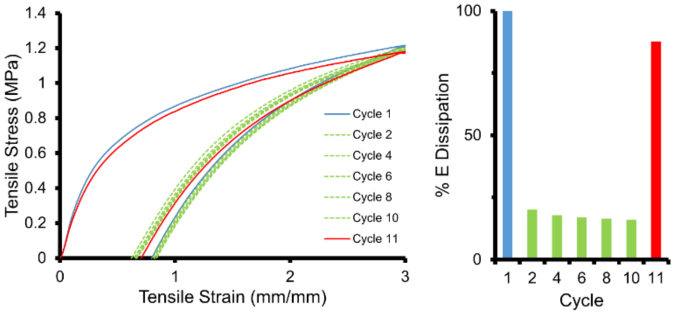

Figure 2.3 Recovery and cyclic loading of ACON with no G2 incorporation. ACON specimens were loaded (300%), unloaded, and immediately reloaded 10 times (strain rate: 100 mm/min, 25 °C). Cycles 1, 2, 4, 6, 8, 10, and 11 are plotted for clarity. Cycle 11 took place after no stress for 30 min at room temperature. Bar graphs summarize the percent energy dissipation for each sample.

2.2.5 Self-healing studies

Finally, the self-healing behavior of the ACON sample was investigated by following reported protocols.[43] Previous studies have shown that G2 can tolerate a wide range of polar functional groups including secondary amide groups.[32,36,37] We envisioned that the incorporation of sacrificial hydrogen-bonding secondary amides should not negatively impact olefin cross-metathesis in our bulk samples for self-healing. To test this, ACON samples were damaged (cut through 70−90% of width) and the cut interfaces were brought together with slight pressure for 1 min. The sample was then left to heal at 50 °C in air with no applied pressure for the remainder of the experiment. Moderate heat is required to facilitate ACON healing because the sample is semicrystalline with a broad melting transition in the range of −5 to 40 °C (see experimental section). The crystallinity reduces chain dynamics and impedes the self-healing process. Heating the sample at 50 °C melts the crystalline phase and enhances the healing ability. After the desired healing time, the extent of healing was quantified via percent recovery of pristine sample toughness (Figure 2.4a). Each polymer was treated under identical conditions in triplicate to characterize their healing.

Healing experiments confirm that the new system containing sacrificial hydrogen bonds shows excellent healing properties. For all healing times, the stress–strain curves overlap closely with the original samples (Figure 2.4a). ACON achieved 90% toughness recovery after healing for just 3 h in air at 50 °C. The study suggests that the healing is time-dependent, as 1 h healing achieved near 30% toughness recovery. Additionally, we observe fast and complete recovery of the Young's modulus after just 1 h of healing (Figure 2.4a, red curve, and Table 2.2). The healing is through olefin cross-metathesis at the cut interface. For a control study, ACON samples without incorporation of the G2 catalyst show only minimal healing when following an identical protocol (Figure 2.4b). The efficient healing of ACON samples indicates that G2 turnover frequency is not significantly affected by secondary amide functionality at the tested incorporation ratios of **3**.

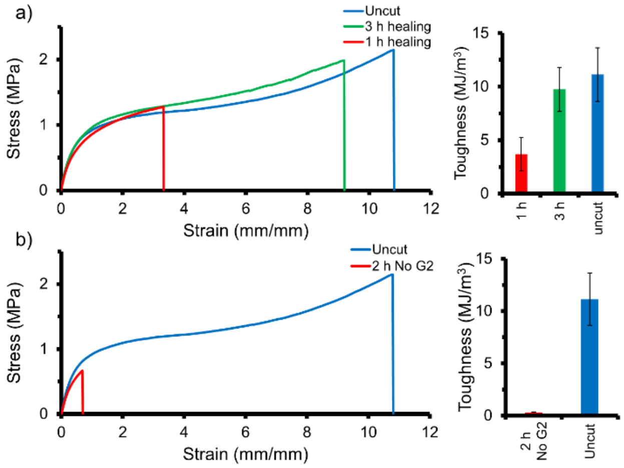

Figure 2.4 Self-healing analysis. (a) Self-healing experiments for ACON samples at 50 °C in air. (b) Control self-healing experiment for ACON with no G2 incorporation at 50 °C in air. Bar graphs summarize toughness recovery at various time points.

2.3 Conclusion

In summary, we have demonstrated that sacrificial hydrogen bonds introduced through incorporation of simple secondary amide side chains dramatically improve the mechanical performance of a dynamic covalent self-healing material. By incorporating 20 mol % of our sacrificial hydrogen-bonding monomer (**3**) into an olefin-containing network, the strain-atbreak was increased from 150% for the control network to 950%, and the toughness of the network was enhanced by more than 7-fold. Rheological and cyclic tensile experiments were used to further probe the energy dissipation and reversible recovery of the sacrificial hydrogen bonds in our bulk system. Mediated by the G2 catalyst, the olefin-containing network displays efficient healing under relatively mild conditions. The attained robust mechanical properties combined with the efficient self-healing capability are highly desirable for many practical applications. We anticipate that this straightforward sacrificial bonding strategy can be employed to improve mechanical properties of many other self-healing systems. These studies are currently underway, and the results will be disseminated in time.

2.4 References

(1) White, S. R.; Sottos, N. R.; Geubelle, P. H.; Moore, J. S.; Kessler, M. R.; Sriram, S. R.; Brown, E. N.; Viswanathan, S. *Nature* **2001**, *409* (6822), 794–797.

(2) Montarnal, D.; Capelot, M.; Tournilhac, F.; Leibler, L. *Science* **2011**, *334* (6058), 965–968.

(3) Capelot, M.; Montarnal, D.; Tournilhac, F.; Leibler, L. *J. Am. Chem. Soc.* **2012**, *134* (18), 7664–7667.

(4) Lu, Y.-X.; Guan, Z. *J. Am. Chem. Soc.* **2012**, *134* (34), 14226–14231.

(5) Amamoto, Y.; Kamada, J.; Otsuka, H.; Takahara, A.; Matyjaszewski, K. *Angew. Chemie - Int. Ed.* **2011**, *50* (7), 1660–1663.

(6) Imato, K.; Nishihara, M.; Kanehara, T.; Amamoto, Y.; Takahara, A.; Otsuka, H. *Angew. Chemie - Int. Ed.* **2012**, *51* (5), 1138–1142.

(7) Yao, L.; Yuan, Y. C.; Rong, M. Z.; Zhang, M. Q. *Polymer.* **2011**, *52* (14), 3137–3145.

(8) Deng, G.; Tang, C.; Li, F.; Jiang, H.; Chen, Y. *Macromolecules* **2010**, *43* (3), 1191–1194.

(9) Ying, H.; Zhang, Y.; Cheng, J. *Nat. Commun.* **2014**, *5*, 3218.

(10) Zheng, P.; McCarthy, T. J. *J. Am. Chem. Soc.* **2012**, *134* (4), 2024–2027.

(11) Martin, R.; Rekondo, A.; Ruiz de Luzuriaga, A.; Cabañero, G.; Grande, H. J.; Odriozola, I. *J. Mater. Chem. A* **2014**, *2* (16), 5710.

(12) Chen, Y.; Kushner, A. M.; Williams, G. A.; Guan, Z. *Nat. Chem.* **2012**, *4* (6), 467–472.

(13) Cordier, P.; Tournilhac, F.; Soulié-Ziakovic, C.; Leibler, L. *Nature* **2008**, *451* (7181), 977–980.

(14) Burnworth, M.; Tang, L.; Kumpfer, J. R.; Duncan, A. J.; Beyer, F. L.; Fiore, G. L.; Rowan, S. J.; Weder, C. *Nature* **2011**, *472* (7343), 334–337.

(15) Burattini, S.; Greenland, B. W.; Merino, D. H.; Weng, W.; Seppala, J.; Colquhoun, H. M.; Hayes, W.; MacKay, M. E.; Hamley, I. W.; Rowan, S. J. *J. Am. Chem. Soc.* **2010**, *132*, 12051–12058.

(16) Wang, C.; Liu, N.; Allen, R.; Tok, J. B. H.; Wu, Y.; Zhang, F.; Chen, Y.; Bao, Z. *Adv. Mater.* **2013**, *25*, 5785–5790.

(17) Bode, S.; Zedler, L.; Schacher, F. H.; Dietzek, B.; Schmitt, M.; Popp, J.; Hager, M. D.; Schubert, U. S. *Adv. Mater.* **2013**, *25* (11), 1634–1638.

(18) Ahn, B. K.; Lee, D. W.; Israelachvili, J. N.; Waite, J. H. *Nat. Mater.* **2014**, *13* (9), 867–872.

(19) Chen, X.; Dam, M. A.; Ono, K.; Mal, A.; Shen, H.; Nutt, S. R.; Sheran, K.; Wudl, F. *Science* **2002**, *295* (5560), 1698–1702.

(20) Ghosh, B.; Urban, M. W. *Science* **2009**, *323* (5920), 1458–1460.

(21) Wool, R. P. *Soft Matter* **2008**, *4* (3), 400–418.

(22) Murphy, E. B.; Wudl, F. *Prog. Polym. Sci.* **2010**, *35* (1–2), 223–251.

(23) Fantner, G. E.; Hassenkam, T.; Kindt, J. H.; Weaver, J. C.; Birkedal, H.; Pechenik, L.; Cutroni, J. A.; Cidade, G. A. G.; Stucky, G. D.; Morse, D. E.; Hansma, P. K. *Nat. Mater.* **2005**, *4* (8), 612–616.

(24) Zhao, X. *Soft Matter* **2014**, *10*, 672–687.

(25) Haque, M. A.; Kurokawa, T.; Gong, J. P. *Polymer.* **2012**, *53* (9), 1805–1822.

(26) Sun, T. L.; Kurokawa, T.; Kuroda, S.; Ihsan, A. Bin; Akasaki, T.; Sato, K.; Haque, M. A.; Nakajima, T.; Gong, J. P. *Nat. Mater.* **2013**, *12* (10), 932–937.

(27) Kean, Z. S.; Hawk, J. L.; Lin, S.; Zhao, X.; Sijbesma, R. P.; Craig, S. L. *Adv. Mater.* **2014**, *26* (34), 6013–6018.

(28) Müller, M.; Seidel, U.; Stadler, R. *Polymer.* **1995**, *36* (16), 3143–3150.

(29) Zhang, H.; Chen, Y.; Lin, Y.; Fang, X.; Xu, Y.; Ruan, Y.; Weng, W. *Macromolecules* **2014**, *47* (19), 6783–6790.

(30) Yang, J.; Han, C.-R.; Zhang, X.-M.; Xu, F.; Sun, R.-C. *Macromolecules* **2014**, *47* (12), 4077–4086.

(31) Kushner, A. M.; Gabuchian, V.; Johnson, E. G.; Guan, Z. *J. Am. Chem. Soc.* **2007**, *129* (46), 14110–14111.

(32) Shi, H.; Shi, D.; Yin, L.; Luan, S.; Zhao, J.; Yin, J. *React. Funct. Polym.* **2010**, *70* (7), 449–455.

(33) Allcock, H. R.; Welna, D. T.; Stone, D. A. *Macromolecules* **2005**, *38* (25), 10406–10412.

(34) Lang, K.; Davis, L.; Wallace, S.; Mahesh, M.; Cox, D. J.; Blackman, M. L.; Fox, J. M.; Chin, J. W. *J. Am. Chem. Soc.* **2012**, *134* (25), 10317–10320.

(35) Higley, M. N.; Pollino, J. M.; Hollembeak, E.; Weck, M. *Chemistry* **2005**, *11* (10), 2946–2953.

(36) Scholl, M.; Ding, S.; Lee, C. W.; Grubbs, R. H. *Org. Lett.* **1999**, *1* (6), 953–956.

(37) Martinez, H.; Ren, N.; Matta, M.; Hillmyer, M. *Polym. Chem.* **2014**, *5*, 3507–3532.

(38) Lu, Y.-X.; Tournilhac, F.; Leibler, L.; Guan, Z. *J. Am. Chem. Soc.* **2012**, *134* (20), 8424–8427.

(39) Dickie, R. A.; Ferry, J. D. *J. Phys. Chem.* **1966**, *70* (8), 2594–2600.

(40) D2765-11, A. *Standard Test Methods for Determination of Gel Content and Swell Ratio of Crosslinked Ethylene Plastics*; 2011.

(41) González, A. E. *Polymer.* **1983**, *24* (1), 77–80.

(42) Leibler, L.; Rubinstein, M.; Colby, R. H. *Macromolecules* **1991**, *24* (16), 4701–4707.

(43) Mozhdehi, D.; Ayala, S.; Cromwell, O. R.; Guan, Z. *J. Am. Chem. Soc.* **2014**, *136* (46),

16128–16131.

2.5 Experimental

General materials and methods: Anhydrous solvents were purified through a column of alumina according to the method described by Pangborn *et al*. before use.[1] All commercial reagents were used as received unless otherwise noted. Flash column chromatography was performed by forced flow of indicated solvent using automated silica columns (CombiFlash, Teledyne Isco). ^{1}H NMR spectra were recorded at 500 MHz on a CRYO-500 spectrometer. ^{1}H NMR chemical shifts are reported as δ values in ppm relative to TMS or residual solvent: $CDCl_3$ (7.26 ppm; 77.0 ppm), CD_3OD (3.31 ppm; 49.0 ppm). ^{1}H NMR data are reported as follows: chemical shift in ppm, multiplicity (s = singlet, d = doublet, t = triplet, q = quartet), coupling constants in Hz, and relative integration in number of protons. Multiplets (m) are reported over the range of chemical shift at which they appear. For ^{13}C NMR, only chemical shift values are reported. Gel Permeation Chromatography (GPC) traces were obtained on an Agilent 1100 SEC system using a PLGel Mixed-C column from Polymer Labs (Amherst, MA). THF was used as eluting solvent at a flow rate of 1.0 mL/min. Number averaged and weight averaged molecular weight distributions (M_n and M_w, respectively) of samples were measured with respect to polystyrene (PS) standards purchased from Aldrich (Milwaukee, WI). Thin layer chromatography (TLC) plates were stained by $KMnO_4$ to observe the presence of double bonds.

Synthesis and characterization

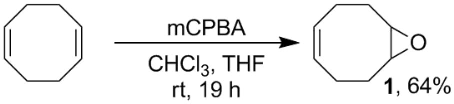

Synthesis of 1: The synthesis was carried out as previously described.[2] A solution of *m*-chloroperoxybenzoic acid (30.8 g (70% w/w), 125 mmol) in chloroform (250 mL) was added dropwise at room temperature overnight to *cis*-1,5-cyclooctadiene (21.3 g, 197 mmol) dissolved in tetrahydrofuran (24 mL). The white precipitate, *m*-chlorobenzoic acid was removed via vacuum filtration. The organic layer was washed with aqueous solutions of $NaHSO_3$ (20% w/v), $NaHCO_3$ (10% w/v), and brine. The organic layer was dried with anhydrous sodium sulfate and concentrated *in vacuo*. The crude product was purified with column chromatography (0:100 – 20:80 acetone:hexanes) to yield **1** as a colorless oil (9.98 g, 64% yield). The identity of the product was confirmed by ^{1}H NMR, ^{13}C NMR, and HRMS.

^{1}H NMR (500 MHz, $CDCl_3$) δ 5.56 (br. s, 2H), 3.03 (br. s, 2H), 2.41–2.46 (m, 2H), 2.11–2.18 (m, 2H) 1.99–2.09 (m, 6H). ^{13}C NMR (125 MHz, $CDCl_3$) δ 129.0, 56.9, 28.3, 23.9. HRMS (CI) m / z calcd for $C_8H_{12}O$ $(M + NH_4)^+$ 142.1232; found: 142.1228.

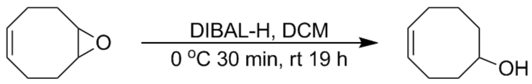

1

2, 75%

Synthesis of 2: The synthesis was adapted from a previously described procedure.[3] Under argon, a solution of **1** (10.0 g, 80.4 mmol) in anhydrous DCM (200 mL) was cooled to 0 °C. To this solution, diisobutylaluminium hydride (1.20 M in toluene, 73.6 mL, 88.4 mmol) was added dropwise. After 30 min, the reaction was warmed to room temperature and allowed to stir for 19 h. Next, the reaction was diluted with DCM (100 mL) and cooled to 0 °C. Deionized water (3.5 mL) was slowly added with vigorous stirring, followed by addition of NaOH (3.5 mL, 15% w/v) and deionized water (8.8 mL) to quench the reaction. The mixture was warmed to room temperature and vigorously stirred for 15 min. During this time, precipitates formed. Next, anhydrous sodium sulfate was added and stirred for 15 min. Finally, the salt and drying agent was removed via vacuum filtration and the reaction mixture was concentrated *in vacuo*. The crude product was purified by column chromatography (0:100 – 40:60 EtOAc:hexanes) to yield **2** as a colorless oil (7.6 g, 75% yield). The identity of the product was confirmed by ^{1}H NMR, ^{13}C NMR, COSY, HMQC, and HRMS.

^{1}H NMR (500 MHz, CDCl$_3$) δ 5.69 (appar. q, J = 8.1, 1H), 5.58 (appar. q, J = 8.2, 1H), 3.76–3.85 (br. m, 1H), 2.26–2.33 (m, 1H), 2.07–2.19 (m, 3H), 1.82–1.95 (m, 2H), 1.60–1.74 (m, 2H), 1.47–1.57 (m, 2H), 1.37 (br. s, 1H). ^{13}C NMR (125 MHz, CDCl$_3$) δ 130.3, 129.7, 72.9, 37.9, 36.4, 25.8, 25.0, 22.9. HRMS (CI) m / z calcd for C$_8$H$_{14}$O (M + NH$_4$)$^+$ 144.1388; found: 144.1394.

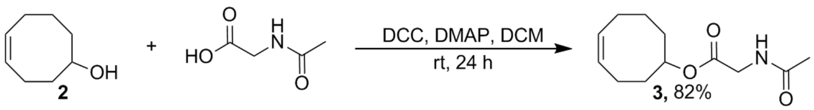

Synthesis of 3: The synthesis was adapted from a previously reported procedure.[4] Compound **2** (3.70 g, 29.3 mmol), N-acetylglycine (3.78 g, 32.3 mmol), dicyclohexylcarbodiimide (6.65 g, 32.3 mmol), and dimethylaminopyridine (0.394 g, 3.23 mmol) were dissolved in anhydrous DCM (72.5 mL) and allowed to react. After 24 h the reaction was cooled to 0 °C. The urea byproduct was removed via vacuum filtration. The filtrate was concentrated *in vacuo* and purified by column chromatography (0:100 – 60:40 acetone:hexanes). The product was then diluted in DCM and washed with saturated aqueous NaHCO3 and brine to remove starting material. The organic layer was dried with anhydrous sodium sulfate and concentrated *in vacuo* to yield **3** as a viscous oil (5.41 g, 82% yield). The identity of the product was confirmed by ^{1}H NMR, ^{13}C NMR, and HRMS.

^{1}H NMR (500 MHz, $CDCl_3$) δ 6.03 (br. s, 1H), 5.61–5.68 (m, 2H), 4.87–4.91 (m, 1H), 3.97 (d, J = 5.1, 2H), 2.30–2.37 (m, 2H), 2.06–2.18 (m, 3H), 2.03 (s, 3H), 1.84–1.91 (m, 2H), 1.66–1.75 (m, 1H), 1.60–1.65 (m, 3H). ^{13}C NMR (125 MHz, $CDCl_3$) δ 170.3, 169.6, 130.1, 129.7, 77.0, 42.0, 33.78, 33.76, 25.7, 25.0, 23.2, 22.4. HRMS (CI) m / z calcd for C12H19NO3 $(M + Na)^+$ 248.1263; found: 248.1272.

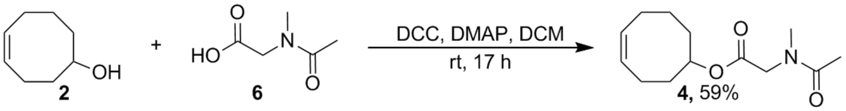

Synthesis of 4: The synthesis was adapted from a previously reported procedure.[4] Compound **2** (0.782 g, 6.20 mmol), **6** (0.898 g, 6.80 mmol), dicyclohexylcarbodiimide (1.41 g, 6.80 mmol), and dimethylaminopyridine (0.0837 g, 0.680 mmol) were dissolved in anhydrous DCM (17 mL) and allowed to react. After 17 h the reaction was cooled to 0 °C. The urea byproduct was removed via vacuum filtration. The filtrate was concentrated *in vacuo* and purified by column chromatography (0:100 – 50:50 acetone:hexanes). The product was diluted in DCM and washed with saturated aqueous $NaHCO_3$ and brine to remove excess starting material. The organic layer was dried with anhydrous sodium sulfate and concentrated *in vacuo* to yield **4** as a clear liquid (0.88 g, 59% yield). The identity of the product was confirmed by ^1H NMR, ^{13}C NMR, and HRMS. Analysis of NMR spectra revealed the presence of two amide bond rotamers. These conformational isomers have been observed and studied in similar compounds.[5] The minor distinguishable rotamer peak is denoted with *.

^1H NMR (500 MHz, $CDCl_3$) δ 5.61–5.70 (m, 2H), 4.86–4.90 (m, 1H), 4.02–4.11/3.97* (m, 2H), 3.07/2.96* (s, 3H), 2.32–2.34 (m, 1H), 2.04–2.18 (m, 6H), 1.81–1.92 (m, 2H), 1.64–1.79 (m, 1H), 1.50–1.64 (m, 3H). ^{13}C NMR (125 MHz, $CDCl_3$) δ 171.4/171.2*, 168.9/168.4*, 130.0, 129.6, 77.6, 53.0*/49.7, 37.4/34.9*, 33.8, 33.7, 25.7, 24.9, 22.3, 21.5/21.4*. HRMS (CI) m / z calcd for $C_{13}H_{21}NO_3$ $(M + H)^+$ 240.1600; found: 240.1595.

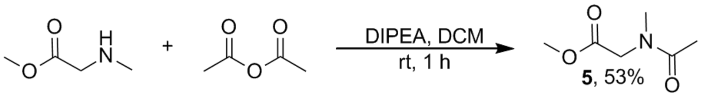

Synthesis of 5: Sarcosine methyl ester hydrochloride (10.1 g, 71.6 mmol) was dispersed in anhydrous DCM (140 mL). After addition of diisopropylethylamine (31.2 mL, 179 mmol), acetic anhydride was added dropwise over 5 min at room temperature (7.43 mL, 78.8 mmol). Upon addition of acetic anhydride, the contents completely dissolved. After 1 h, the reaction was diluted with DCM and washed with saturated aqueous $NaHCO_3$ and brine. The organic layer was dried with anhydrous sodium sulfate and concentrated *in vacuo* to yield **5** as a liquid (5.26 g, 53% yield). The identity of the product was confirmed by ^{1}H NMR, ^{13}C NMR, and HRMS. As in **4**, the minor distinguishable rotamer peak is denoted with *.

^{1}H NMR (500 MHz, $CDCl_3$) δ 4.12/4.03* (s, 2H), 3.77*/3.72 (s, 3H), 3.08/2.96* (s, 3H), 2.14/2.04* (s, 3H). ^{13}C NMR (125 MHz, $CDCl_3$) δ 171.5, 170.0/169.6*, 52.5*/52.2, 49.2, 37.4/34.8*, 21.5/21.4*. HRMS (CI) m / z calcd for $C_6H_{11}NO_3$ $(M + Na)^+$ 168.0637; found: 168.0639.

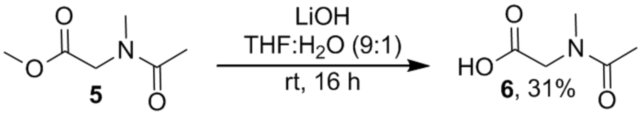

Synthesis of 6: Compound **5** (9.05 g, 62.3 mmol) was dissolved in a mixture of THF and H2O (120 mL, 9:1 THF:H2O). Lithium hydroxide monohydrate (3.90 g, 93.1) was added with stirring and allowed to react for 16 h. Next, THF was removed *in vacuo* and the residual water layer was chilled to 0 °C and acidified (pH = 2). The H2O layer was concentrated *in vacuo* and then extracted with EtOAc. The organic layer was dried with anhydrous sodium sulfate and concentrated *in vacuo* to yield **6** as a white solid (2.54 g, 31% yield). Similar to **4**, the minor distinguishable rotamer peak is denoted with *.

^{1}H NMR (500 MHz, MeOH) δ 4.17*/4.09 (s, 2H), 3.11/2.94* (s, 3H), 2.13/2.04* (s, 3H). ^{13}C NMR (125 MHz, $CDCl_3$) δ 174.3*/174.1 172.6/172.3*, 53.0*/50.1, 37.8/35.1*, 21.3/21.1*. HRMS (ES+) m / z calcd for $C_5H_9NO_3$ $(M + Na)^+$ 154.0480; found: 154.0488.

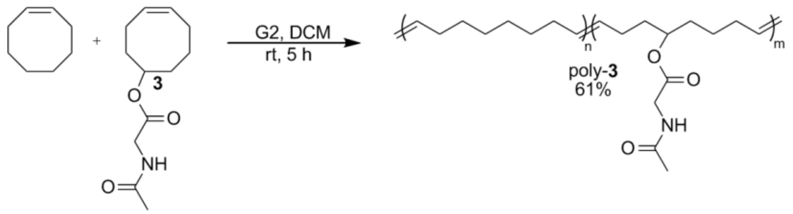

Representative ring opening metathesis polymerization procedure: (shown here for poly-**3**) Cyclooctene was purified via vacuum distillation before use. Compound **3** (5.00 g, 22.2 mmol) and cyclooctene (CO) (8.19 g, 74.3 mmol) were mixed with 25 mL of anhydrous DCM. In a flame-dried round bottom flask, Grubbs' second generation catalyst (G2) (16.0 mg, 19.0 μmol, [monomers]/[cat.] = 5000) was dissolved in anhydrous DCM (200 mL). The DCM solution of monomer was added over five min to the round bottom flask and allowed to react for 5 h at room temperature under air. The polymerization was quenched by addition of ethyl vinyl ether (1.0 mL) to the mixture. The polymer was obtained by precipitation from methanol to yield poly-**3** (8.04 g, 61% yield). The copolymer was characterized by ^{1}H NMR and GPC. The monomer incorporation ratio was determined by ^{1}H NMR, where integration of the olefin proton resonances (5.30 ppm) were set to 2H and the corresponding integration of the methine proton (4.95 ppm) was taken as the percentage of functionalized monomer.

^{1}H NMR (500 MHz, $CDCl_3$) δ 6.01 (br. s, 0.17H), 5.25–5.45 (m, 2H), 4.95 (br. s, 0.18H), 4.02 (d, J = 4.7, 0.36H), 2.03 (s, 0.54H), 1.85–2.10 (m, 4H), 1.50–1.68 (m, 0.72H), 1.30 (m, 6.92H).

Representative Cross-Linking Procedure: The cross-linking procedure was adapted from a previously described protocol.[6] After precipitation, the copolymer of CO and **3** (poly-**3**) was redissolved in dichloromethane (DCM) (380 mL). Three aliquots (1.5 mL) of the poly-**3**/DCM solution were collected and dried to calculate total polymer mass (8.04 g). Dicumyl peroxide (0.048 g, 0.178 mmol, [olefin]/[peroxide] = 333) was added to the DCM solution with stirring. The polymer solution was cast in Teflon molds via slow evaporation overnight. The polymer was melt pressed (100 °C) to remove defects and form testable samples. Poly-**3** was cross-linked at 150 °C for 2 h *in vacuo*. Finally, the mass of each sample was recorded and subsequently swelled in anhydrous DCM overnight to remove unreacted dicumyl peroxide.

Incorporation of G2: The G2 incorporation procedure was adapted from a previously described protocol.[6] After being swelled in anhydrous DCM overnight, the swollen mass of each sample was recorded. The difference in mass between the swollen and dried sample was used to calculate the volume of DCM in each sample. Samples were soaked in a DCM solution of G2 to incorporate the metathesis catalyst ([olefin]/[catalyst] = 2000) into the polymer network. Swollen samples were equilibrated in G2/DCM solution for 1 h in an ethylene glycol/dry ice bath (−16 °C) and subsequently dried *in vacuo* for 2 h at room temperature.

Calculating swell ratio: The swelling ratio was calculated following a protocol developed by the American Society for Testing and Materials (ASTM).[7] After cross-linking, samples were swollen and washed in DCM to remove unreacted dicumyl peroxide. Next, the samples were dried *in vacuo* and the dried mass was recorded. The dried samples were again swollen in DCM for 24 h and the swollen mass was recorded. The density of the polymer was calculated using the mass of a dried sample and the volume of that sample measured with electronic calipers. The swelling ratio was calculated in triplicate. The following equation was used to calculate the swell ratio:

$$\text{Swell ratio} = \left[\frac{W_g - W_d}{W_d}\right] K + 1$$

where:
W_g = weight of swollen gel after immersion period
W_d = weight of dried gel
K = ratio of density of polymer to that of the solvent at the immersion temperature

Uniaxial Tensile Testing: The mechanical properties of polymer samples were measured using an Instron 3365 machine. Standard stress/strain experiments were performed on samples at room temperature. Samples were extended at a rate of 100 mm/min. Each measurement was performed in triplicate to ensure reproducibility. Uncut samples were heated at 50 °C for 3 h to act as pristine controls for healing experiments. The average sample size was 15 mm × 7 mm × 2 mm (length, width, thickness).

Rheological Studies: Rheology data were collected on an AR-G2 rheometer from TA Instruments (20 mm Peltier plate with no solvent trap, stainless steel, 2800 μm gap width). The instrument was equipped with Peltier temperature control system. Frequency sweep experiments were performed at 0.1% strain by varying the frequency between 10 and 628 rad/s at 10−90 °C for each polymer system. Rheological data were reported from 10 to 50 °C. Temperature was increased at increments of 10 °C with 10 min soak time to ensure the complete equilibration of sample temperature.

Cyclic Tensile Testing: The cyclic tensile test was performed using an Instron 3365 machine. Before the experiment, the length of the ACON sample (with no G2 incorporation) was measured. Next, the sample was loaded, unloaded, and immediately reloaded 10 times to 300% extensibility at room temperature. The loading rate remained constant at 100 mm/min. After the initial 10 cycles, the sample was removed from the clamp and allowed to relax at room temperature for 30 min. After the equilibration period, the length of the ACON sample was again measured and found to have relaxed to its original length. An 11th loading cycle was completed to measure the recovery of energy dissipative properties.

Self-Healing Procedure: Samples were cut with a fresh blade (75% of width) through the center and subsequently pushed back together for 1 min. Samples were left to stand in air for the duration of the experiment at 50 °C. Pristine samples were not cut but carried through an otherwise identical procedure. Samples were allowed to equilibrate to room temperature for 10 min before uniaxial tensile testing. Each measurement was performed in triplicate to ensure reproducibility.

Thermal characterization: Differential scanning calorimetry (DSC) was performed using a TA Q800. Non-cross-linked polymers of ACON and BACON (5-10 mg) were placed in a non-hermetic pan and scanned against an empty reference. A heat-cool-heat cycle was used. The sample temperature was ramped to 180 °C at a rate of 10 °C/min to remove thermal history. Next, the sample was cooled to –80 °C at a rate of 20 °C/min. After an isotherm at –80 °C for 10 min, the sample temperature was ramped to 200 °C at 5 °C/min.

Differential scanning calorimetry of bulk poly-**3** and poly-**4**:

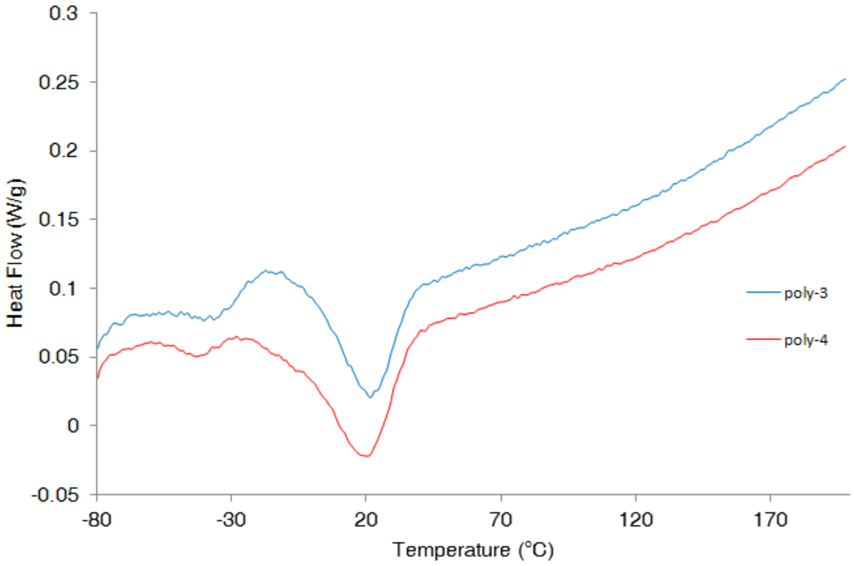

2.6 References for Experimental

(1) Pangborn, A. B.; Giardello, M. A.; Grubbs, R. H.; Rosen, R. K.; Timmers, F. J. *Organometallics* **1996**, *15* (5), 1518–1520.

(2) Allcock, H. R.; Welna, D. T.; Stone, D. A. *Macromolecules* **2005**, *38* (25), 10406–10412.

(3) Lang, K.; Davis, L.; Wallace, S.; Mahesh, M.; Cox, D. J.; Blackman, M. L.; Fox, J. M.; Chin, J. W. *J. Am. Chem. Soc.* **2012**, *134* (25), 10317–10320.

(4) Higley, M. N.; Pollino, J. M.; Hollembeak, E.; Weck, M. *Chemistry* **2005**, *11* (10), 2946–2953.

(5) Laursen, J. S.; Engel-Andreasen, J.; Fristrup, P.; Harris, P.; Olsen, C. A. *J. Am. Chem. Soc.* **2013**, *135* (7), 2835–2844.

(6) Lu, Y.-X.; Tournilhac, F.; Leibler, L.; Guan, Z. *J. Am. Chem. Soc.* **2012**, *134* (20), 8424–8427.

(7) D2765-11, A. *Standard Test Methods for Determination of Gel Content and Swell Ratio of Crosslinked Ethylene Plastics*; 2011.

2.7 Chapter 2 Spectra

Compound 1. ^{1}H NMR (500 MHz, $CDCl_3$, 298 K)

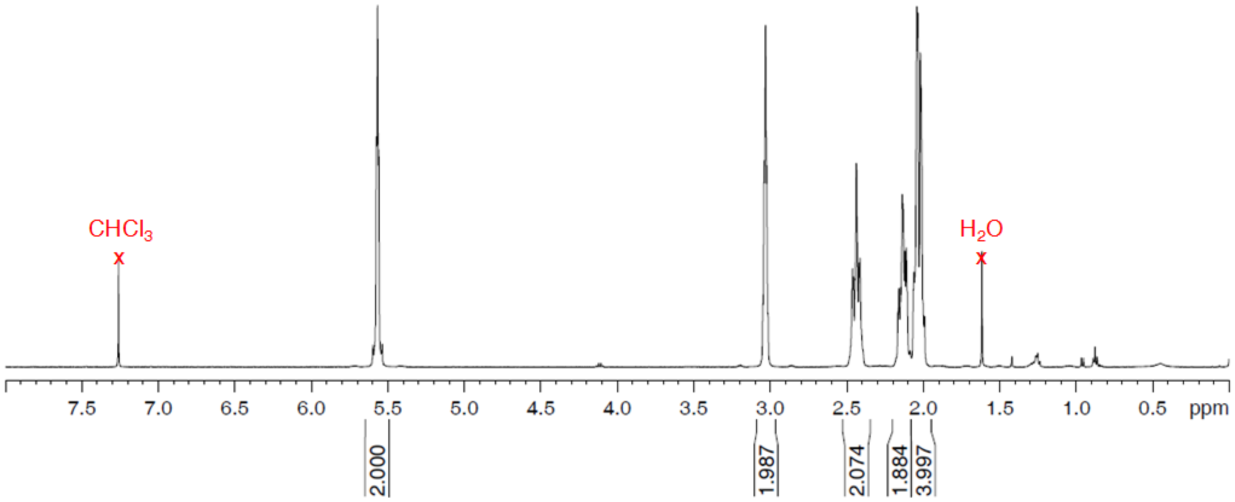

Compound 1. ^{13}C NMR (125 MHz, $CDCl_3$, 298 K)

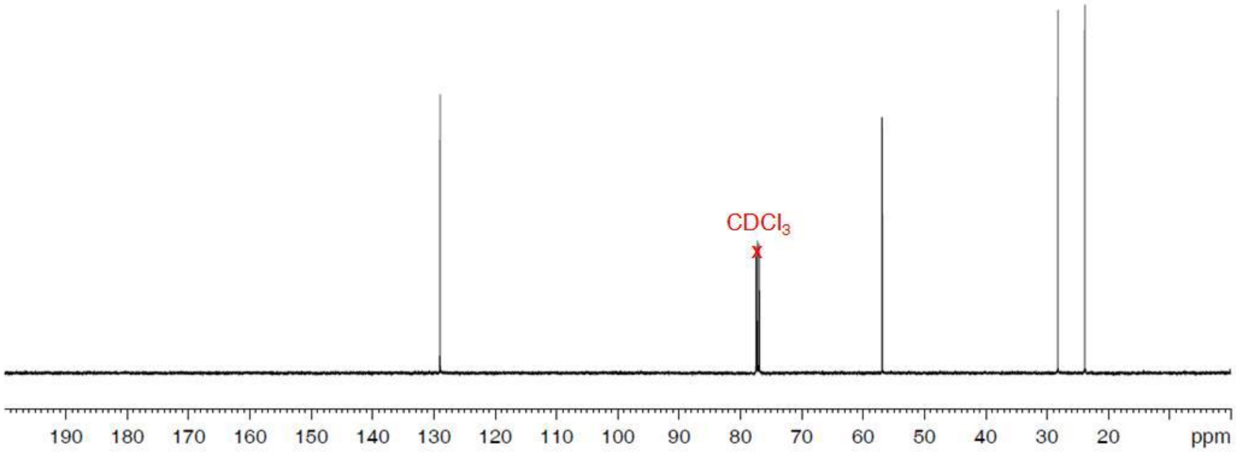

Compound 2. ^{1}H NMR (500 MHz, CDCl$_3$, 298 K)

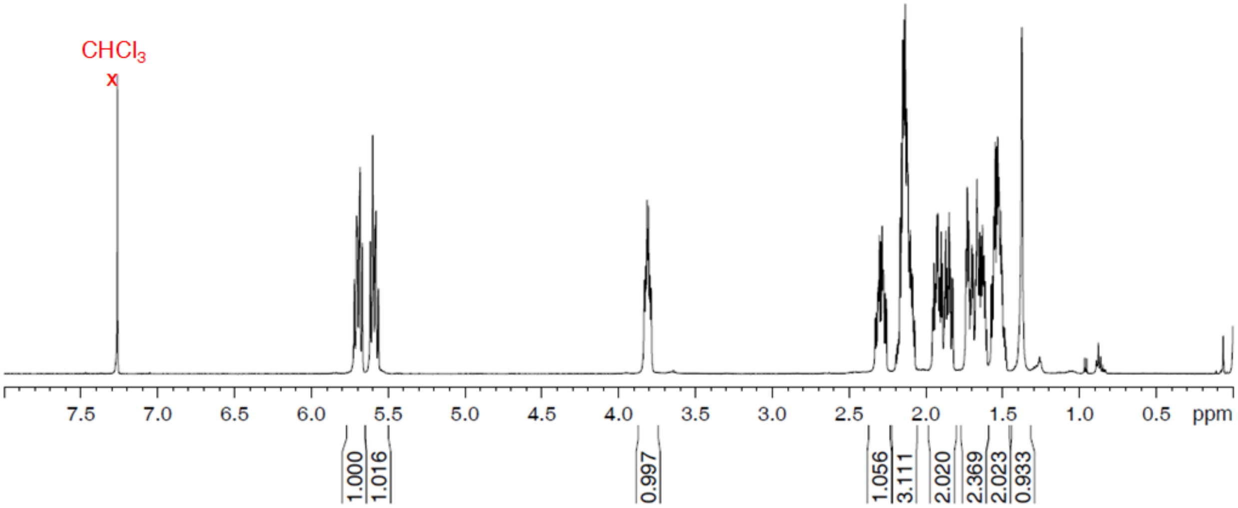

Compound 2. ^{13}C NMR (125 MHz, CDCl$_3$, 298 K)

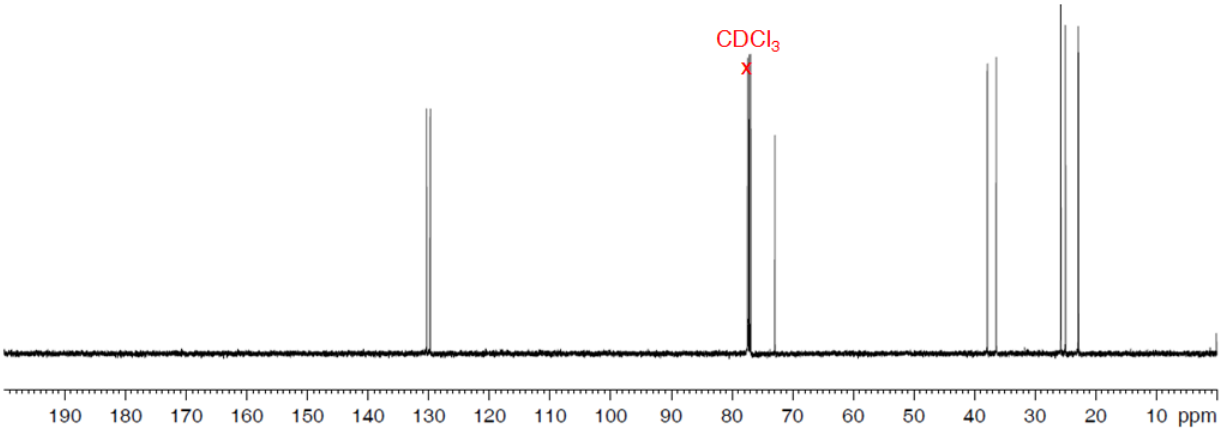

Compound 2. COSY (500 MHz, $CDCl_3$, 298 K)

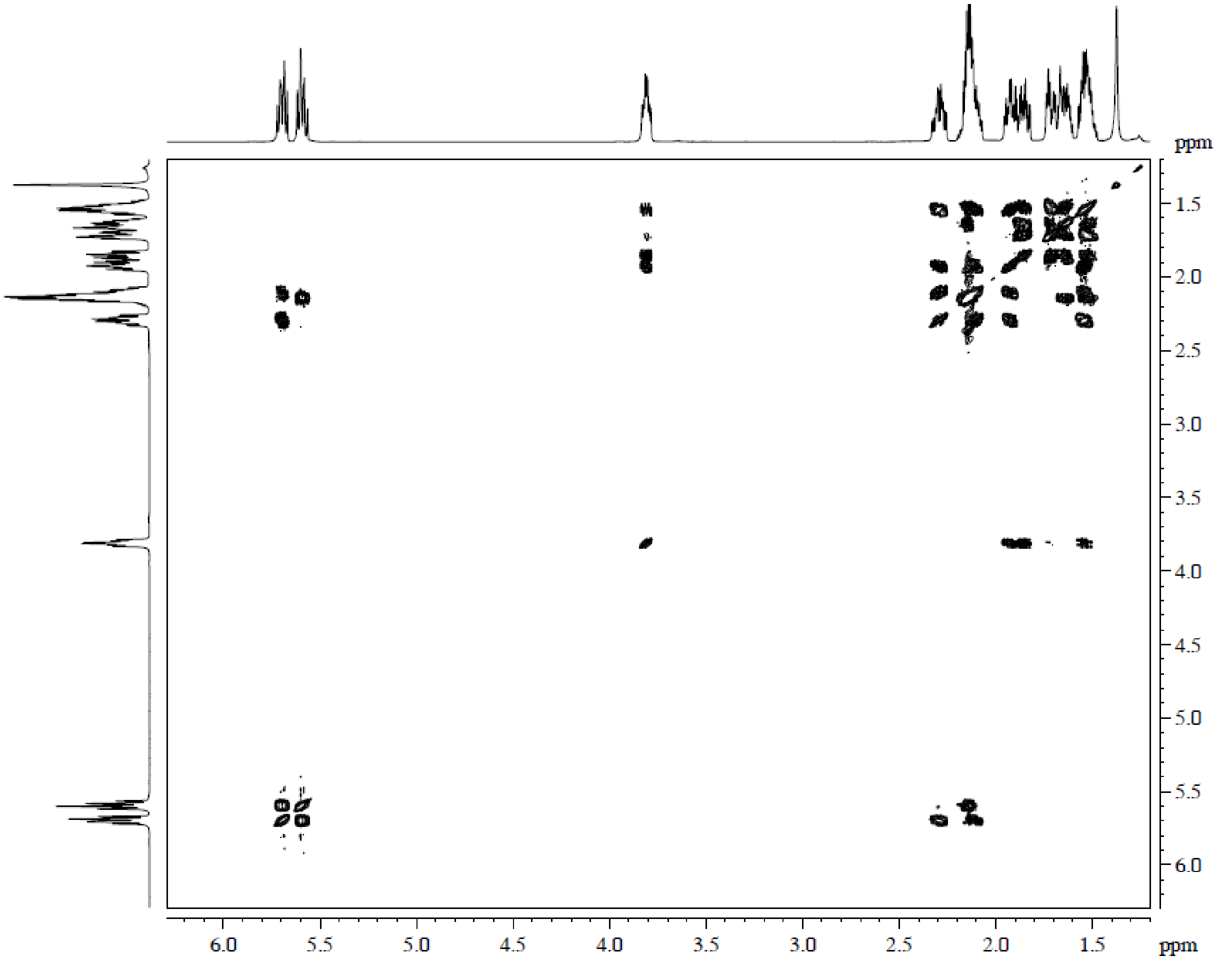

Compound 2. COSY (500 MHz, $CDCl_3$, 298 K)

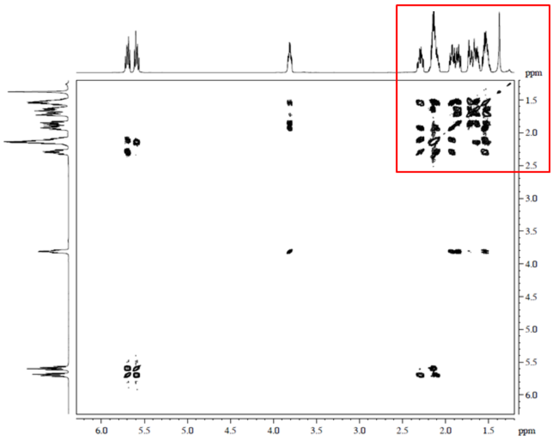

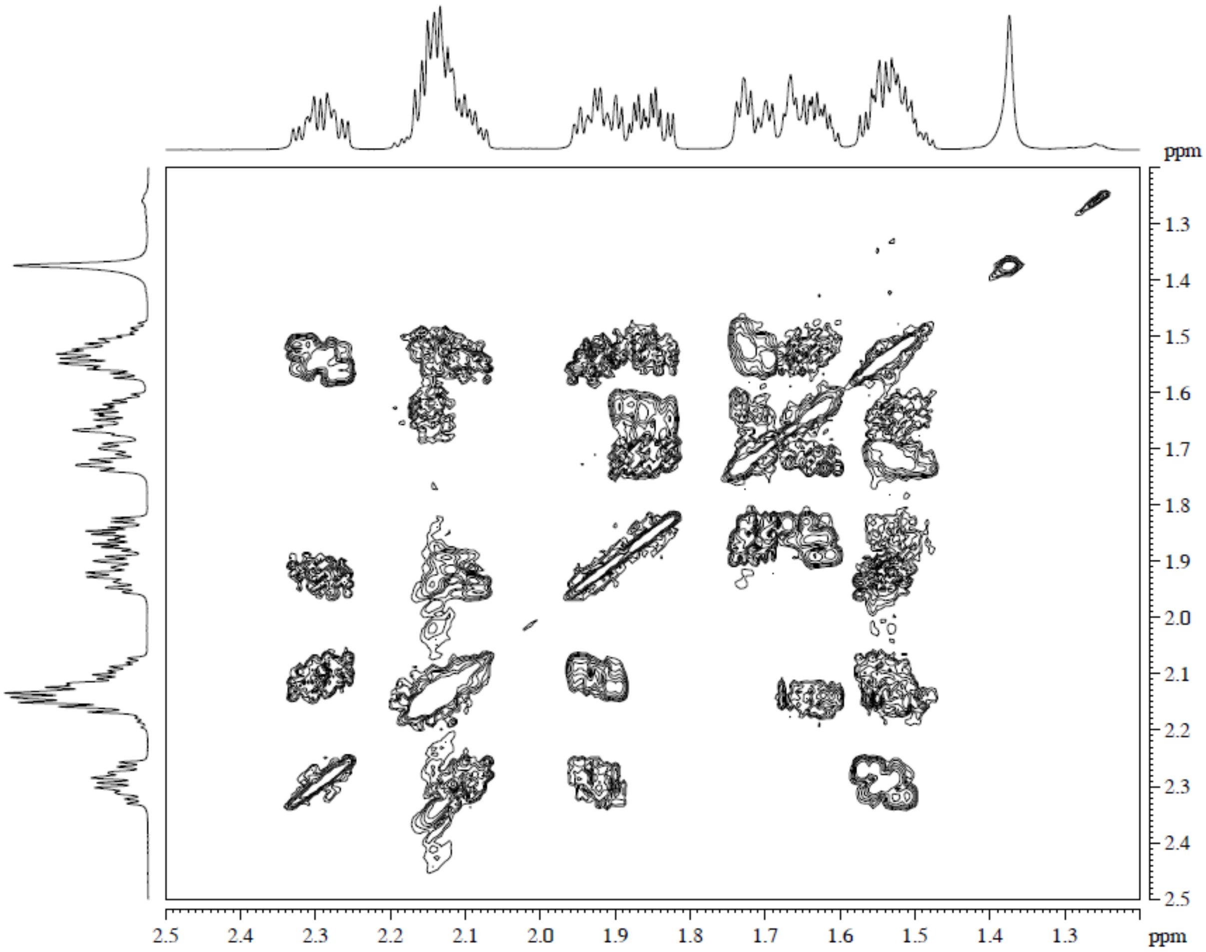

Compound 2. HMQC ($CDCl_3$, 298 K)

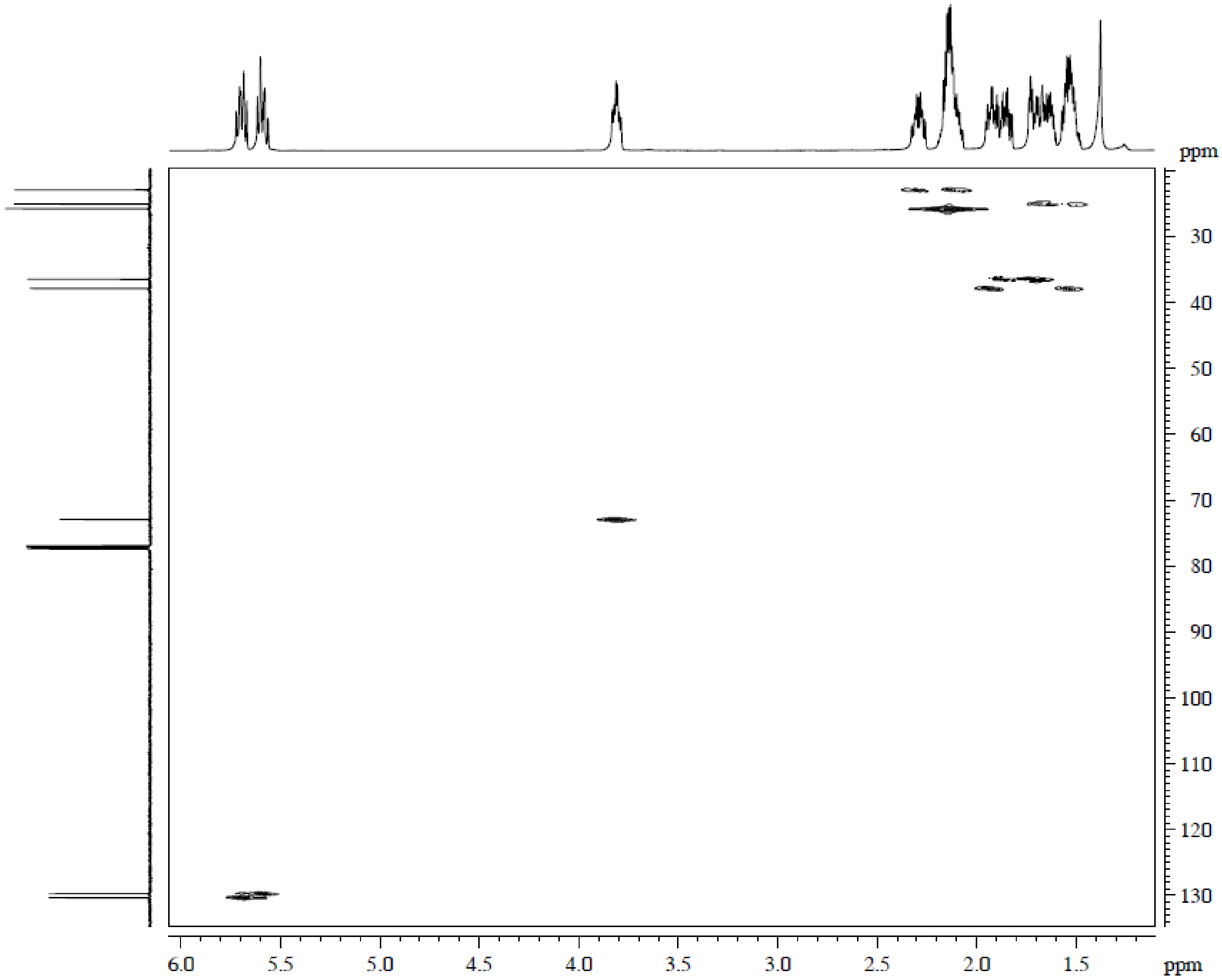

Compound 3. ^{1}H NMR (500 MHz, $CDCl_3$, 298 K)

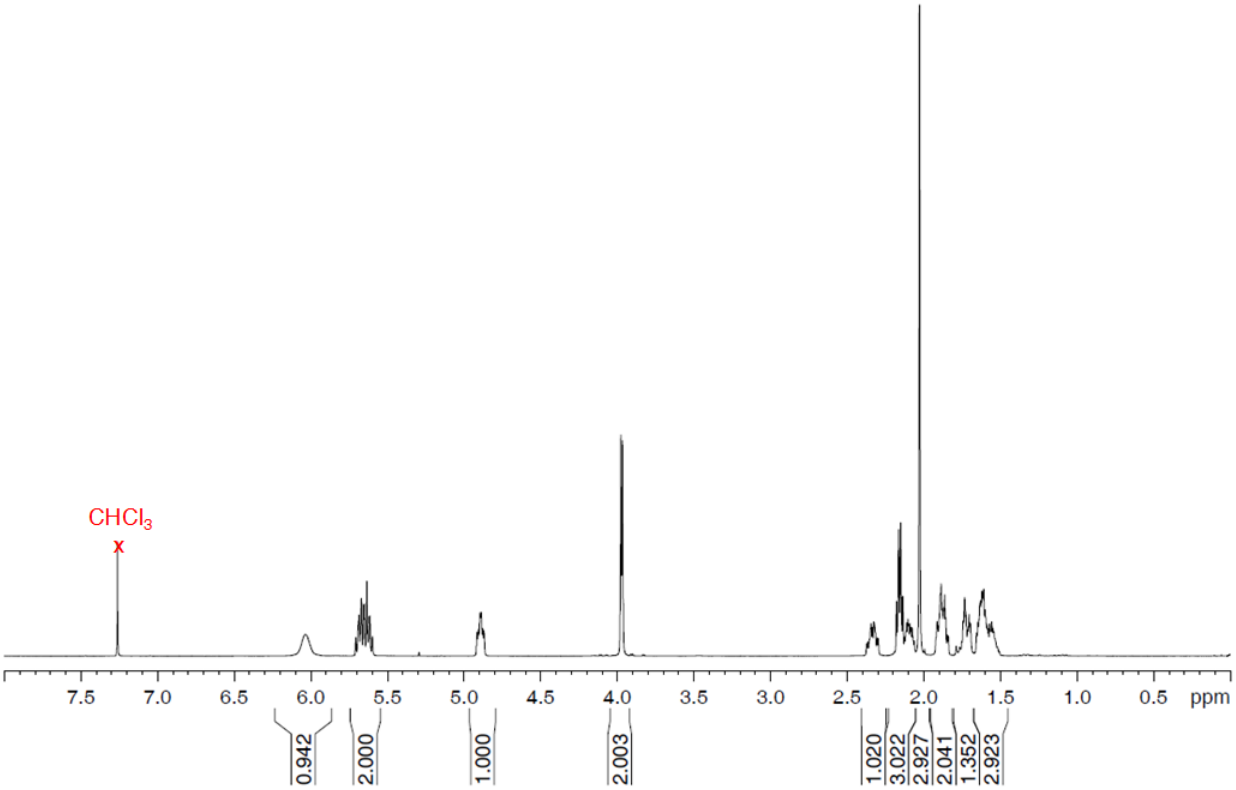

Compound 3. ^{13}C NMR (125 MHz, $CDCl_3$, 298 K)

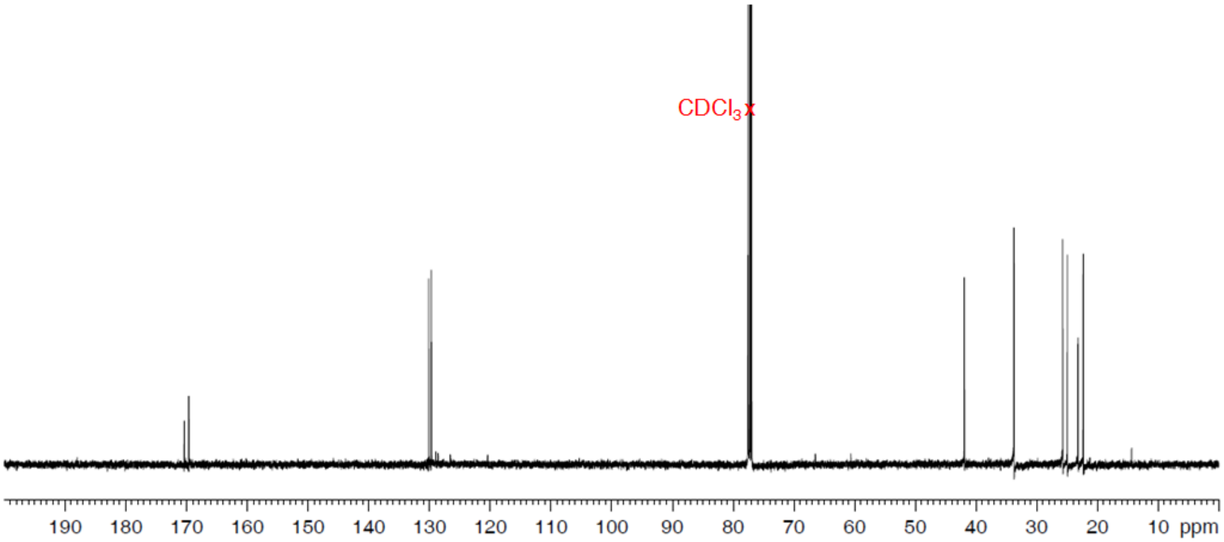

Compound 4. ^{1}H NMR (500 MHz, $CDCl_3$, 298 K)

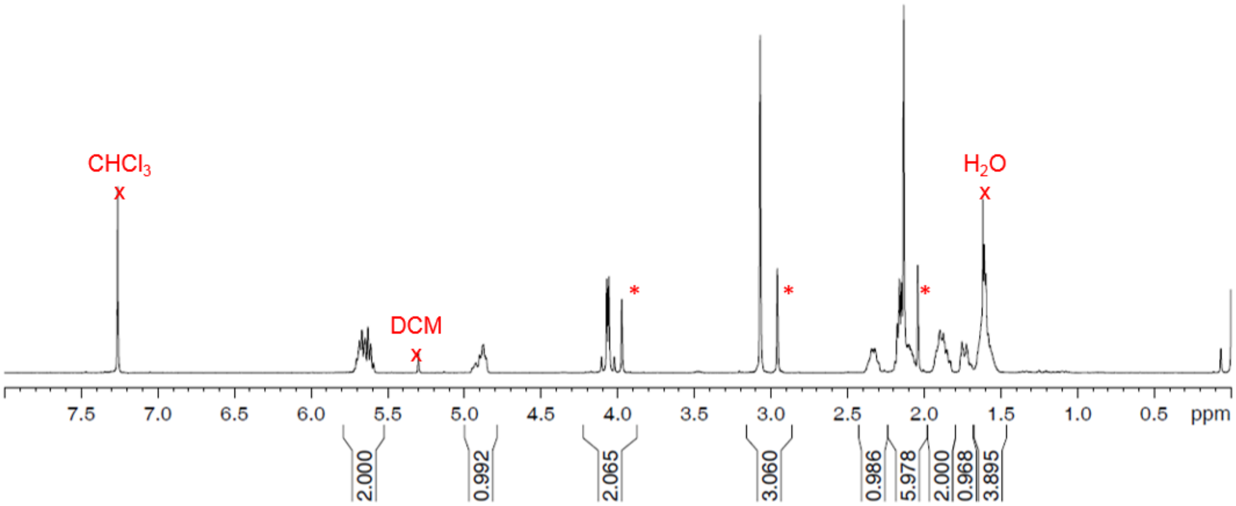

Compound 4. ^{13}C NMR (125 MHz, $CDCl_3$, 298 K)

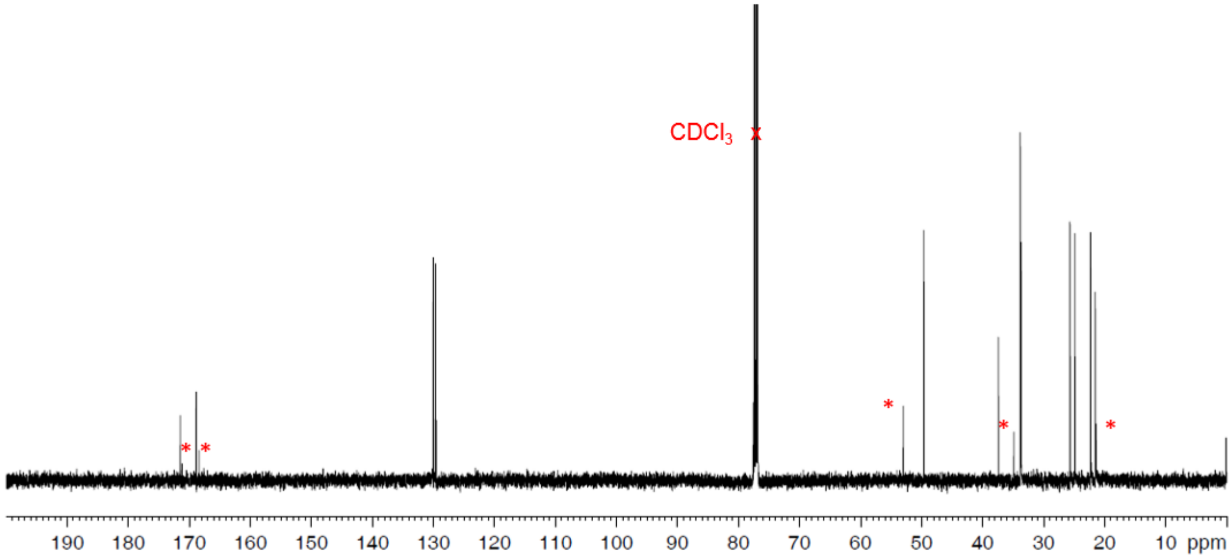

Compound 5. ^{1}H NMR (500 MHz, $CDCl_3$, 298 K)

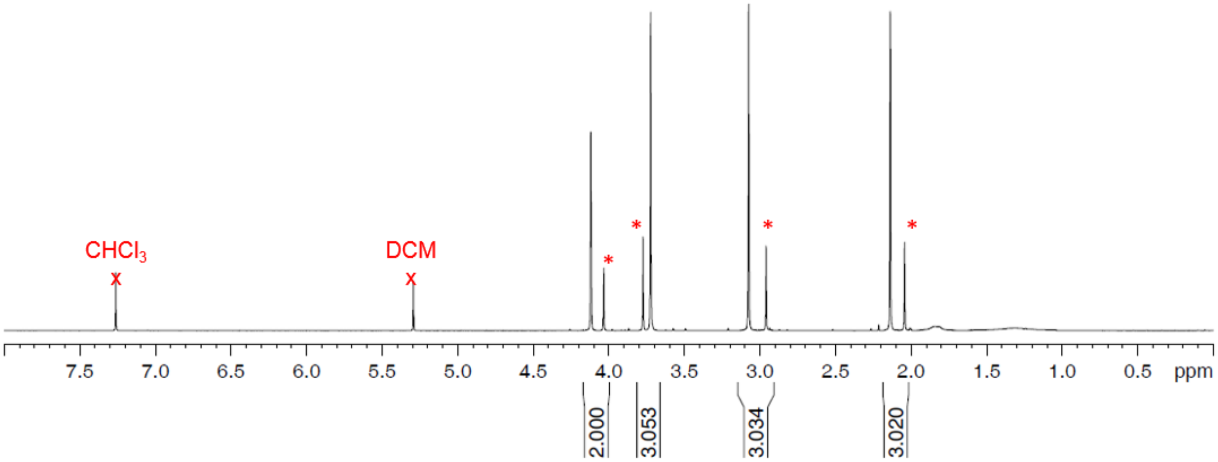

Compound 5. ^{13}C NMR (125 MHz, $CDCl_3$, 298 K)

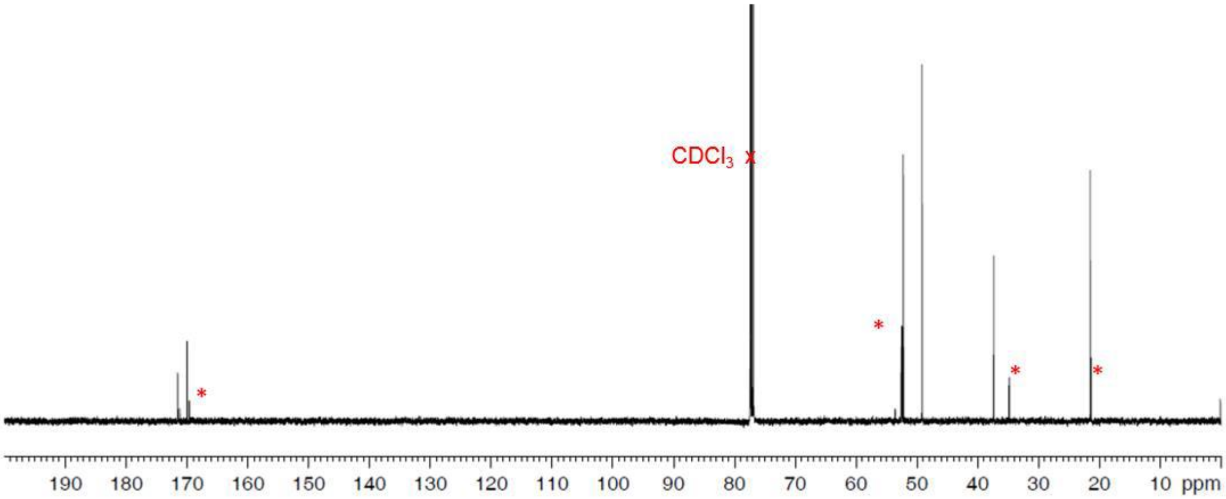

Compound 6. ¹H NMR (500 MHz, $CDCl_3$, 298 K)

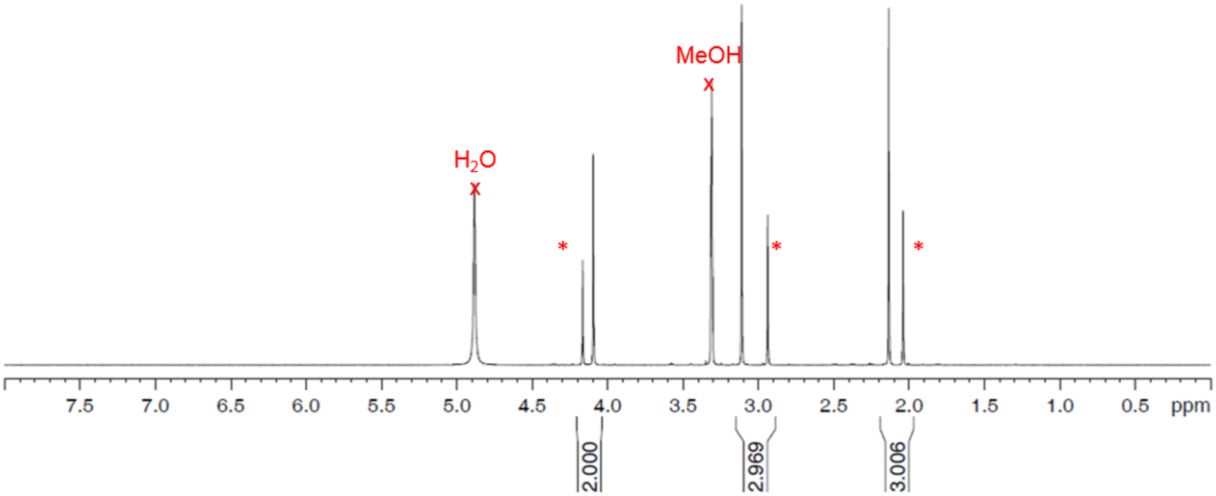

Compound 6. ¹³C NMR (125 MHz, $CDCl_3$, 298 K)

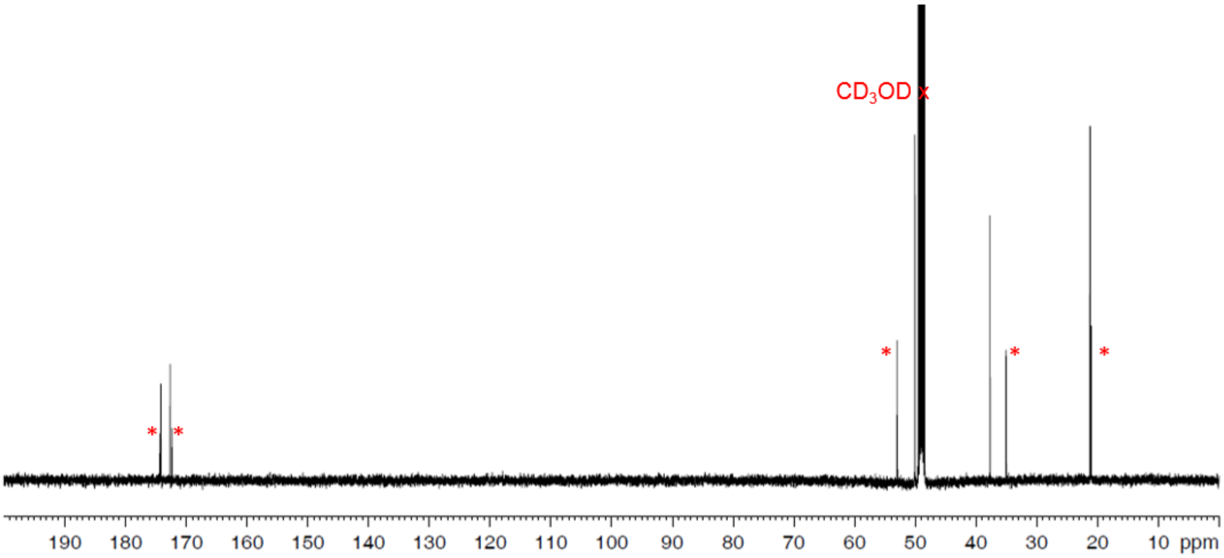

Poly-3. ^{1}H NMR (500 MHz, $CDCl_3$, 298 K)

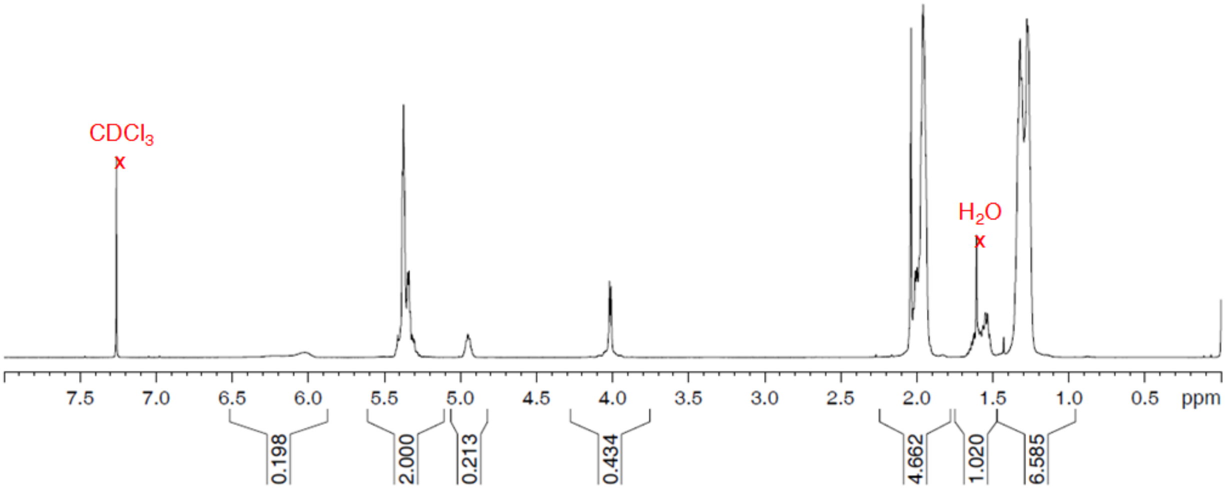

GPC trace of poly-3. GPC (THF eluent, PS standard) M_w: 266 kDa M_n: 155 kDa, M_w/M_n: 1.69

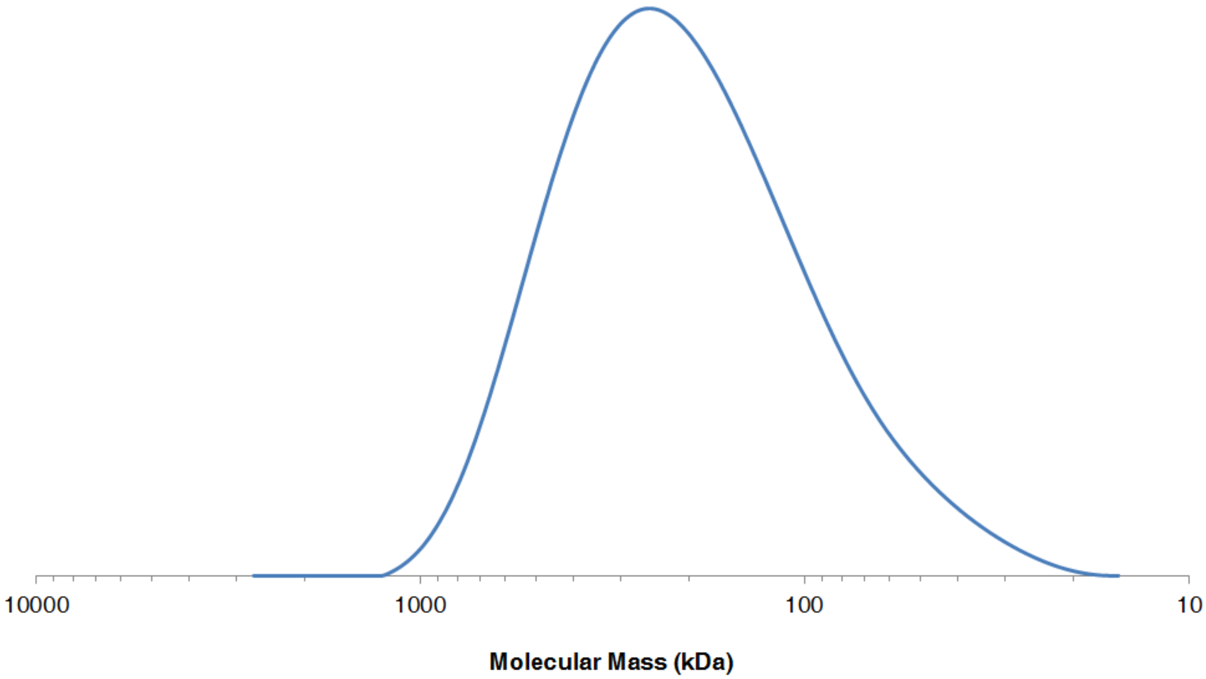

Poly-4. ^{1}H NMR (500 MHz, $CDCl_3$, 298 K)

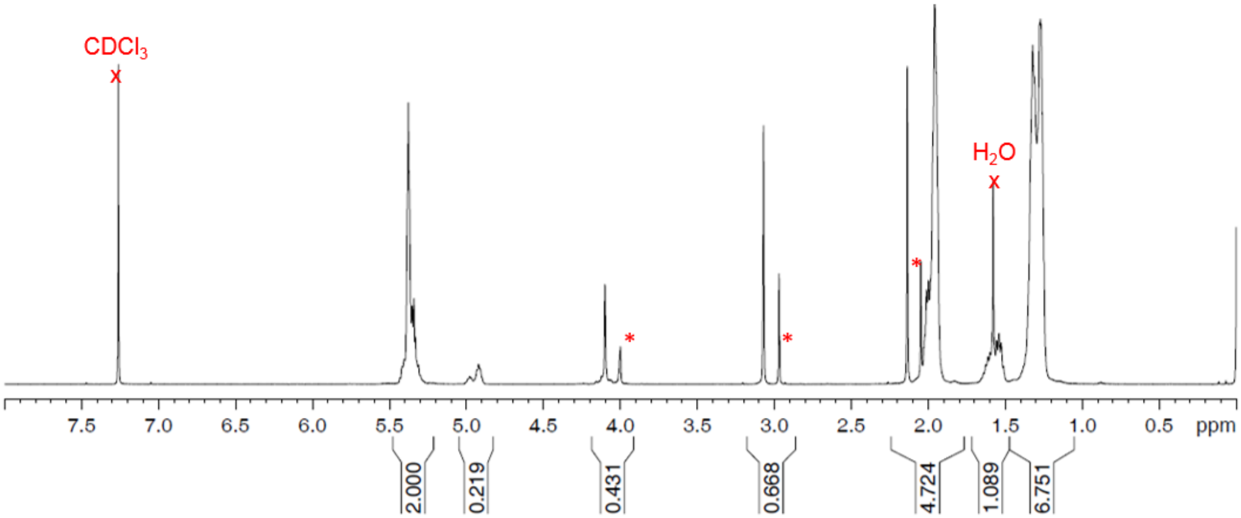

GPC trace of poly-4. GPC (THF eluent, PS standard) M_w: 330 kDa M_n: 157 kDa, M_w/M_n: 2.10

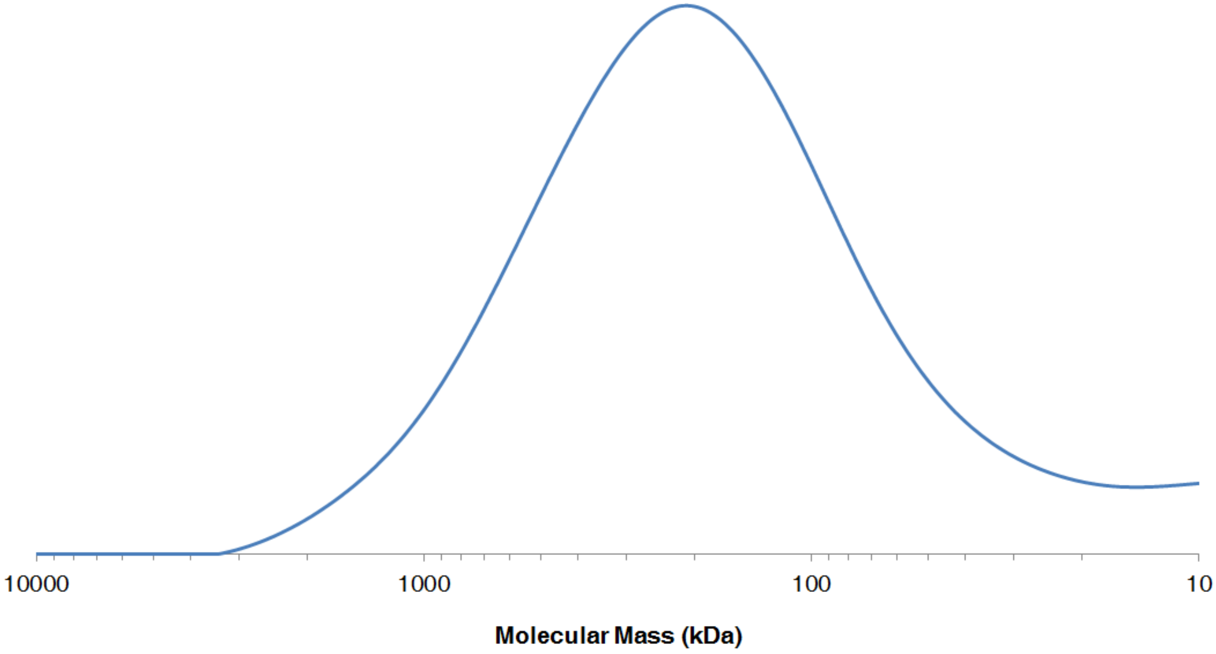

Chapter 3: Tuning Dynamic Mechanical Response in Metallopolymer Networks through Simultaneous Control of Structural and Temporal Properties of the Networks

3.1 Introduction

3.1.1 The state of tunable metallopolymers

The ability to easily tune the mechanical and dynamic properties of a polymeric material has important implications for technological and biomedical applications.[1–4] A common strategy to control a material's response under static and dynamic load is to use reversible interactions, such as H-bond,[5–8] ionic,[9–11] π−π,[12] and metal−ligand[13–24] (M−L) interactions as dynamic cross-linkers.[25] It is, however, challenging to achieve the desired mechanical properties by a priori design and without extensive synthetic modifications of polymers.

M−L interactions are uniquely suited to engineer desired mechanical properties from a ligand-containing polymer without the need for synthetic modifications of the backbone.[26–28] First, metal ions can react with multiple ligands to form well-defined molecular entities with controllable and predictable stereochemical arrangements and coordination numbers. In contrast, simple hydrogen bond donors and acceptors or ion pairs tend to form either pairwise junctions or aggregates with ill-defined stoichiometry. Second, the kinetics of M−L exchange can be easily tuned across a broad range by changing the type of metal ion and/or the oxidation state of the metal.[29–31] Third, ligand exchange reactions can occur through mechanistic pathways with either associative or dissociative character.[29] In contrast, the kinetics of exchange for hydrogen bonds and ion pairs are not easily modulated, and the exchange reaction generally occurs through the dissociation of a bound pair. Because of these unique properties of M−L interactions, it is possible to tune the mechanical response of ligand-containing polymers by simply selecting the type and amount of added metal cross-linker. One can rationally modulate the mechanical properties through controlling the topology and the exchange dynamics of cross-linkers by understanding the dynamic M−L cross-linker at the molecular level.

Despite the surge of interest in designing polymeric materials based on new M−L complexes, variables such as preferred coordination number, ligand exchange kinetics/mechanism, and the ligand-to-metal (L/M) stoichiometric ratio are often overlooked through restrictive polymeric designs. For example, many of the previously reported M−L systems rely on supramolecular assemblies of end-capped oligomers, necessitating a nearly balanced L/M ratio to achieve robust mechanical properties. Furthermore, many systems rely on multidentate ligands that bind strongly to metal centers, limiting the accessible ligand exchange mechanisms. Additionally, these chelating ligands form complexes with well-defined stoichiometry, irrespective of the initial ratio of ligand to metal.[13,32–35]

3.1.2 Our design for a tunable, dynamic metallopolymer

In contrast to these previous studies, here we aimed to develop a simple, new strategy for tuning mechanical properties in dynamic metallopolymer networks through M−L coordination geometry and ligand exchange dynamics. Specifically, we chose to study the emergent bulk mechanical properties of imidazole-containing polymers (ICPs) dynamically cross-linked by Co^{2+}, Zn^{2+}, or Cu^{2+} through systematic variation in the L/M ratio (Figure 3.1a). Unlike previous reports of bi- and tridentate ligands, imidazole is a monodentate ligand that can transiently bind to these transition metal ions. The three metal ions were selected because they are all of similar ionic radius and electrostatic charge, making them suitable for comparative study. Additionally, they possess different coordination numbers and geometry,[36–41] allowing us to discern how these coordination parameters may impact the emergent material properties. In particular, we can control the relative abundance of unbound ligands and cross-linkers by varying the L/M ratio (Figure 3.1b). While these unbound ligands are traditionally classified as mechanically inactive dangling chains, we envisioned an active role for them in facilitating the cross-linker exchange dynamics. Specifically, the presence of unbound ligands affects the network relaxation behavior in a different manner depending on the preferred ligand exchange mechanism[42,43] of the mechanically active M−L cross-linking complex (Figure 3.1c). Accordingly, unbound ligands can play a critical role in overall network relaxation behavior and hence the materials' dynamic mechanical properties.

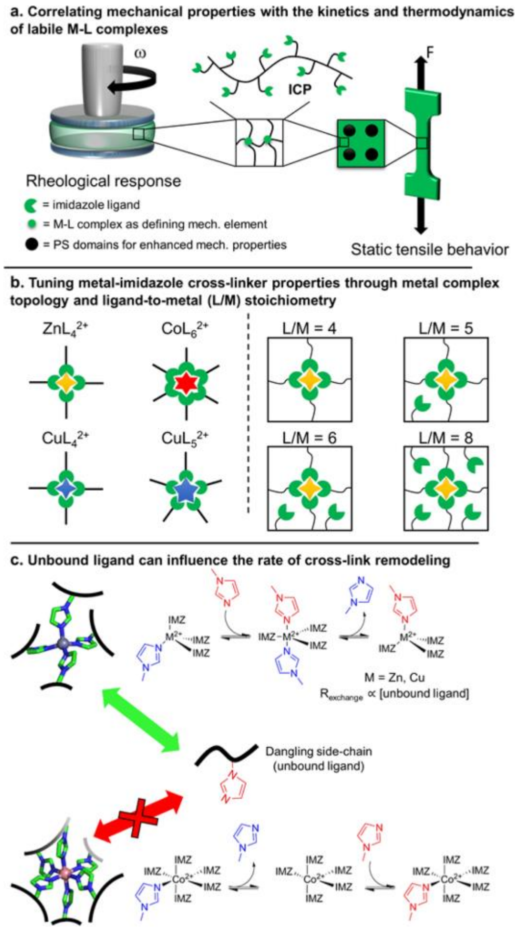

Figure 3.1 Monodentate metallopolymer design concept. (a) M−L complexes control the mechanical response of an imidazole-containing polymer (ICP) under dynamic and static load. (b) Crosslinker properties can by tuned by the identity of the metal (which influences preferred coordination number and ligand exchange mechanism) and the ligand-to-metal (L/M) stoichiometric ratio (which simultaneously adjusts the concentration of cross-linkers and unbound ligands). (c) At the molecular level, the presence of unbound ligands can facilitate ligand exchange dynamics depending on the M−L complex. Accordingly, for associative exchange the unbound ligands can affect the dynamics of the cross-linking exchange leading to stress redistribution and the protection of the covalent network from damage under load.

In this study, we demonstrate these concepts by tuning the mechanical properties of ICPs from viscous fluids to stiff plastics (Young's modulus in the range of 100 MPa) by simply changing the type and amount of added metal ion (L/M ratio). Through rheological study of a model system, we correlate bulk network relaxation at different L/M ratios to molecular parameters such as coordination number and preferred ligand exchange mechanism. In particular, we demonstrate that the presence of unbound ligands could significantly increase the rate of cross-link exchange depending on the metal center preferred exchange mechanism. Consequently, the bulk mechanical properties are not solely dependent on the cross-link density and can be significantly influenced by the contribution of unbound ligands to the kinetics of the relaxation process. Our tensile experiments further establish that this underexplored contribution of unbound ligands is critically important for stress distribution and chain relaxation, which ultimately governs the material's failure under load. To the best of our knowledge, this represents the first strategy for the simultaneous control of both the structure of networks (coordination geometry and topology) and the temporal response (ligand exchange-induced relaxation kinetics) of bulk materials using dynamic associations of weak and monodentate ligands with transition metals. The direct correlation of bulk mechanical properties to molecular structure and ligand exchange mechanisms provides critical insights into the contribution of M−L interactions and paves the road toward de novo design of functional materials with advanced properties.[33,44]

3.2 Results and Discussion

3.2.1 Synthesis and characterization

Two polymer architectures were included in this study: a short, linear imidazole-containing polymer (L-ICP) for solution and melt rheological studies and a brush copolymer having a polystyrene (PS) backbone grafted with multiple imidazole-containing polymers (B-ICP) for bulk mechanical property investigation (Scheme 3.1). The L-ICP system served as a good model for solution and melt rheological studies to build basic structure–property correlations between small molecule M–L complexes and mechanical properties. The B-ICP system was used to correlate the tensile mechanical and self-healing properties to M–L thermodynamic and kinetic parameters. In bulk, glassy PS in B-ICPs microphase separates into hard nanodomains embedded in the soft brush matrix, producing thermoplastic elastomers that are amenable for standard tensile mechanical testing.

The syntheses of imidazole-containing acrylate monomer (IMZa) and polymers (ICP) were reported previously.[45] Briefly, IMZa was synthesized via a stoichiometrically controlled Michael addition reaction (Scheme 3.1a). This monomer was copolymerized with butyl acrylate (BA) in a controlled reversible addition–fragmentation chain-transfer (RAFT) polymerization[46] using different chain transfer agents to yield two polymers with comparable imidazole content but different architectures. The random copolymer L-ICP was synthesized using a small molecule chain transfer agent (CTA) as a simple model system to investigate the effect of M–L interactions on viscoelastic properties of polymer solution and melt (Scheme 3.1b). The brush copolymer B-ICP was synthesized by growing well-defined BA/IMZa copolymer brushes from a PS backbone macro-CTA having 10 mol % ($N_{CTA}/(N_{CTA} + N_{styrene}) \times 100$) pendant chain transfer agents. As we have shown previously,[45] in the solid state, this brush copolymer microphase separates to form PS nanodomains dispersed in a soft matrix. The microphase separated PS nanodomains act as physical cross-linkers and are crucial for the improved mechanical properties of these samples in bulk. All uniaxial tensile and self-healing tests of bulk samples were performed using the B-ICP. Details of the synthesis and characterization of all polymers using ^{1}H NMR and size exclusion chromatography (SEC) are included in the Experimental section. Important molecular composition data for L-ICP and B-ICP are summarized in Table 3.1.

Scheme 3.1 Synthesis of imidazole-containing monomer and copolymers

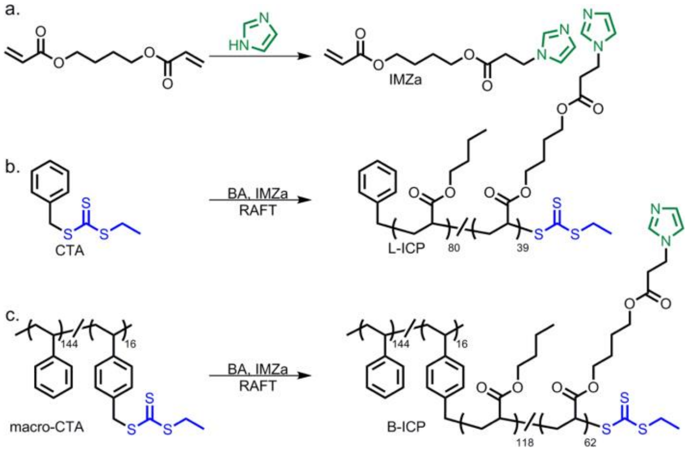

(a) Synthesis of imidazole-containing acrylate monomer, IMZa. (b) Synthesis of linear imidazole-containing polymer (L-ICP) from the small molecule CTA via RAFT polymerization. (c) Synthesis of a brush ICP (B-ICP) from polystyrene macro-CTA via RAFT polymerization.

Table 3.1 Molecular compositions of L-ICP and B-ICP samples

sample	backbone # of repeat units[a]	CTA sites[b]	Brush # of repeat units[b]	IMZa mol%[b,c]
L-ICP	-	1	119	33
B-ICP	160	16	180	34

[a]Calculated from size exclusion chromatography (SEC) using polystyrene standards in THF. [b]Estimated from ^{1}H NMR. [c]In mol %, calculated from $N_{IMZa}/(N_{IMZa} + N_{BA}) \times 100$, where N is the number of repeat units for each monomer.

3.2.2 Metal incorporation

For the following M–L study, different metal salts were added to the above-mentioned polymers to form dynamic networks. For all studies, the bis(trifluoromethylsulfonyl)imide (NTf_2^-) counterion was chosen due to its high mobility in the solid state. Clustering of NTf_2^- is disfavored because of its delocalized charge and unique shape. Additionally, NTf_2^- possesses good solubility and thermal stability. All metals used in this study contain NTf_2^- counterions for consistency. The composition of samples is described throughout this study using the following nomenclature: polymer–metal–L/M ratio. For example, L-ICP–Zn–4.0 refers to the linear imidazole-containing polymer that is cross-linked with $Zn(NTf_2)_2$ at the ratio of 4 imidazole ligands to 1 zinc ion.

3.2.3 Rheological studies of L-ICP–M samples

The L-ICP was used as a simple model system to explore the relationship between labile M–L complexes and mechanical properties. We started our investigation by looking at the rheological properties of L-ICP solutions cross-linked with different metal ions. Given that the M–L interactions play critical roles in the mechanical properties of the dynamic M–L networks, their contributions should manifest in both solution and the solid state.

In the absence of metal salt, solutions of L-ICP in acetonitrile ([L-ICP] = 350 mg/mL) did not exhibit any appreciable viscoelastic properties as expected from their relatively low degree of polymerization (DP = 119) and lack of strong interchain association. Upon slow addition of the metal salt (also dissolved in acetonitrile), an increase in the viscosity of the solution was noted. Two observations suggest that dynamic M-L cross-links are the major contributors to the viscoelastic properties of the solution: First, the dynamic viscosity of the solutions increased by the addition of more metal salt (i.e., decreasing the L/M ratio) (Figure 3.2a). Second, addition of a small molecule ligand, N-methylimidazole, to the dynamically cross-linked polymer solution resulted in a decrease in the viscosity, presumably by competing with the imidazole ligand on the polymer chain for binding to the metal ion (Figure S3.1).

Despite the observed increase in the viscosity of L-ICP solutions upon the addition of various metal salts, none of the mixtures formed stable gels, even at high metal content. Instead, the L-ICP−M (M = Zn^{2+}, Cu^{2+}, and Co^{2+}) solutions behaved as fluids ($G' < G''$ and constant dynamic viscosity across decades of shear rates, Figure S3.2). This observation demonstrates that the majority of M−L cross-links dynamically dissociate at the time scale of the rheological deformation.

Dynamic viscosity, as defined by $\eta = G''/\omega$ (where G'' is the rheological loss modulus and ω is the frequency of oscillation), is a measure of polymer network resistance to the shear flow, and it is expected to increase as more cross-links are added to the polymer solution. As shown in Figure 3.2a, the dependence of the dynamic viscosity on metal ion loading (i.e., L/M ratio) was strikingly different for these metals and did not always scale with the theoretical cross-linking density. Viscosity of L-ICP−Co samples increased gradually by the addition of more cobalt over the range of 15 > L/Co > 7.[47] In this range, the dynamic viscosity exhibited a power dependence on the cross-linking density ($\eta \approx (M/L)^6$). This dependence is higher than theoretical predictions,[48,49] but similar differences were previously observed in metallosupramolecular networks.[50]

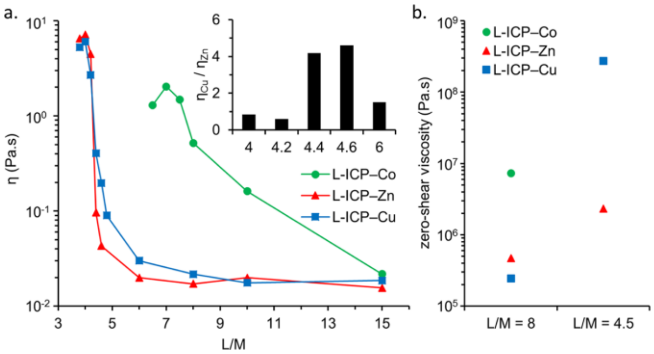

Figure 3.2 Rheological studies of L-ICP−M samples. (a) Dynamic viscosity of L-ICP−M CH_3CN solutions cross-linked with different amounts of metal. The inset shows the ratio of the dynamic viscosity of copper (η_{Cu}) to the dynamic viscosity of zinc (η_{Zn}) for select L/M ratios. (b) Zero-shear viscosity of L-ICP−M melt samples at 20 °C. At L/M = 8.0, the zero-shear viscosities of L-ICP samples cross-linked with Cu^{2+} and Zn^{2+} are similar, while the viscosity of L-ICP−Co−8.0 is over an order of magnitude larger. As the L/M ratio decreases from 8.0 to 4.5, the difference between the viscosity of L-ICP−Cu and L-ICP−Zn increases significantly. At L/M = 4.5, L-ICP−Cu is 100-fold more viscous than L-ICP−Zn.

In contrast, L-ICP solutions dynamically cross-linked with Cu^{2+} and Zn^{2+} displayed a dramatically different relationship between viscosity and the L/M ratio. For both Zn^{2+} and Cu^{2+} systems, the solution viscosity did not change significantly by the addition of more metal salts at low metal ion loading (6 < L/M < 15) but increased sharply near L/M ~ 4.0 (360-fold increase for zinc and 200-fold increase for copper). In other words, for these two metals, the solution viscosity surprisingly did not show any dependence on the cross-linking density of L-ICP−M over a large range of metal concentrations and increased significantly as the L/M approached 4.0.

To investigate these trends in neat polymer without any solvent, we next dried the cross-linked solutions of L-ICP−M and investigated the viscoelastic response of polymer melts under shear stress. In the absence of a polystyrene backbone, the L-ICP−M samples formed relatively weak materials. The physical state varied based on the identity of each metal and the L/M ratio, ranging from viscous liquids (L/M = 8, M= Zn^{2+} and Cu^{2+}) to soft solids (L/Co = 8; L/M = 4.5, M= Zn^{2+} and Cu^{2+}, which were still amenable to melt rheology). Consistent with solution rheology, L-ICP−Co−8.0 exhibited much higher zero-shear viscosity (~10^7 Pa·s) than L-ICP−Zn−8.0 or L-ICP−Cu−8.0 (~$10^{5.5}$ Pa·s). (Figure 3.2b and Figure S3.3). Similar to the solution rheology, the zero-shear viscosity of L-ICP−Cu and L-ICP−Zn melts increased dramatically near L/M ~4. Additionally, we noted that the subtle difference between the solution viscosities of L-ICP−Cu and L-ICP−Zn is magnified in the melt state. For example, at L/M = 4.5, L-ICP−Cu is 100-fold more viscous than L-ICP−Zn (Figure 3.2b) while in solution L-ICP−Cu is only 5-fold more viscous than L-ICP−Zn (Figure 3.2a, inset).

In summary, we observed the following trends in the rheological studies: First, the viscosities of zinc and copper samples peak with a sharp transition near L/M = 4, while the viscosity of cobalt samples increases more gradually and peaks near L/M = 6. Second, for zinc and copper samples the viscosity is not directly related to the density of cross-linker. In fact, doubling the density of cross-linkers (by changing L/M = 15 to L/M = 8.0) had no discernible effect on the overall viscosity. Finally, at intermediate L/M ratios (~4.5) copper samples display significantly higher viscosity than zinc samples, and this behavior was more pronounced when the solvent was removed.

3.2.4 Contribution of coordination number and ligand exchange mechanism to network mechanical properties

It is possible to rationalize the rheological response of L-ICP−M at different L/M ratios by considering the contribution of M−L cross-linkers (as the defining mechanical element) to the network structural topology and temporal relaxation. For example, the average junction functionality (number of polymer chains connected at one cross-linker) is directly influenced by the identity of the metal and its preferred coordination geometry. Nonetheless, it is clear from the viscosity trends that the dependence of viscoelastic properties on the added metal is fundamentally different for L-ICP−Co compared to L-ICP−Zn and L-ICP−Cu. While the L/M ratios at peak viscosity are consistent with the preferred coordination number of the complexes (Co^{2+}: $Co(Imz)_6^{2+}$; Zn^{2+}: $Zn(Imz)_4^{2+}$; Cu^{2+}: $Cu(Imz)_{4-6}^{2+}$), the coordination valency alone cannot explain the dramatic contrast in the observed trends, particularly the contrast between a gradual increase in the viscosity for solutions of L-ICP−Co and the sharp transition for L-ICP−Cu and L-ICP−Zn solutions. It is well-established that the bulk mechanical properties of networks held together by dynamic cross-linker are influenced strongly by the kinetics of cross-linker remodeling and exchange under load.[33,51,52] To fully account for the dramatic differences between different metal ions, it is necessary to consider the ligand exchange-induced relaxation in addition to the equilibrium network topology.

Ligand substitution in transition metal complexes is influenced by their electronic configuration and coordination number of the metal centers. The ligand exchange in four-coordinate tetrahedral complexes, such as $Zn(Imz)_4^{2+}$ and $Cu(Imz)_4^{2+}$, proceeds mainly through an associative mechanism for which the rate of exchange increases as the concentration of free ligand increases.[43,53–55] For both L-ICP−Cu and L-ICP−Zn, at high L/M ratio (i.e., low metal ion content) the cross-linked junctions can rapidly exchange due to the relatively high concentration of uncoordinated imidazole moieties on the polymer chains. Accordingly, an uncoordinated imidazole moiety is not merely a dangling chain with no contribution to the mechanical properties. The concentration of unbound ligands directly influences the rate of cross-link remodeling under load, which significantly impacts the mechanical properties.

As the L/M ratio approaches 4, most imidazole moieties are bound to metal centers; hence, the addition of a small amount of metal salt will precipitously reduce the concentration of uncoordinated imidazole moieties over a very narrow L/M window. At L/M ∼ 4.0, the absence of uncoordinated imidazole moieties further slows down the ligand exchange reaction, impeding the network remodeling and dramatically increasing the network dynamic viscosity. Both the concentration of uncoordinated imidazole moieties and the rate for an associative ligand exchange reaction are significantly reduced near L/M ∼ 4. As shown in Figure S3.6 of the Experimental section, it is possible to qualitatively predict the sharp increase in the viscosity near L/M ∼ 4 for Cu^{2+} and Zn^{2+} systems by assuming that the dynamic viscosity is inversely proportional to the rate of the ligand exchange reaction.[33,51] Thus, for L-ICP−Zn and L-ICP−Cu, as more metal is added to these systems, not only does the polymer network become more cross-linked but also the rate of cross-link remodeling under shear stress is further reduced and the network exhibits collectively higher resistance to flow beyond the predictions of a static view of cross-linking density.

On the contrary, the ligand exchange in octahedral complexes, such as $Co(Imz)_6^{2+}$, occurs with significant dissociative character because steric hindrance disfavors the formation of complexes with higher coordination numbers.[42,56–58] The kinetic manifestation of the dissociative ligand exchange mechanism is the independence of the exchange rate and the unbound ligand concentration, as the rate-determining step is ligand dissociation. These observations suggest that the rate of exchange for $Co(Imz)_6^{2+}$ cross-linkers should not be significantly affected by the presence of dangling side chains. Accordingly, the gradual increase in the dynamic viscosity of L-ICP−Co with the addition of more Co^{2+} salt is consistent with the formation of transient networks with increasing cross-linking density (Figure 3.2a).[59]

To summarize, an unbound imidazole (dangling chain) in this system can influence the network relaxation and bulk properties depending on the M−L preferred mechanism of the ligand exchange. For exchange with associative−dissociative character, we predict and observe a sharp, dramatic switch in properties when the cross-link exchange is arrested as the concentration of unbound ligand reaches zero.

3.2.5 Fine-tuning the mechanical properties through a network of weak associations

The difference in ligand coordination number between zinc and copper complexes is a plausible explanation for the observed difference in viscosity between copper and zinc samples in the range of $4 < L/M < 6$. Zn^{2+} strongly prefers four-coordinate tetrahedral complexes (especially with bulkier imidazole derivatives) while Cu^{2+} can adopt a coordination number from 4 to 6 depending on the availability and sterics of the imidazole ligands. Not only have complexes of $Cu(Imz)_5^{2+}$ and $Cu(Imz)_6^{2+}$ been isolated and characterized previously, but also reliable data for equilibrium constants ($K_5 = 4.0$, $K_6 = 1.3$) are reported in the literature.[60] In contrast, isolated $Zn(Imz)_6^{2+}$ complexes prove unstable and show a strong preference to lose two ligands upon mild heating.[61]

Using the available binding constant data,60 we calculated the theoretical distribution of different species in a system of zinc and copper complexes (Figure S3.5). As expected, the calculation shows that for $4 < L/M < 6$ a considerable amount of CuL_4^{2+}, CuL_5^{2+}, and CuL_6^{2+} coexist in equilibrium. The presence of these higher coordination number complexes (CuL_5^{2+} and CuL_6^{2+}) could impact both the topological and temporal properties of the network. According to the phantom network model, the number of elastically active chains increases as the functionality of the cross-linker is increased.[62] Additionally, the presence of CuL_5^{2+} and CuL_6^{2+} results in a lower concentration of uncoordinated imidazole moieties at any given L/M ratio compared to the ZnL_4^{2+} system. As discussed above, the reduced concentration of uncoordinated imidazole moieties may also reduce the dynamics of ligand exchange-induced cross-linker remodeling for Cu^{2+} due to its preference for the associative ligand exchange mechanism.

Overall, it is clear that these additional equilibria for L-ICP−Cu, despite their low association constants, significantly change the dynamic properties of L-ICP−Cu compared to L-ICP−Zn in the solution and the melt state (similar effects are observed in static tensile tests, *vide infra*). Our results demonstrate the potential of using "very weak" dynamic M−L interactions to engineer mechanical properties by controlling the population of mechanically active cross-linking elements and the dynamic ligand exchange rate. This molecular strategy is often neglected in material science as most mechanically active cross-linking elements are chosen from motifs with high association and slow exchange rates.[13,32–35] Nonetheless, it is possible to achieve unprecedented control over both the structure of networks (by controlling the number and the coordination geometry of M−L cross-linker) and the temporal response (ligand exchange-induced relaxation kinetics) of bulk materials using dynamic association of weak and monodentate ligands with transition metals.

3.2.6 Modulating uniaxial tensile properties of B-ICP−M

The rheological studies of the model systems supported our hypothesis that the concentration of unbound ligands can modulate the rate of cross-linker remodeling under dynamic load. We envisioned that a similar mechanism can also be utilized to engineer a desired mechanical response to tensile stress. To test this hypothesis, we next investigated the mechanical properties of ICP−M in bulk using static tensile tests. As it is evident from melt rheology data, cross-linking of these low molecular weight linear polymer chains with transient imidazole−metal interactions is generally not sufficient to produce mechanically strong materials. A common strategy used in both natural[63,64] and synthetic materials[45,64] is to combine the dissipative properties of relatively weak, dynamic interactions with rigid structural domains, often in a multiphase fashion, to obtain advanced properties. One of the most recognized biological examples of this design strategy is spider silk, where crystalline domains with high β-sheet content are used in tandem with disordered protein sequences.[65] Spider silk's exceptional mechanical properties are attributed to this hierarchical structure.[66] Additionally, in mussel byssus threads, histidine-rich domains flank a rigid collagenous network to combine mechanical strength and molecular self-healing.[67] In our design, such structural hierarchy is mimicked by a multiphasic design, where glassy polystyrene nanodomains act as physical cross-links and contribute to the mechanical properties, such as the Young's modulus and the post yield behavior.

B-ICP−M samples were prepared by a method similar to L-ICP−M. After the removal of solvents, the samples were melt pressed in a vacuum oven (T = 100 °C) and allowed to cool to room temperature (approximately 30 min). The mechanical properties of each sample were evaluated by static tensile tests. Representative tensile stress−strain curves, along with select mechanical properties, for each system at different L/M ratios are shown in Figure 3.3. The complete summary of tensile mechanical properties is presented in Table S3.3.

A quick survey of representative stress−strain curves in Figure 3.3 demonstrates that the thermodynamic and kinetic parameters of M−L cross-linkers influence different aspects of mechanical response under load. We have selected two parameters, the Young's modulus (E) and the ultimate extensibility ($\varepsilon_{\mathrm{ult}}$), to highlight these differences. The Young's modulus is the measure of a material's stiffness, describing the response of a material under load in the low strain regime where the polymer chains are not significantly stretched and the response to the applied force stems from the number and the functionality of cross-linking points (structural topology). We observe that across all three metals the Young's modulus is proportional to the number and the functionality of cross-linkers (coordination number and geometry). On the other hand, ultimate extensibility (strain-at-break) of different ICP−M exhibits a more complex trend and does not decrease uniformly with increasing cross-linking density as is typically expected. Here, we find that the trends of strain-at-break versus the L/M ratio for all metals resembles the trends of viscosity (gradual decrease for cobalt versus sudden decrease for zinc, Figure 3.2), suggesting a connection to the ligand exchange induced relaxation kinetics of M−L cross-linkers (temporal response). This connection is plausible as the dynamics of crosslinker remodeling alters the redistribution of stress across the extended chains to increase strain-at-break. Additionally, the transient cross-linkers can rupture at the time scale of deformation, absorbing energy and protecting the covalent network from catastrophic failure.[68–71]

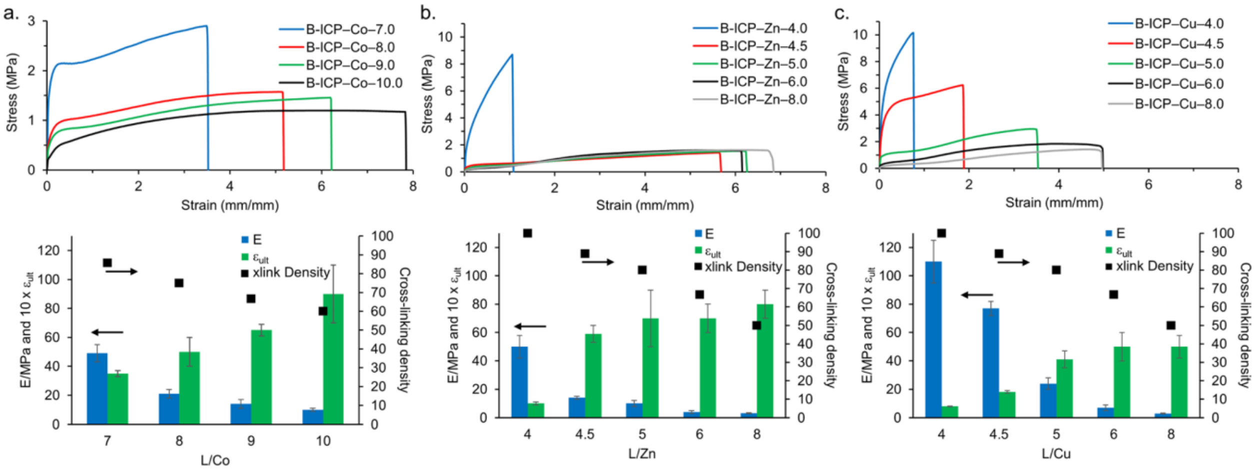

Figure 3.3 Static tensile stress−strain curves for B-ICP−M samples. Different L/M ratios are tested, where M = Co^{2+} (a), Zn^{2+} (b), and Cu^{2+} (c) (top, strain rate: 100 mm/min, 25 °C). Select mechanical properties derived from stress−strain curves, Young's modulus (left, *E*) and strain-at-break (left, ε_{ult}), plotted with theoretical cross-linking density (right) at each L/M ratio (bottom). Theoretical degree of cross-linking at any L/M ratio is defined as the (1 − [unbound imidazole]/$[\text{imidazole}]_0$) × 100 by assuming the preferred coordination number of 6 for Co and 4 for Zn and Cu. A summary of mechanical properties is provided in Table S3.3.

For all three metals, the Young's modulus increases with increasing cross-link density, defined as (1 − [unbound imidazole]/$[\text{imidazole}]_0$) × 100, through the addition of more metal ions (i.e., with the decrease of the L/M ratio) or using metal centers with higher preferred coordination number. For example, for B-ICP−Co samples with L/Co decreasing from 10.0 to 7.0, the Young's modulus increases monotonically (Figure 3.3a and Table S3.3). This trend is consistent with the gradual increase in the M−L cross-linking density with the addition of more metal salts, which is corroborated by the trend in dynamic viscosity observed in the L-ICP−Co solution rheology (Figure 3.2). Additionally, the Co^{2+} samples have a higher Young's modulus than Zn^{2+} and Cu^{2+} samples at the same L/M ratio. For example, B-ICP−Co−8.0 has a Young's modulus of 21 ± 3 MPa, which is 7-fold higher than the Young's modulus of Cu^{2+} and Zn^{2+} samples at the same L/M ratio. We attribute this difference in Young's modulus to the preference of Co^{2+} to form octahedral complexes, whereas Zn^{2+} and Cu^{2+} prefer complexes with lower coordination number. ML_6 complexes have higher functionalities, and therefore more polymer chains are cross-linked per ML_6 metal junction compared to ML_4-type cross-links. Comparison of B-ICP−Cu and B-ICP−Zn provides additional evidence to support this hypothesis as the copper samples, which form $Cu(Imz)_{4-6}^{2+}$ complexes, consistently exhibit a higher Young's modulus than zinc. The maximal difference between these two metals is still around L/M ~ 4.5, at which the Young's modulus of B-ICP−Cu−4.5 is 77 ± 5 MPa while the value of B-ICP−Zn−4.5 is 14 ± 1 MPa (Figure 3.3).

Unlike the Young's modulus, the extensibility trends do not directly correlate with the cross-linking density for all metals. For our L-ICP−M systems, our solution and melt rheology data showed that the small molecule kinetics of ligand exchange directly influence the rheological properties in solution and melt (Figure 3.2). It is reasonable to assume that ligand exchange kinetics should also modulate the bulk network behavior under static load for our B-ICP−M systems.

Consistent with our solution and melt rheology data, the dependence of bulk tensile mechanical properties on the L/M ratio for the B-ICP−Zn (Figure 3.3b) and B-ICP−Cu (Figure 3.3c) samples deviated significantly from the B-ICP−Co samples. The ultimate tensile strength and extensibility of B-ICP−Zn did not change significantly when the L/Zn ratio was lowered from 8 to 4.5. In contrast, reducing the L/Co ratio from 10 to 7, corresponding to a comparable increase in cross-linking density, increased the ultimate tensile strength by 50% and reduced the ultimate extensibility by more than 80%. Notably, the tensile properties of bulk B-ICP−Zn samples at various metal ion loadings (Figure 3.3b) follow a similar trend versus the L/M ratio as the dynamic rheological properties of the L-ICP−Zn solutions (Figure 3.2). A sharp transition in the bulk mechanical properties was observed at L/Zn ~ 4.0 for B-ICP−Zn, where the sample transitioned from a very extensible rubber into a relatively stiff plastic. Specifically, reducing the L/Zn from 4.5 to 4.0 resulted in an increase of the tensile strength by 540% and a decrease of the extensibility by 600%. The striking similarities in the dependence of mechanical properties on the L/Zn ratio suggest that the observed sharp transitions in mechanical behaviors for both solution and bulk polymer samples originate from the same molecular mechanism.

The differences in bulk mechanical properties between Zn^{2+} and Co^{2+} samples can be explained by their respective exchange mechanisms. Given the associative ligand exchange mechanism for the Zn−imidazole complex, as the L/Zn ratio approaches 4.0, a drastic reduction of uncoordinated imidazole moieties in the bulk sample would dramatically slow down the ligand exchange reaction, impeding network relaxation and dramatically increasing the network rigidity. For Co^{2+}, as the metal salt loading was increased, the extensibility gradually decreased and the tensile strength increased. The dissociative nature of its ligand exchange and the relatively slow exchange dynamics of Co^{2+}−imidazole complexes, further slowed in bulk samples and in the absence of solvent, make the Co^{2+}−imidazole cross-links similar to covalent cross-links for which the increase in cross-linking density generally results in lower extensibility and higher tensile strength.23

B-ICP−Cu displays a similar overall trend to B-ICP−Zn in the high and low regimes of the tested L/Cu ratios (Figure 3.3c). At high L/Cu ratios (6.0 < L/Cu < 8.0), the mechanical properties are not affected significantly by the amount of added metal. On the other hand, a sharp transition in the mechanical properties is observed near B-ICP−Cu−4.0. For the intermediate regime, with $4.5 < L/Cu < 6$, the tensile mechanical properties changed gradually. This is different from the behavior of the B-ICP−Zn sample where the transition from “soft elastomer” to “hard plastic” occurs abruptly around $L/Zn \sim 4$. This difference in bulk mechanical properties between B-ICP−Zn and B-ICP−Cu closely mirrors the trend of rheological properties in solution (Figure 3.2a). We note here that the observed differences in mechanical properties between copper and zinc samples in this region are more pronounced in dry states (i.e., polymer melt and bulk tensile samples) compared to solution state due to the absence of solvent-assisted exchange (CH_3CN is a coordinating solvent due to its π-accepting characteristics).[72] As discussed earlier, we attribute the differences between copper and zinc samples to the flexibility of the coordination number in Cu^{2+} complexes. Comparison of the mechanical properties of B-ICPs cross-linked with Cu^{2+} or Zn^{2+} further highlights the importance of weak interactions (with low association constant) on the population and dynamics of transient cross-linkers.

To demonstrate that these observed effects are not simply physical effects from the addition of the metal salt, we prepared B-ICP−Ca samples by adding $Ca(NTf_2)_2$ salt into the B-ICP polymer. Calcium(II) is a divalent ion in the same row of the periodic table as the transition metals used in this study while having lower binding affinity to the imidazole.[73] We prepared B-ICP−Ca samples with L/Ca of 4 by addition of $Ca(NTf_2)_2$ to the solution of B-ICP. In both cases, the viscosity of the solution did not change significantly, and after the removal of solvents, the resulting materials were significantly weaker than B-ICP−Cu and B-ICP−Zn with L/M = 4 (Figure S3.4).

The dependence of the bulk tensile properties on the M−L content is summarized in Figure 3.4. At low strain regimes, the mechanical response under load is dominated by the structural topology of the network, number (metal content), and functionality (M−L complex coordination number) of the cross-linker. As the polymer chains are stretched further, the dynamics of ligand exchange influence the outcome of overstretched chains as the rupture of the cross-linkers results in the relaxation of chains under the stress.

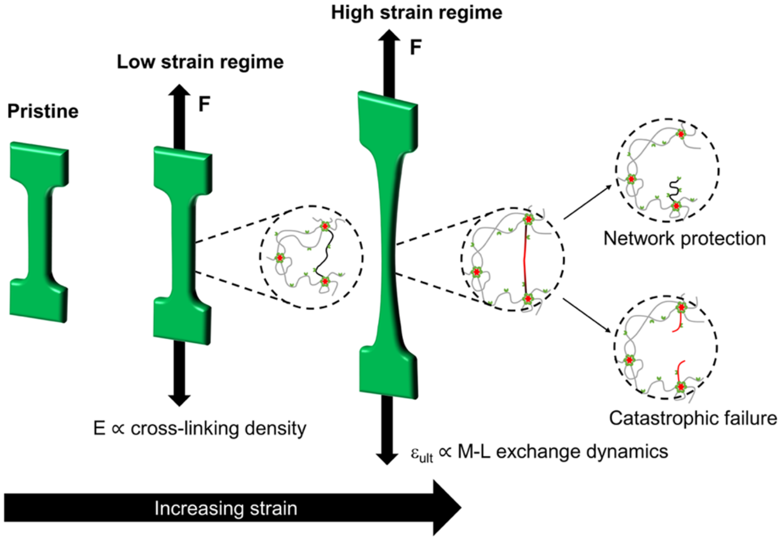

Figure 3.4 Proposed relationship between mechanical properties and L/M ratio. At low strain, quantity and topology of the M−L complexes dictate cross-link density and therefore the Young's modulus. At high strain, cross-link remodeling influences the fate of overstretched polymer chains. The ultimate extensibility (strain-at-break) of networks is governed by M−L exchange dynamics.

These results clearly demonstrate that a wide window of mechanical properties is accessible by simply tuning the metal salt identity and loading. By adjusting one parameter, the L/M ratio, we have achieved concurrent control over structural organization and temporal response of defining mechanical elements by using dynamic association of weak and monodentate ligands with transition metals. The imidazole ligands in our system provide a unique opportunity to exploit these design principles and fine-tune the mechanical properties under dynamic and static loading. The weak monodentate binding of the imidazole ligand is in direct contrast with many of the previously reported multidentate ligands (i.e., bidentate histidine[74] and tridentate terpyridine).

3.2.7 Self-healing studies of B-ICP−M

Finally, we investigated the self-healing behavior of selected B-ICP−M. Efficient self-healing in supramolecular systems requires adhesion of the cut interface, diffusion of polymer chains across the damaged interfaces, and reassociation of dynamic motifs.[75,76] Since the B-ICP−M samples were prepared from identical polymer architecture (B-ICP), any observed differences in self-healing efficiency must be caused by differences in dynamic M−L cross-links[77–79] such as the geometry, ligand exchange mechanism, and kinetics of the M−L complexes. These parameters should influence both the exchange rates of the dynamic motifs and the localized polymer diffusion near the cut interface.

B-ICP−M samples for self-healing were so chosen to ensure that a fraction of uncoordinated ligands was present to facilitate ligand exchange. As such, B-ICP−Zn−4.5, B-ICP−Cu−4.5, and B-ICP−Co−7.0 were chosen. To minimize the residual stress from compression molding, samples used in self-healing studies were thermally annealed by slowly cooling the samples from 100 °C to room temperature over 12 h. Next, a well-defined cut was made through the center (75% of width) of the sample, and the cut interfaces were brought back together for 1 min and then left to heal under ambient conditions without further treatment.

The selected B-ICP−M samples showed various healing efficiencies under ambient conditions. Consistent with our previous reports, B-ICP−Zn−4.5 displayed excellent healing efficiency, showing quantitative recovery of the Young's modulus and toughness after only 3 h under ambient conditions (Figure 3.5a). However, B-ICP−Cu−4.5 showed only minimal healing after 3 h and healed to about 50% toughness after 24 h under ambient conditions (Figure 3.5b). Finally, B-ICP−Co−7.0 exhibited the lowest healing efficiency and recovered only about 20% of the pristine sample's toughness.

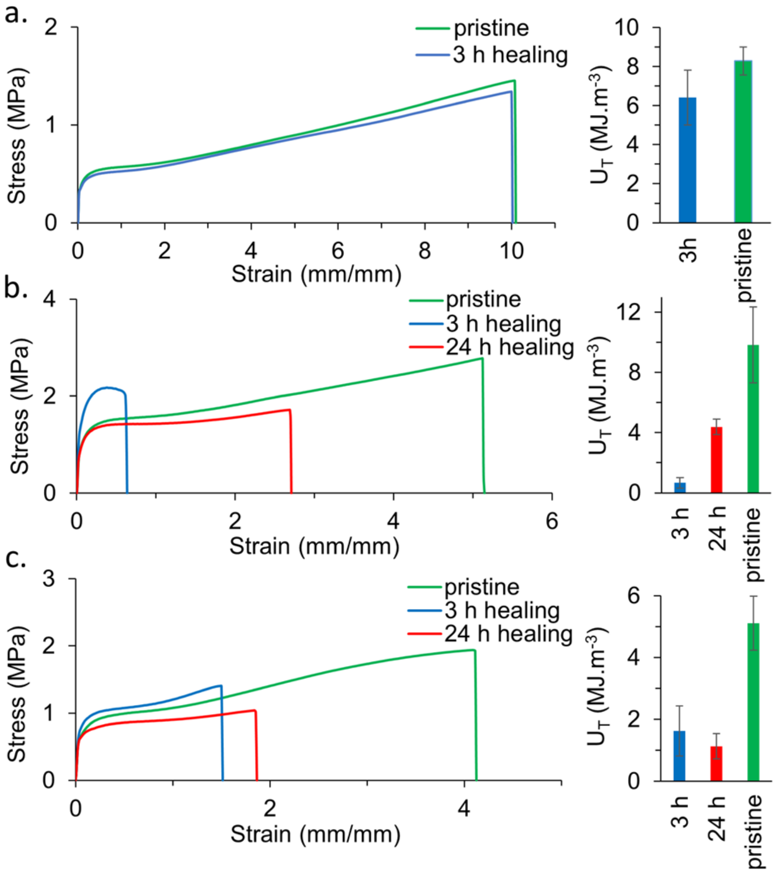

Figure 3.5 Self-healing test for B-ICP−M samples under ambient conditions. (a) Stress−strain curves for B-ICP−Zn−4.5 healed for 3 h and pristine sample. (b) Stress−strain curves for B-ICP−Cu−4.5 healed for 3 and 24 h. (c) Stress−strain curves for B-ICP−Co−7.0 healed for 3 and 24 h (strain rate: 100 mm/min, 25 °C). The bar graph summarizes the toughness recovery for each sample. Error bars are standard deviation for at least three measurements.

The decreased healing efficiency of B-ICP−Cu−4.5 is consistent with the slower network relaxation observed by the polymer melt rheology (Figure S3.3). As described earlier, formation of CuL_5^{2+} and CuL_6^{2+} complexes is presumably responsible for the extended relaxation times as the cross-link exchange and polymer diffusion were hindered. Following a similar reasoning, it is not surprising that B-ICP−Co−7.0 exhibited the lowest healing efficiency, as the Co^{2+}−imidazole complex has the highest coordination number and slowest exchange rate (Figure 3.3).

We note that based on the mechanistic lessons of this study, it is possible to improve the self-healing efficiency of B-ICP−M by introducing a small amount of unbound ligand at the damaged surface to facilitate cross-linking exchange and polymer diffusion across the cut interface. This extrinsic self-healing ability is currently being investigated in our laboratory, and the results will be reported in due course.

3.3 Conclusion

M−L interactions are receiving increased attention as a promising dynamic motif to control material response under load.[80–82] In this work, we used our previously developed ICP system to demonstrate that it is possible to simultaneously control both the structural topology and the temporal response of bulk material using dynamic association of weak and monodentate ligands with transition metals. Our well-defined linear and brush copolymers allow us to systematically control multiple structural and compositional parameters for each sample, such as the density of imidazole ligand on polymer brushes, the type of metal salt, and the L/M ratio. By combining this compositionally well-defined system with a series of "weak" and labile metal−imidazole interactions, our study demonstrates design rules that complement current approaches to incorporate metal–ligand complexes as defining mechanical elements.

We demonstrated that the bulk mechanical response of these materials under both static and dynamic loads are influenced significantly by the L/M stoichiometry and coordination number of the metal complex. In particular, we observed intriguing differences between the evolution of mechanical response for each metal regardless of the physical state (i.e., linear polymer solution and melt, multiphasic elastomer). Samples cross-linked with Zn^{2+} and Cu^{2+} did not behave as traditionally cross-linked materials, exhibiting mechanical properties that did not always correlate to the amount of added metal. Specifically, the addition of more Zn^{2+} or Cu^{2+} salt had no effect on viscosity or extensibility, until a sharp transition occurred near a critical ligand to metal ratio (L/M = 4). In contrast, addition of more Co^{2+} salt resulted in a proportional, and incremental increase in viscosity of polymer solutions and melts as well as a decrease in extensibility. These trends for Co^{2+} containing polymers more closely resemble incorporation of permanent cross-linker, while offering significant energy dissipation through force mediated rupture of weaker coordination bonds, evident by the high extensibility of B-ICP–Co samples.

We suggest that the mechanism of ligand exchange could explain the observed differences in mechanical behavior of these metallopolymers. Specifically, the concentration of unbound imidazole should affect the remodeling rate of cross-linked junctions differently for a mechanism with associative character (ML_4^{2+} complexes, M = Zn and Cu) compared to dissociative character (CoL_6^{2+}). The uncoordinated imidazole effectively catalyzes the exchange of the polymer chains bound through the ML_4^{2+} species. When L/M approaches 4 for Zn^{2+} and Cu^{2+}, the concentration of free imidazole is reduced significantly by the addition of small amount of metal and thus drastically reducing the cross-linking remodeling kinetics under load. The sudden transition of these materials from extensible elastomers to stiff plastics is noteworthy and is reminiscent of the mechanical properties of biological tissues such as the proteinaceous jaws of Nereis and Glycera worms, among the hardest nonmineralized biological tissues identified to date.[83,84] This structural protein is enriched in histidine, similar to the metal-binding domains of mussel byssus.[85] Nonetheless, unlike extensible byssal threads, metal-mediated cross-linking of these proteins results in a lightweight composite with high stiffness, hardness, and abrasion resistance.[86,87]

The contribution of weak and dynamic interactions is underscored when samples cross-linked with Zn^{2+} and Cu^{2+} are further compared. Despite similarities in trend, it was not straightforward to fine-tune the static tensile properties of the B-ICP−Zn samples between the thermoplastic elastomer and stiff plastic as the addition of small amount of zinc salt (<1% w/w) near the L/Zn of 4.0 significantly changed the mechanical properties (data not shown). On the other hand, samples with intermediate behavior under static load were easily accessible in B-ICP−Cu. We attributed this difference to the ability of copper to form complexes with more than four imidazole even though the K_5 and K_6 were significantly smaller than K_{1-4}. The network of these cross-linkers with different topology and dynamics results in a superior mechanical adaptability.

We anticipate that this study will further efforts toward engineering “weak” and transient associations in dynamic materials, while testifying to the utility of M−L interactions as a promising motif for material design for concurrent control of structural and temporal hierarchy. Finally, we suggest that other mechanical properties of metallopolymers, such as adhesion, hardness, and abrasion resistance, may show similar dependence on the kinetic parameters and L/M ratios of contributing M−L complexes. Future studies can unravel these trends and provide similar guidelines for minimalistic design of bioinspired materials.

3.4 References

(1) Boesel, L. F.; Greiner, C.; Arzt, E.; del Campo, A. *Adv. Mater.* **2010**, *22* (19), 2125–2137.

(2) Banerjee, I.; Pangule, R. C.; Kane, R. S. *Adv. Mater.* **2011**, *23* (6), 690–718.

(3) Wijewardane, S.; Goswami, D. Y. *Renew. Sustain. Energy Rev.* **2012**, *16* (4), 1863–1873.

(4) Chaudhuri, O.; Gu, L.; Klumpers, D.; Darnell, M.; Bencherif, S. A.; Weaver, J. C.; Huebsch, N.; Lee, H.; Lippens, E.; Duda, G. N.; Mooney, D. J. *Nat. Mater.* **2016**, *15* (3), 326–334.

(5) Sijbesma, R. P.; Beijer, F. H.; Brunsveld, L.; Folmer, B. J. B.; Hirschberg, J. H. K. K.; Lange, R. F. M.; Lowe, J. K. L.; Meijer, E. W. *Science.* **1997**, *278* (5343), 1601–1604.

(6) Cordier, P.; Tournilhac, F.; Soulié-Ziakovic, C.; Leibler, L. *Nature* **2008**, *451* (7181), 977–980.

(7) Montarnal, D.; Tournilhac, F.; Hidalgo, M.; Couturier, J.-L.; Leibler, L. *J. Am. Chem. Soc.* **2009**, *131* (23), 7966–7967.

(8) Agnaou, R.; Capelot, M.; Tencé-Girault, S.; Tournilhac, F.; Leibler, L. *J. Am. Chem. Soc.* **2014**, *136* (32), 11268–11271.

(9) Sun, T. L.; Kurokawa, T.; Kuroda, S.; Ihsan, A. Bin; Akasaki, T.; Sato, K.; Haque, M. A.; Nakajima, T.; Gong, J. P. *Nat. Mater.* **2013**, *12* (10), 932–937.

(10) Henderson, K. J.; Zhou, T. C.; Otim, K. J.; Shull, K. R. *Macromolecules* **2010**, *43* (14), 6193–6201.

(11) Das, A.; Sallat, A.; Böhme, F.; Suckow, M.; Basu, D.; Wießner, S.; Stöckelhuber, K. W.; Voit, B.; Heinrich, G. *ACS Appl. Mater. Interfaces* **2015**, *7* (37), 20623–20630.

(12) Burattini, S.; Greenland, B. W.; Merino, D. H.; Weng, W.; Seppala, J.; Colquhoun, H. M.; Hayes, W.; MacKay, M. E.; Hamley, I. W.; Rowan, S. J. *J. Am. Chem. Soc.* **2010**, *132*, 12051–12058.

(13) Vermonden, T.; van Steenbergen, M. J.; Besseling, N. A. M.; Marcelis, A. T. M.; Hennink, W. E.; Sudhölter, E. J. R.; Cohen Stuart, M. A. *J. Am. Chem. Soc.* **2004**, *126* (48), 15802–15808.

(14) Zhao, Y.; Beck, J. B.; Rowan, S. J.; Jamieson, A. M. *Macromolecules* **2004**, *37* (10), 3529–3531.

(15) Li, C.-H.; Wang, C.; Keplinger, C.; Zuo, J.-L.; Jin, L.; Sun, Y.; Zheng, P.; Cao, Y.; Lissel, F.; Linder, C.; You, X.-Z.; Bao, Z. *Nat. Chem.* **2016**, *8* (6), 618–624.

(16) Razgoniaev, A. O.; Butaeva, E. V.; Iretskii, A. V.; Ostrowski, A. D. *Inorg. Chem.* **2016**, *55* (11), 5430–5437.

(17) Weng, W.; Beck, J. B.; Jamieson, A. M.; Rowan, S. J. *J. Am. Chem. Soc.* **2006**, *128* (35), 11663–11672.

(18) Williams, K. A.; Boydston, A. J.; Bielawski, C. W. *J. R. Soc. Interface* **2007**, *4* (13), 359–362.

(19) Chen, P.; Li, Q.; Grindy, S.; Holten-Andersen, N. *J. Am. Chem. Soc.* **2015**, *137* (36), 11590–11593.

(20) Enke, M.; Bode, S.; Vitz, J.; Schacher, F. H.; Harrington, M. J.; Hager, M. D.; Schubert, U. S. *Polymer.* **2015**, *69*, 274–282.

(21) Balkenende, D. W. R.; Coulibaly, S.; Balog, S.; Simon, Y. C.; Fiore, G. L.; Weder, C. *J. Am. Chem. Soc.* **2014**, *136* (29), 10493–10498.

(22) Bode, S.; Bose, R. K.; Matthes, S.; Ehrhardt, M.; Seifert, A.; Schacher, F. H.; Paulus, R. M.; Stumpf, S.; Sandmann, B.; Vitz, J.; Winter, A.; Hoeppener, S.; Garcia, S. J.; Spange, S.; van der Zwaag, S.; Hager, M. D.; Schubert, U. S. *Polym. Chem.* **2013**, *4* (18), 4966.

(23) Li, Q.; Barrett, D. G.; Messersmith, P. B.; Holten-Andersen, N. *ACS Nano* **2016**, *10* (1),

1317–1324.

(24) Rao, Y.-L.; Chortos, A.; Pfattner, R.; Lissel, F.; Chiu, Y.-C.; Feig, V.; Xu, J.; Kurosawa, T.; Gu, X.; Wang, C.; He, M.; Chung, J. W.; Bao, Z. *J. Am. Chem. Soc.* **2016**, *138* (18), 6020–6027.

(25) Zhao, X. *Soft Matter* **2014**, *10*, 672–687.

(26) Whittell, G. R.; Manners, I. *Adv. Mater.* **2007**, *19* (21), 3439–3468.

(27) Whittell, G. R.; Hager, M. D.; Schubert, U. S.; Manners, I. *Nat. Mater.* **2011**, *10* (3), 176–188.

(28) Degtyar, E.; Harrington, M. J.; Politi, Y.; Fratzl, P. *Angew. Chem. Int. Ed. Engl.* **2014**, *53* (45), 12026–12044.

(29) Kruck, T. *Angew. Chemie* **1967**, *79* (8), 387–387.

(30) Harris, R. D.; Auletta, J. T.; Motlagh, S. A. M.; Lawless, M. J.; Perri, N. M.; Saxena, S.; Weiland, L. M.; Waldeck, D. H.; Clark, W. W.; Meyer, T. Y. *ACS Macro Lett.* **2013**, *2* (12), 1095–1099.

(31) Wegner, S. V.; Schenk, F. C.; Witzel, S.; Bialas, F.; Spatz, J. P. *Macromolecules* **2016**, *49* (11), 4229–4235.

(32) Yount, W. C.; Juwarker, H.; Craig, S. L. *J. Am. Chem. Soc.* **2003**, *125* (50), 15302–15303.

(33) Yount, W. C.; Loveless, D. M.; Craig, S. L. *J. Am. Chem. Soc.* **2005**, *127* (41), 14488–14496.

(34) Burnworth, M.; Tang, L.; Kumpfer, J. R.; Duncan, A. J.; Beyer, F. L.; Fiore, G. L.; Rowan, S. J.; Weder, C. *Nature* **2011**, *472* (7343), 334–337.

(35) Bode, S.; Zedler, L.; Schacher, F. H.; Dietzek, B.; Schmitt, M.; Popp, J.; Hager, M. D.; Schubert, U. S. *Adv. Mater.* **2013**, *25* (11), 1634–1638.

(36) Chen, X. M.; Huang, X. C.; Xu, Z. T.; Huang, X. Y. *Acta Crystallogr. Sect. C Cryst. Struct.*

Commun. **1996**, *52* (10), 2482–2484.

(37) Roe, R. R.; Pang, Y.-P. *J. Mol. Model.* **1999**, *5* (7–8), 134–140.

(38) Marzotto, A.; Bianchi, A.; Valle, G.; Clemente, D. A. *Acta Crystallogr. Sect. C Cryst. Struct. Commun.* **1989**, *45* (4), 582–585.

(39) Reedijk, J. *J. Inorg. Nucl. Chem.* **1971**, *33* (1), 179–188.

(40) Vander Hoogerstraete, T.; Brooks, N. R.; Norberg, B.; Wouters, J.; Van Hecke, K.; Van Meervelt, L.; Binnemans, K. *CrystEngComm* **2012**, *14* (15), 4902.

(41) Otieno, T.; Hatfield, M. J.; Asher, S. L.; McMullin, A. I.; Patrick, B. O.; Parkin, S. *Synth. React. Inorg. Met. Chem.* **2001**, *31* (9), 1587–1598.

(42) Helm, L.; Merbach, A. E. *Chem. Rev.* **2005**, *105* (6), 1923–1960.

(43) Richens, D. T. *Chem. Rev.* **2005**, *105* (6), 1961–2002.

(44) Chung, J.; Kushner, A. M.; Weisman, A. C.; Guan, Z. *Nat. Mater.* **2014**, *13* (11), 1055–1062.

(45) Mozhdehi, D.; Ayala, S.; Cromwell, O. R.; Guan, Z. *J. Am. Chem. Soc.* **2014**, *136* (46), 16128–16131.

(46) Moad, G.; Rizzardo, E.; Thang, S. H. *Aust. J. Chem.* **2009**, *62* (11), 1402.

(47) *Our numerous attempts to prepare samples with L/Cu < 7 were unsuccesful as the polymer irreversibly precipitated from solution, forming a dense polymer coacervate and a less viscous solvent layer. The observed reduction of viscosity at L/Co = 6.5 (Figure 3.2) was attributed to the onset of this phase transition. To avoid complication caused by sample inhomogeneity, for Co system we limited our studies with Co incorporation to L/Co > 7.*

(48) Rubinstein, M.; Semenov, A. N. *Macromolecules* **1998**, *31* (4), 1386–1397.

(49) Rubinstein, M.; Semenov, A. N. *Macromolecules* **2001**, *34* (4), 1058–1068.

(50) Xu, D.; Craig, S. L. *Macromolecules* **2011**, *44* (13), 5465–5472.

(51) Yount, W. C.; Loveless, D. M.; Craig, S. L. *Angew. Chemie Int. Ed.* **2005**, *44* (18), 2746–2748.

(52) Loveless, D. M.; Jeon, S. L.; Craig, S. L. *Macromolecules* **2005**, *38* (24), 10171–10177.

(53) Shtyrlin, V. G.; Zyavkina, Y. I.; Gilyazetdinov, E. M.; Bukharov, M. S.; Krutikov, A. A.; Garipov, R. R.; Mukhtarov, A. S.; Zakharov, A. V. *Dalton Trans.* **2012**, *41* (4), 1216–1228.

(54) Alzoubi, B. M.; Puchta, R.; van Eldik, R. *Chem. - A Eur. J.* **2010**, *16* (24), 7300–7308.

(55) Mereshchenko, A. S.; Olshin, P. K.; Karabaeva, K. E.; Panov, M. S.; Wilson, R. M.; Kochemirovsky, V. A.; Skripkin, M. Y.; Tveryanovich, Y. S.; Tarnovsky, A. N. *J. Phys. Chem. B* **2015**, *119* (28), 8754–8763.

(56) Ducommun, Y.; Newman, K. E.; Merbach, A. E. *Inorg. Chem.* **1980**, *19* (12), 3696–3703.

(57) Wilkins, R. G. *Transit. Met. Chem.* **1998**, *23*, 735–737.

(58) Fratiello, A.; Schuster, R. E.; Bartolini, G. *J. Am. Chem. Soc.* **1970**, *92* (8), 2304–2308.

(59) Jackson, A. C.; Beyer, F. L.; Price, S. C.; Rinderspacher, B. C.; Lambeth, R. H. *Macromolecules* **2013**, *46* (14), 5416–5422.

(60) Sjöberg, S. *Pure Appl. Chem.* **1997**, *69* (7), 1549–1570.

(61) Goodgame, D. M. L.; Goodgame, M.; Rayner-Canham, G. W. *Inorganica Chim. Acta* **1969**, *3*, 406–410.

(62) Rubinstein, M.; Colby, R. H. *Polymer Physics*; Oxford University Press, 2003.

(63) Egan, P.; Sinko, R.; LeDuc, P. R.; Keten, S. *Nat. Commun.* **2015**, *6* (1), 7418.

(64) Kushner, A. M.; Guan, Z. *Angew. Chemie Int. Ed.* **2011**, *50* (39), 9026–9057.

(65) Römer, L.; Scheibel, T. *Prion 2* (4), 154–161.

(66) Guerette, P. A.; Ginzinger, D. G.; Weber, B. H.; Gosline, J. M. *Science* **1996**, *272* (5258), 112–115.

(67) Harrington, M. J.; Gupta, H. S.; Fratzl, P.; Waite, J. H. *J. Struct. Biol.* **2009**, *167* (1), 47–54.

(68) Kean, Z. S.; Hawk, J. L.; Lin, S.; Zhao, X.; Sijbesma, R. P.; Craig, S. L. *Adv. Mater.* **2014**, *26* (34), 6013–6018.

(69) Neal, J.; Mozhdehi, D.; Guan, Z. *J. Am. Chem. Soc.* **2015**, *137* (14), 4846–4850.

(70) Schmitt, C. N. Z.; Politi, Y.; Reinecke, A.; Harrington, M. J. *Biomacromolecules* **2015**, *16* (9), 2852–2861.

(71) Fantner, G. E.; Hassenkam, T.; Kindt, J. H.; Weaver, J. C.; Birkedal, H.; Pechenik, L.; Cutroni, J. A.; Cidade, G. A. G.; Stucky, G. D.; Morse, D. E.; Hansma, P. K. *Nat. Mater.* **2005**, *4* (8), 612–616.

(72) Presolski, S. I.; Hong, V.; Cho, S.-H.; Finn, M. G. *J. Am. Chem. Soc.* **2010**, *132* (41), 14570–14576.

(73) Daniele, P. G.; De Robertis, A.; De Stefano, C.; Sammartano, S. *J. Solution Chem.* **1989**, *18* (1), 23–36.

(74) Fullenkamp, D. E.; He, L.; Barrett, D. G.; Burghardt, W. R.; Messersmith, P. B. *Macromolecules* **2013**, *46* (3), 1167–1174.

(75) Yang, Y.; Urban, M. W. *Chem. Soc. Rev.* **2013**, *42* (17), 7446–7467.

(76) Stukalin, E. B.; Cai, L.-H.; Kumar, N. A.; Leibler, L.; Rubinstein, M. *Macromolecules* **2013**, *46* (18), 7525–7541.

(77) Bode, S.; Enke, M.; Bose, R. K.; Schacher, F. H.; Garcia, S. J.; van der Zwaag, S.; Hager, M. D.; Schubert, U. S. *J. Mater. Chem. A* **2015**, *3* (44), 22145–22153.

(78) Kersey, F. R.; Loveless, D. M.; Craig, S. L. *J. R. Soc. Interface* **2007**, *4* (13), 373–380.

(79) Menyo, M. S.; Hawker, C. J.; Waite, J. H. *ACS Macro Lett.* **2015**, *4* (11), 1200–1204.

(80) Zhukhovitskiy, A. V; Zhong, M.; Keeler, E. G.; Michaelis, V. K.; Sun, J. E. P.; Hore, M. J. A.; Pochan, D. J.; Griffin, R. G.; Willard, A. P.; Johnson, J. A. *Nat. Chem.* **2016**, *8* (1), 33–41.

(81) Grindy, S. C.; Learsch, R.; Mozhdehi, D.; Cheng, J.; Barrett, D. G.; Guan, Z.; Messersmith, P. B.; Holten-Andersen, N. *Nat. Mater.* **2015**, *advance on*.

(82) Krogsgaard, M.; Nue, V.; Birkedal, H. *Chem. - A Eur. J.* **2016**, *22* (3), 844–857.

(83) Broomell, C. C.; Chase, S. F.; Laue, T.; Waite, J. H. *Biomacromolecules* **2008**, *9* (6), 1669–1677.

(84) Srivastava, A.; Holten-Andersen, N.; Stucky, G. D.; Waite, J. H. *Biomacromolecules* **2008**, *9* (10), 2873–2880.

(85) Zhao, H.; Waite, J. H. *Biochemistry* **2006**, *45* (47), 14223–14231.

(86) Lichtenegger, H. C.; Schoberl, T.; Bartl, M. H.; Waite, H.; Stucky, G. D. *Science.* **2002**, *298* (5592), 389–392.

(87) Lichtenegger, H. C.; Schoberl, T.; Ruokolainen, J. T.; Cross, J. O.; Heald, S. M.; Birkedal, H.; Waite, J. H.; Stucky, G. D. *Proc. Natl. Acad. Sci.* **2003**, *100* (16), 9144–9149.

3.5 Experimental

General materials and methods: ^{1}H NMR and ^{13}C NMR spectra were recorded at 500 MHz and 125 MHz Bruker Instruments. Chemical shifts were reported in standard format as values in ppm relative to the signal of deuterated solvents. Gel permeation chromatography (GPC) was performed in THF (1 mL/min) using an Agilent LC 1100 Series equipped with Polymer Laboratory's PLgel 5 μm mixed-C column to determine molecular weights and molecular weight distributions, M_w/M_n, of the macro-CTAs with respect to polystyrene (PS) standards (Varian, Palo Alto, CA). L-ICP and B-ICP were analyzed by GPC using DMF as eluents supplemented with 0.1% LiBr (w/v) (1 mL/min) using an Agilent LC 1100 Series equipped with OHpak SB-803 HQ column from Shodex to determine molecular weights and molecular weight distributions, M_w/M_n, with respect to poly(ethylene glycol) (PEG) standards (Sigma Aldrich). GC-MS was obtained on ThermoFinnegen Trace MS+ instrument with DB-5 column (30m μ 0.25 mm μ 0.25μm film) with helium gas as carrier on positive EI mode. The mass spectrometry used electron ionization (70 eV) scanning (1/sec) from m/z 50-650.

All metal salts were stored and weighed in a Nitrogen glove box to minimize water absorption and ensure accurate L/M ratios. $Cu(NTf_2)_2$ and $Ca(NTf_2)_2$ were purchased from Aldrich. $Zn(NTf_2)_2$ was purchased from Strem Chemicals, Inc. $Co(NTf_2)_2$ was purchased from Alfa Aesar. $Cu(NTf_2)_2$ was obtained in hydrate form and the water content, reported in the Certificate of Analysis (determined by Karl Fischer titration), was used to calculate the molecular weight of the copper hydrate.

For butyl acrylate and styrene monomers, inhibitors were removed by passing through basic alumina column prior to polymerization. 4-vinylbenzyl chloride, technical grade, was used as received and was not passed through basic column before polymerization.

Thin layer chromatography, TLC, plates were stained by $KMnO_4$ for presence of double bonds and ninhydrin for the presence of the amine groups. The monomer was purified using CombiFlash® Rf+ automatic column using RediSep Rf Gold® Normal-Phase Silica as described in the monomer synthesis section.

Synthesis and characterization

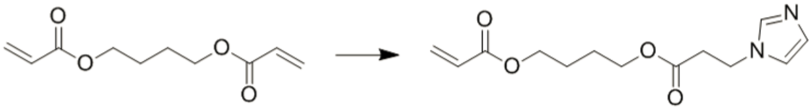

Synthesis of IMZa: The synthesis of IMZa was carried out as previously described.[1] The purity of IMZa was confirmed by GC-MS to ensure removal of all unreacted diacrylate starting material which would act as a cross-linking monomer if polymerized. Characterization matched previous literature values.[1]

GC Temperature gradient program: initial temperature: 35 °C, ramp/min: 10 °C/min, final temp: 290 °C.

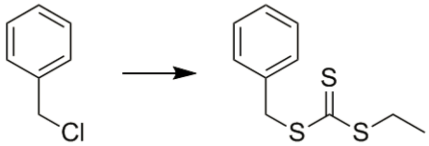

Synthesis of CTA: The synthesis of CTA was adapted from a previous procedure.[2] K_3PO_4 (21.6 g, 94 mmol) was suspended in acetone (100 mL) at room temperature. Ethanethiol (83 mmol) was added via disposable syringe, resulting in a color change to pale yellow. After stirring for 45 min, carbon disulfide (13.1 mL, 216 mmol) was added to the reaction mixture, resulting in a dark yellow appearance. Next, 4-vinylbenzyl chloride (10 mL, 72 mmol) was added to the reaction mixture and allowed to stir for 24 h at room temperature. The reaction was then poured into chloroform (200 mL) and extracted with water (2 x 100 mL), brine (1 x 100 mL), dried over anhydrous Na_2SO_4, and the solvent evaporated to afford the desired chain transfer agent.

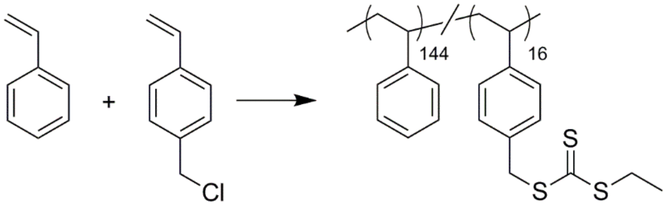

Synthesis of macro-CTA: The synthesis of macro-CTA was carried out as previously described.[1] Macro-CTA was synthesized to possess 10% initiator and was calculated to contain 0.65 mmol initiator/1 g of polymer.

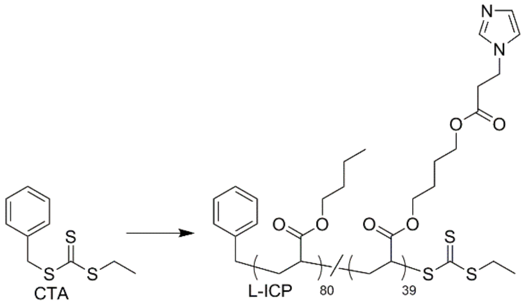

Synthesis of L-ICP: The polymerization of L-ICP was adapted from a previously described procedure.[1] A representative polymerization procedure follows. Two separate L-ICP batches were combined to provide enough uniform samples for the rheological studies. Using ^{1}H NMR, the IMZa content was calculated to be 1.87 mmol/1 g of polymer.

CTA (129 mg, 0.563 mmol) was added to a Schlenk flask. IMZa (10.2 g, 38.3 mmol), BA (9.53 g, 74.3 mmol), and 3.2 mL anisole as NMR internal standard were dissolved in DMF (75.1 mL, 1.5 M with respect to vinyl moiety). AIBN (18 mg) was transferred to reaction flask ([Monomer]:[CTA]:[AIBN] = 200:1:0.2). 50 μL sample was taken for calculating the conversion using ^{1}H NMR and reaction flask was sealed by a rubber septum. The reaction mixture was then purged with a stream of N_2 for 1 h. Schlenk flask was immersed in an oil bath thermostatted at 65 °C. After 190 min, the reaction was removed from the oil bath and was cooled on ice. The conversion was determined via ^{1}H NMR by comparing the integration of vinyl protons with respect to anisole protons (OCH_3). 30 mg of 4-methoxyphenol was added as radical inhibitor to the reaction and the reaction mixture was concentrated in vacuo. The residue was transferred to Nalgene centrifuge tubes and the polymer was precipitated in Et_2O/Hexane mixture, (1:3 v/v) followed by centrifugation at 8500 rpm, for 10 min at 4 °C. The supernatant was decanted and the polymer was dissolved in CH3CN and precipitated in Et_2O/Hexane (4:1 v/v). Finally, the polymer was precipitated in pure Et_2O three times. The polymer was then dissolved in CH_3CN and the stock solution was kept at 4 °C. To quantify the concentration of polymer (mg/mL), known volume of polymer solution was transferred to three oven dried pre-tared 1 dram vials. The solution was then completely dried by placing the vials in pre-heated oven at 80 °C for 18 h under reduced pressure (< 1 mTorr). The average mass of these three samples was used to calculate the concentration of stock solution.

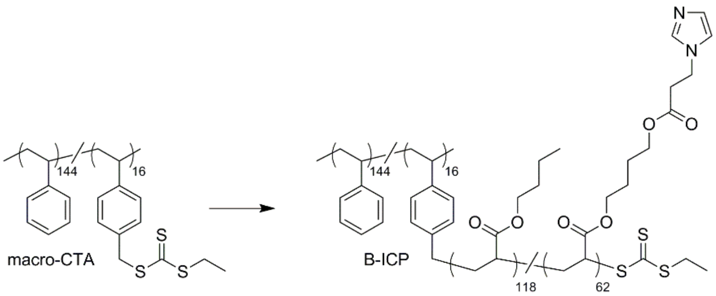

Synthesis of B-ICP: The polymerization of B-ICP was adapted from a previously described procedure.[1] Two separate B-ICP batches were combined to provide uniform samples to complete tensile testing and self-healing studies. The average brush contained 34% IMZa as found via ^{1}H NMR. IMZa content was determined via calculations explained in the previous publication.[1] The IMZa content was calculated to be 1.88 mmol/1 g of polymer.

.

Calculation of theoretical imidazole content: The theoretical imidazole content of each polymer was calculated after characterization of copolymers using ^{1}H NMR. The calculation was carried out as previously reported.[1] Imidazole content for polymers used in this study is reported in Table S3.1.

Table S3.1 Theoretical IMZa content (mmol/g) for L-ICP and B-ICP

Polymer	IMZa content (mmol/g)
L-ICP	1.87
B-ICP	1.88

Metal Incorporation: Generally, the metal di[bis(trifluoromethylsulfonyl)imide] salt of interest was dissolved in CH_3CN and added slowly (50–100 μL increments) to a solution of ICP in CH_3CN. Between metal salt additions, the polymer solution was agitated with a vortex mixer until a homogeneous solution was obtained.

L-ICP metal incorporation for solution rheology: The metal di[bis(trifluoromethylsulfonyl)imide] salt of interest was dissolved in 2.3 mL of CH_3CN and added slowly (100 μL increments) to a solution of L-ICP in CH_3CN (initial polymer concentration 372 mg/mL). After addition of each increment, the polymer solution was agitated with a vortex mixer until a homogeneous solution was obtained. After addition of all metal, polymer solutions were analyzed by rheometer according to procedures described in mechanical characterization section. The final polymer concentration of solution rheology samples was held constant at 85 mg/mL.

Metal incorporation for B-ICP: The metal di[bis(trifluoromethylsulfonyl)imide] salt of interest was dissolved in 3.0 mL of CH_3CN and added slowly (100 µL increments) to a solution of B-ICP in CH_3CN (starting polymer concentration 171 mg/mL, final concentration 75 mg polymer/mL). After addition of each increment, the polymer solution was agitated with a vortex mixer until a homogeneous solution was obtained. After completing the metal incorporation, the polymer solution was transferred to a Teflon mold and the solvent was allowed to evaporate at ambient conditions (~5 h). Next, the samples were further dried in a vacuum oven at 80 °C for 5 h (100 Torr). Finally, the sample was dried overnight at 80 °C (0.1 Torr) to ensure complete removal of solvent. Tensile samples were prepared by compression molding at 100 °C.

Mechanical characterization via solution rheology: Solution rheology data were collected on an AR-G2 Rheometer from TA Instruments (40 mm cone plate with solvent trap, 1.998° cone angle, 60 μm gap). Samples were studied at 0.085 g polymer/mL in acetonitrile. A frequency sweep was conducted from 0.1 – 50 Hz with constant 25% strain at 20 °C.

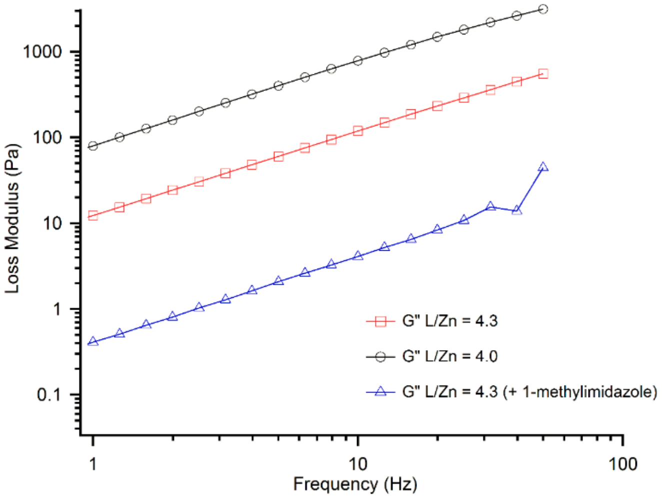

Figure S3.1 The effect of free-imidazole on the viscosity of the L-ICP-Zn solutions. Solution dynamic viscosity (η = G″/ω) increases as more Zn^{2+} is added, L/Zn = 4.3 (red) to L/Zn = 4.0 (black). Addition of N-methylimidazole, reduced the viscosity drastically, (L+L')/Zn = 4.3 (blue).

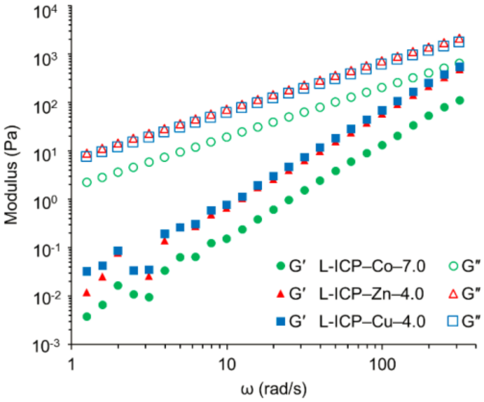

Figure S3.2 Solution rheological studies of L-ICP–M samples. (a) Representative rheological characterization of L-ICP–M CH_3CN solutions. The storage (filled symbols) and loss (open symbols) modulus are shown. None of the solutions formed stable gels and behaved as fluids across the experimental range.

Table S3.2 Dynamic viscosity of **L-ICP–M** dissolved in CH_3CN

Zinc		**Copper**		**Cobalt**	
L/M	Dynamic Viscosity (Pa.s)	L/M	Dynamic Viscosity (Pa.s)	L/M	Dynamic Viscosity (Pa.s)
3.8	6.5	3.8	5.3	6.5	1.3
4.0	7.2	4.0	6.0	7.0	2.0
4.2	4.5	4.2	2.7	7.5	1.5
4.4	0.10	4.4	0.40	8.0	0.52
4.6	0.043	4.6	0.20	10.0	0.16
6.0	0.020	4.8	0.090	15.0	0.022
8.0	0.017	6.0	0.030		
10.0	0.020	8.0	0.022		
15.0	0.016	10.0	0.018		
		15.0	0.019		

Mechanical characterization via melt rheology: Melt rheology was measured on an Anton-Paar MCR 302 rheometer in a 25 mm diameter parallel-plate geometry. Frequency sweeps were performed from ω = 100 rad/s to 0.1 rad/s at T = 80, 70, 60, 50, 40, 30, and 20 °C at $\gamma = 1$ %. Master curves were generated using the time-temperature superposition algorithm of Bae *et al.*[3]

The complex viscosity is calculated according to the following equation:

$$|\eta^*| = \frac{\left(G'^2 + G''^2\right)^{0.5}}{\omega} = \frac{|G^*|}{\omega}$$

Where |G*| is the magnitude of the complex modulus and the w is the angular frequency.

In our melt rheology experiments, we identify two materials properties, which characterize the basic rheological response: the zero-shear viscosity, η_0, defined as the viscosity in the low frequency limit; and the critical shear-thinning frequency, defined as the frequency above which the viscosity begins to decrease. The inverse of the critical shear-thinning frequency ($\tau = 1/\omega_c$) identifies the terminal relaxation timescale that is proportional to the dynamics of network relaxation. Zero-shear viscosity depends on the polymer cross-linking density and the relaxation rate, which is affected by the dynamics of ligand exchange.

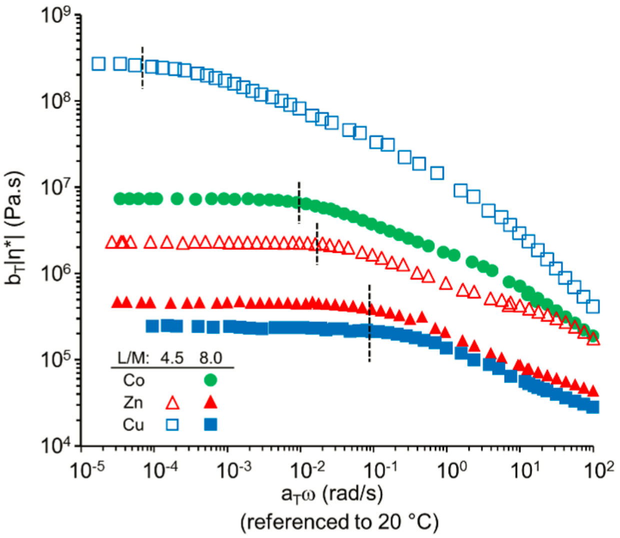

Figure S3.3 Complex viscosity of L-ICP–M samples at different shear rates referenced to 20 °C using time–temperature superposition from data taken at 20–80 °C. Critical shear thinning frequency is marked by a vertical dashed line for each sample. At L/M = 8.0 (filled symbols), the zero-shear viscosity and the critical relaxation time scale of L-ICP samples cross-linked with Cu^{2+} and Zn^{2+} are similar while the viscosity and the critical relaxation time scale of L-ICP–Co–8.0 is over an order of magnitude larger. As the L/M ratio decreases from 8.0 (closed symbols) to 4.5 (open symbols), the difference between the viscosity and the critical relaxation time scale of L-ICP–Cu and L-ICP–Zn increases significantly. At L/M = 4.5, L-ICP–Cu is 100-fold more viscous than L-ICP–Zn.

Sample preparation for tensile testing: B-ICP samples for bulk mechanical characterization were prepared via compression molding. Samples were heated in Teflon molds to 100 °C and hot pressed. Samples were allowed to quickly cool to room temperature (~30 min) while under pressure. Average sample size was 15 mm x 7 mm x 2 mm.

B-ICP samples for self-healing studies were prepared via compression molding at 100 °C, followed by gradual cooling under pressure to room temperature over 12 h. Slow cooling of these samples was carried out to remove residual stress from polymer samples. All samples used for self-healing studies (cut and pristine samples) were processed in this manner. B-ICP–M samples were cut with a fresh blade (75% of width) through the center and subsequently pushed back together for 1 min. Samples were left to stand in air for the duration of the experiment at room temperature. Each measurement was repeated at least three times.

Mechanical testing procedure: The mechanical properties of B-ICP samples were measured using an Instron 3365 machine. Standard stress/strain experiments were performed on samples at room temperature. Samples were extended at a rate of 100 mm/min. Each measurement was repeated at least three times.

Table S3.3 Summary of mechanical properties for B-ICP-M cross-linked with Co^{2+}, Zn^{2+}, and Cu^{2+}

M	L/M	E^a (MPa)	σ^b (MPa)	$\varepsilon_{ult}{}^c$ (mm/mm)	$U_T{}^d$ (MJ/m^3)
Co^{2+}	7.0	49 ± 6	2.8 ± 0.2	3.5 ± 0.2	8.2 ± 0.3
	8.0	21 ± 3	1.8 ± 0.2	5 ± 1	8 ± 2
	9.0	14 ± 3	1.6 ± 0.2	6.5 ± 0.4	8.3 ± 0.8
	10.0	10 ± 1	1.2 ± 0.1	9 ± 2	9 ± 2
Zn^{2+}	4.0	50 ± 8	8.7 ± 0.8	1.00 ± 0.09	5.7 ± 0.4
	4.5	14 ± 1	1.6 ± 0.1	5.9 ± 0.6	6.3 ± 0.7
	5.0	10 ± 2	1.9 ± 0.2	7 ± 2	10 ± 4
	6.0	4 ± 1	1.5 ± 0.2	7 ± 1	8 ± 2
	8.0	3.2 ± 0.4	1.4 ± 0.1	8 ± 1	8 ± 1
Cu^{2+}	4.0	110 ± 15	10.2 ± 0.5	0.79 ± 0.03	6.3 ± 0.4
	4.5	77 ± 5	5.7 ± 0.3	1.8 ± 0.1	9 ± 1
	5.0	24 ± 4	2.99 ± 0.08	4.1 ± 0.6	8 ± 2
	6.0	7 ± 2	1.8 ± 0.3	5 ± 1	7 ± 1
	8.0	3.0 ± 0.4	1.3 ± 0.1	5.0 ± 0.8	4 ± 1

*Strain rate: 100 mm min^{-1}, 25 °C. ^{a}Young's modulus, calculated from the initial slope of stress-strain curves; ^{b}ultimate tensile stress; ^{c}ultimate extensibility (mm/mm); ^{d}toughness, calculated by manually integrating the area under the stress-strain curve.

B-ICP–Ca static tensile test:

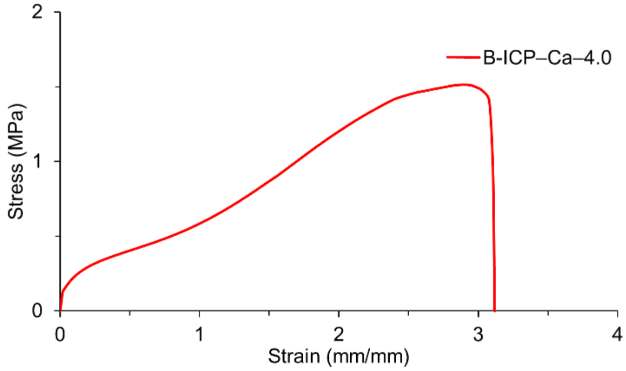

Figure S3.4 Static tensile tests of B-ICP–Ca–4.0 to demonstrate that the observed B-ICP–M mechanical property changes are not artifacts of ionic interactions. The resulting B-ICP–Ca–4.0 materials were significantly weaker than B-ICP–Cu and B-ICP–Zn with L/M = 4.

Sample damaging and healing tests: B-ICP samples were cut with a fresh blade (75% of width) through the center and subsequently pushed back together for 1 min. Samples were left to stand in air for the duration of the experiment at room temperature. Each measurement was repeated at least three times.

Theoretical calculation of fraction of various ML_n species: The theoretical population of each ML_n species was calculated by solving a series of non-linear equations similar to titration problems. Equilibrium constants were used from Table 7 (I = 0) of reference 4, critical survey of literature reports of imidazole-metal binding constants commissioned by the IUPAC.[4] A sample calculation is provided below for the ZnL_n system.

$$K_1 = \frac{[ZnL]}{[Zn][L]}$$

$$K_2 = \frac{[ZnL_2]}{[ZnL][L]}$$

$$K_3 = \frac{[ZnL_3]}{[ZnL_2][L]}$$

$$K_4 = \frac{[ZnL_4]}{[ZnL_3][L]}$$

$$[M_0] = [M] + [ML] + [ML_2] + [ML_3] + [ML_4]$$

$$[L_0] = [L] + [ML] + 2 \times [ML_2] + 3 \times [ML_3] + 4 \times [ML_4]$$

where $[M_0]$ is the initial concentration of metal (zinc) and $[L_0]$ is the initial concentration of ligand. The last two equations describe the mass balance for metal and ligand. For the sake of simplicity, the initial concentration of ligand $[L_0]$ is assumed to be 1 M and the equations were solved analytically using Mathematica® software for different amount of added metal, $[M_0]$. The population of each ML_n species for Zn and Cu at various L/M ratios is plotted in Figure S3.5.

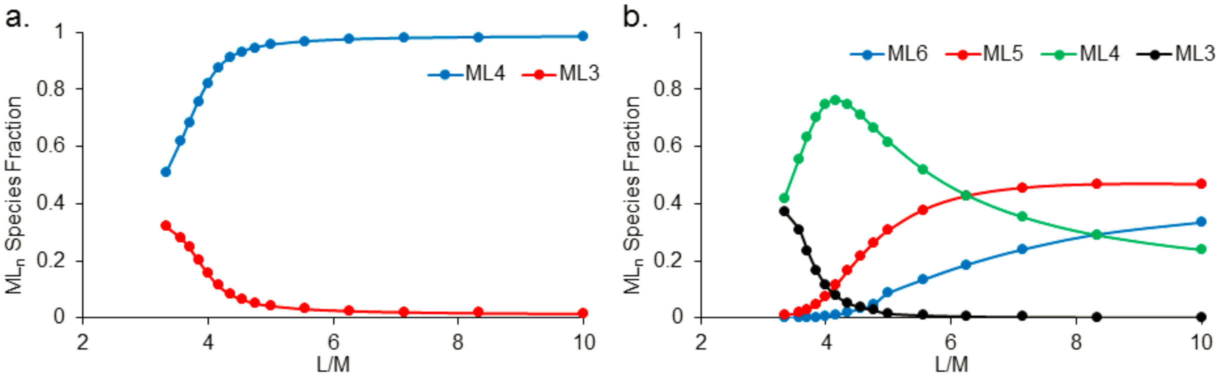

Figure S3.5 Calculated concentration of different ML_n species for M = Zn (a) and Cu (b) at different L/M ratio.

Theoretical rate of exchange: The theoretical rate of exchange was calculated based on the concentration of free ligand at various M/L ratios for both an associative-dissociative and a strictly dissociative mechanism.

Here, we describe rate of exchange as

$$R_{associative-dissociatinve} = k[ML_4][L]$$
$$R_{dissociative} = k[ML_4]$$

using known populations of $[ML_4]$ and $[L]$ from the above section, we calculated the rate of exchange at any L/M ratio. Figure S3.6 shows the relationship between the inverse of rate of exchange and L/M ratio. Specifically, a sharp decrease in rate of exchange occurs near L/M = 4 for the associative-dissociative mechanism (Figure S3.6a). Conversely, rate of exchange remains constant for the dissociative mechanism (Figure S3.6b).

This simple calculation also qualitatively predict the sharp increase in the viscosity near L/M =4 for Cu^{2+} and Zn^{2+} systems by assuming that the dynamic viscosity is inversely proportional to the rate of the ligand exchange reaction (Figure 3.2a).[5,6] We are excluding the cross-linking density and fraction of inter-chain versus intra-chain connections from this calculation. These topological parameters are mainly affected by the equilibrium constants and are not dependent on the mechanism of ligand exchange.

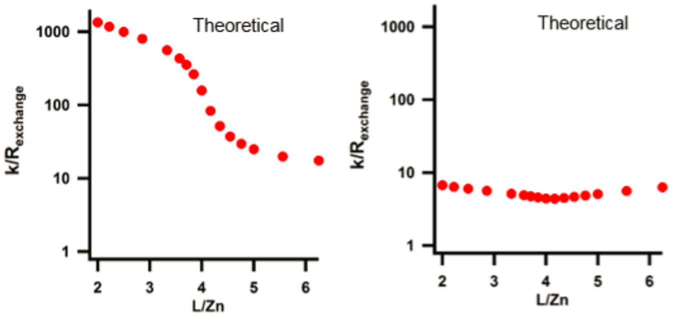

Figure S3.6 Theoretical dependence of viscosity on L/M ratio for associative-dissociative (a) and dissociative (b) mechanisms for various L/M ratios. Viscosity is inversely proportional to the rate of the ligand exchange.

3.6 References for Experimental

(1) Mozhdehi, D.; Ayala, S.; Cromwell, O. R.; Guan, Z. *J. Am. Chem. Soc.* **2014**, *136* (46), 16128–16131.

(2) Skey, J.; O'Reilly, R. K. *Chem. Commun.* **2008**, No. 35, 4183.

(3) Bae, J.-E.; Cho, K. S.; Seo, K. H.; Kang, D.-G. *Korea-Australia Rheol. J.* **2011**, *23* (2), 81–87.

(4) Sjöberg, S. *Pure Appl. Chem.* **1997**, *69* (7), 1549–1570.

(5) Yount, W. C.; Loveless, D. M.; Craig, S. L. *Angew. Chemie Int. Ed.* **2005**, *44* (18), 2746–2748.

(6) Yount, W. C.; Loveless, D. M.; Craig, S. L. *J. Am. Chem. Soc.* **2005**, *127* (41), 14488–14496.

3.7 Chapter 3 Spectra

CTA. ^{1}H NMR (600 MHz, CD_3CN, 298 K)

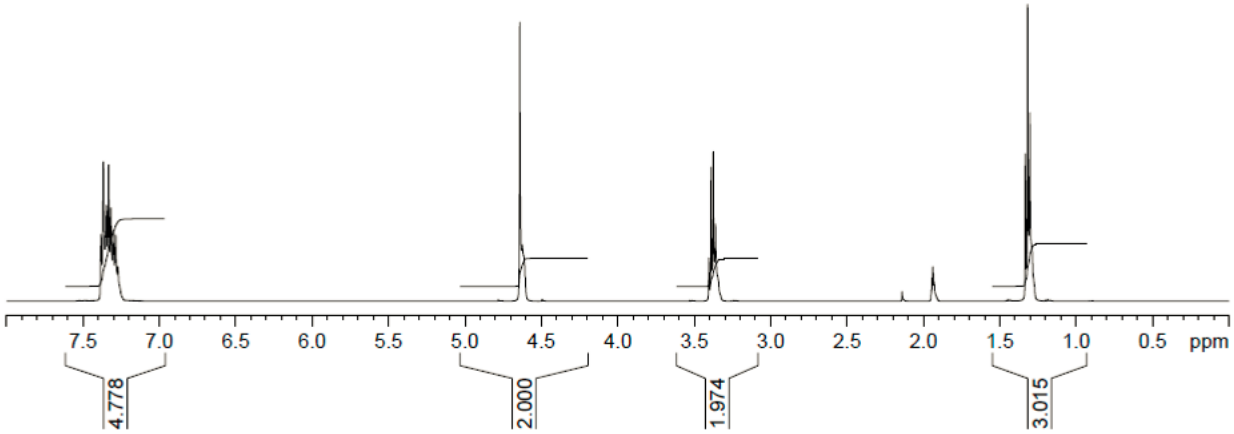

CTA. ^{13}C NMR (125 MHz, $CDCl_3$, 298 K)

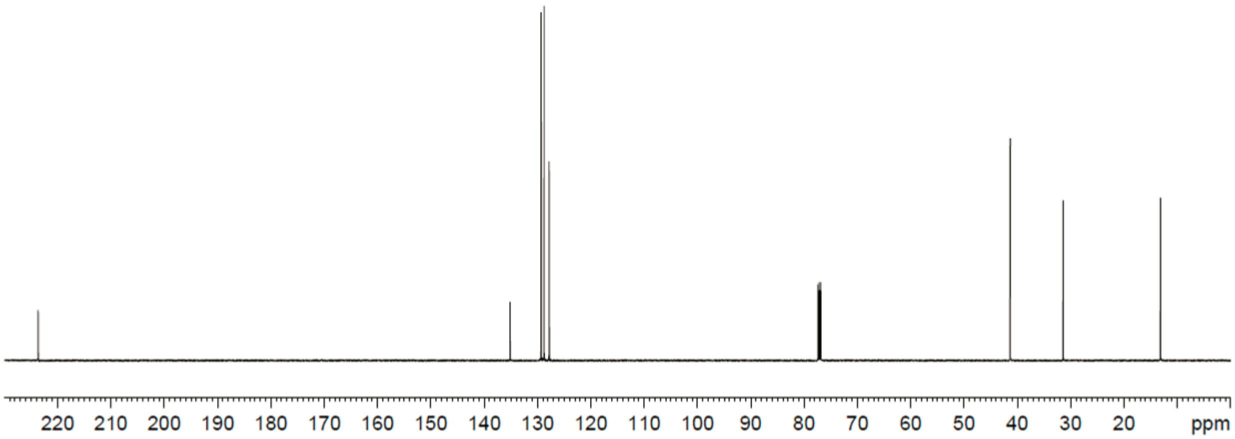

macro-CTA. ^{1}H NMR (500 MHz, CD_2Cl_2, 298 K)

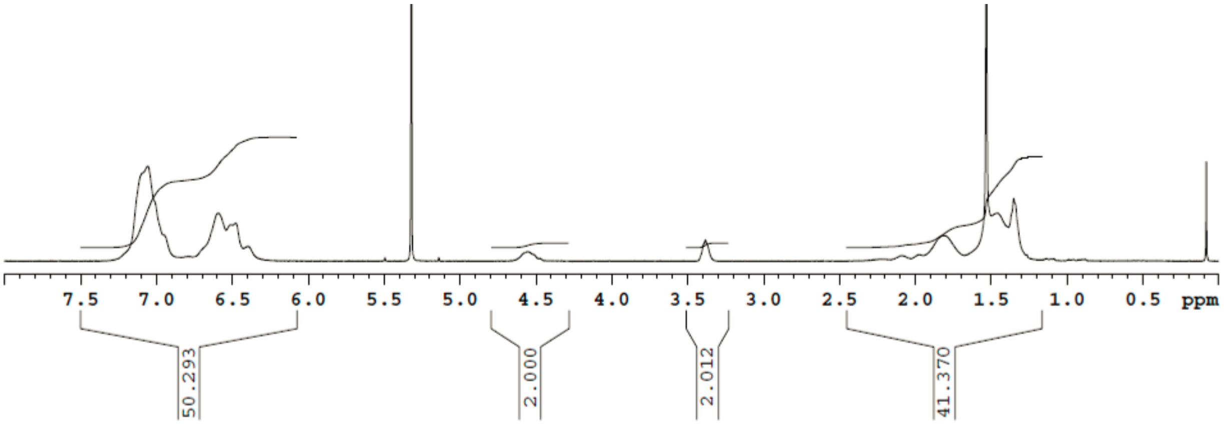

GPC trace of macro-CTA. GPC (THF eluent, PS standard) M_n: 19,100 Da, M_w/M_n: 2.08

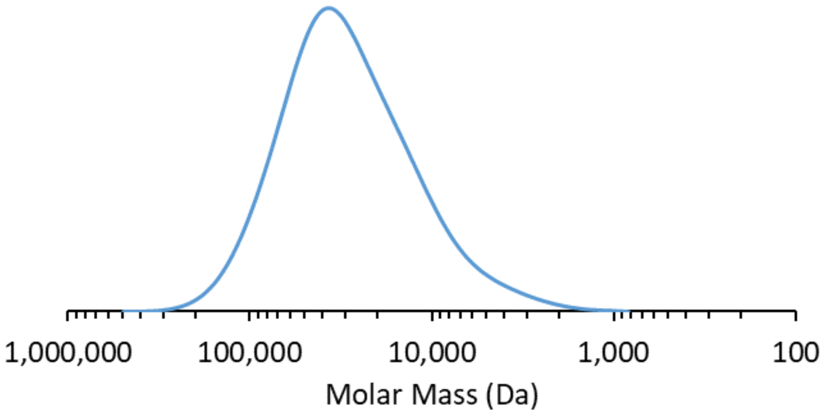

L-ICP. ^{1}H NMR (500 MHz, DMSO-d_6, 298 K). IMZa incorporation ratio determined by comparison of singlet at 7.6 ppm vs triplet at 0.9 ppm.

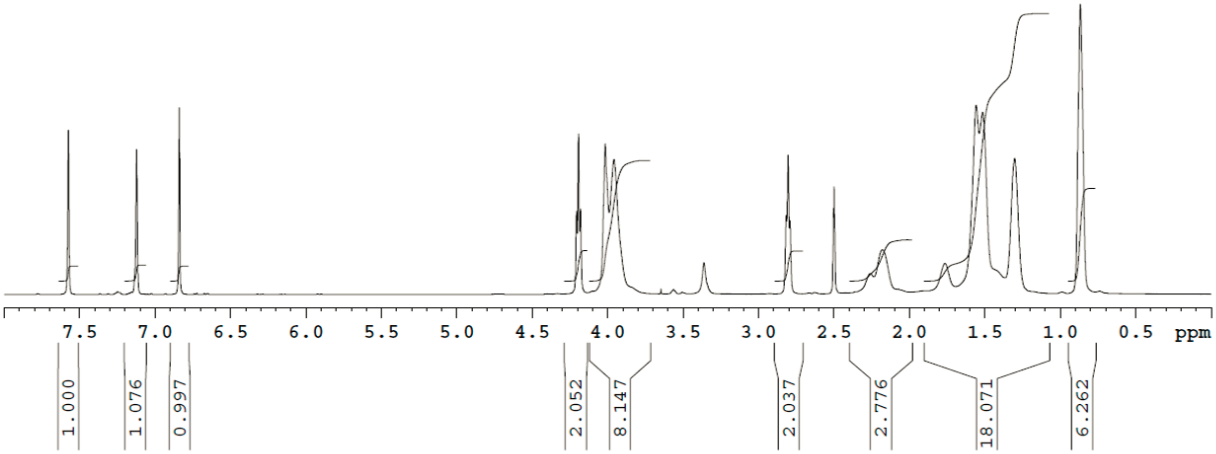

GPC trace of L-ICP. GPC (DMF eluent, PEG standard) M_n: 4,900 Da, M_w/M_n: 1.53

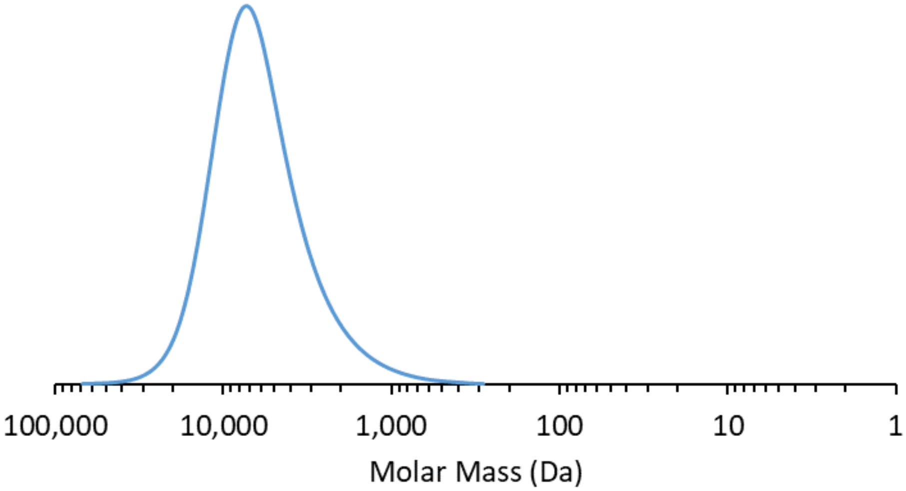

B-ICP. ^{1}H NMR (500 MHz, DMSO-d_6, 298 K).

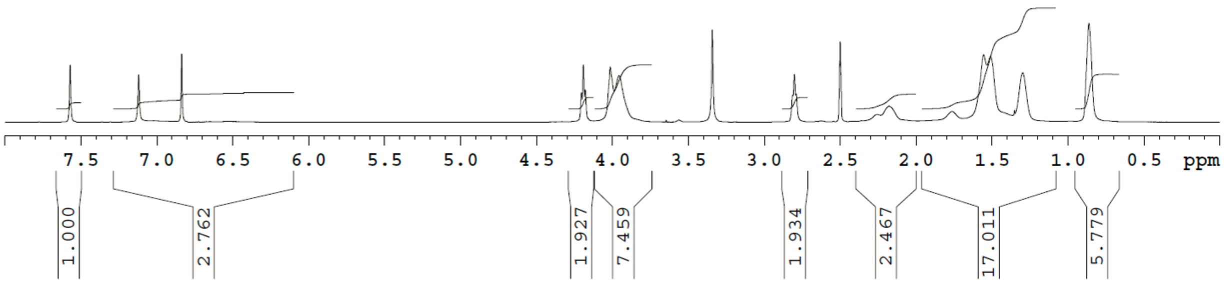

GPC trace of B-ICP. GPC (DMF eluent, PEG standard) M_n: 95,600 Da, M_w/M_n: 1.23. *~10% smaller molecular weight fraction from free chain polymerization is also present.

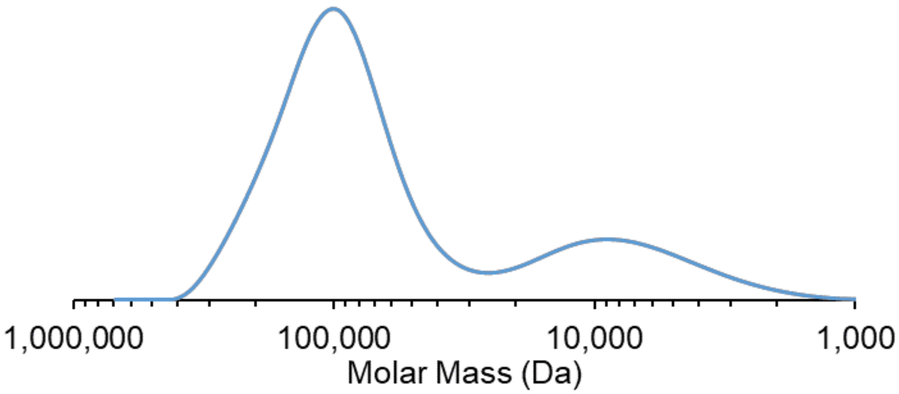

Chapter 4: Large Continuous Mechanical Gradient Formation via Metal–Ligand Interactions

4.1 Introduction

4.1.1 The current state of gradient materials

Materials that provide form and function in living organisms generate and withstand tremendous forces. For example, the club of a peacock mantis shrimp (Odontodactylus scyllarus) can experience up to 700 N during a strike.[1] This massive force must be mitigated when transferring between the hard club and soft tissues of the shrimp to prevent serious damage. Cleverly, the dissipation of the large forces is accomplished through a continuous gradient in mechanical properties from hard to soft. Gradients like this allow the forces to be distributed, preventing stress buildup and catastrophic failures in the tissues of living organisms.[2]

Synthetic analogs of these natural mechanical gradients have been long pursued to create stronger materials with improved thermal and mechanical stress dissipation as well as fracture toughness at interfaces.[2] Synthetic mechanical gradients are generally obtained in a layered or lateral orientation. Layered gradients are printed layer-by-layer onto surfaces and are not true continuous gradients due to the segmented fabrication process.[3–5] Some lateral gradients are able to obtain smooth transitions,[6–10] but there are few examples due to the complex synthetic effort required to generate them. Notable examples of previously reported lateral gradients include photoinduced crosslinking of cellulose nanocrystals,[7] ordering of carbon nanotube films,[11] and cellulose nanofibril/polymer nanopapers.[12] While these and other synthetic analogs are functional mechanical gradients,[6,8–10,13–19] they often suffer from relatively small ranges in stiffness (~1 order of magnitude), non-continuous stepwise transitions, and require specialty equipment to fabricate. To improve upon these systems, we sought a synthetic solution that could span a greater range of mechanical properties with a true continuous gradient and facile synthesis. Many examples of gradient materials exist in nature,[20–25] but when searching for routes to gradient formation, the jaw of the polychaete worm became a unique source of inspiration (Figure 4.1). In contrast to the mineralization and covalent crosslinking used to form many natural gradients,[26–28] the polychaete worm relies on metal–ligand interactions to create a rigid jaw tip to inject venom.[29–31] Specifically, by creating a gradient of zinc or copper through a histidine rich protein network, the increasing number of metal–histidine interactions act as crosslinks and create a mechanical gradient, which can prevent damage to the jaw tip during biting and venom injection.

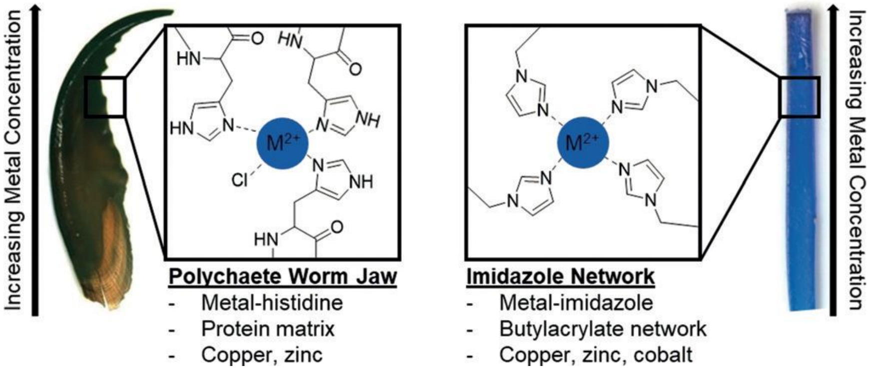

Figure 4.1 Comparison of natural and synthetic gradients. Specifically, the metal–histidine[32] gradient found in the polychaete worm jaw[30] (left) and the metal–imidazole gradient made in this work (right).

4.1.2 Our design for continuous mechanical gradient formation

In one of our previously reported studies, we investigated control of mechanical properties by altering metal identity (Zn, Cu, Co) and concentration in an imidazole-containing metallopolymer network.[33,34] We employed monodentate imidazole ligands to create dynamic metal–ligand crosslinks. In this past work we found that a weakly binding solvent (acetonitrile, ACN) facilitated ligand exchange (no gelation). Upon solvent removal the rate of ligand exchange was significantly reduced to create crosslinks that tuned mechanical properties based on metal concentration.

Herein, we leverage our understanding of dynamic imidazole–metal interactions to generate a gradient crosslinked metallopolymer network that exhibits a range of mechanical properties, mimicking the polychaete jaw (Figure 4.1). To incorporate a gradient of metal into the material, we imagined that we could suspend a polymer sample in a metal salt solution and simultaneously raise it out of the solution, while increasing metal concentration in the reservoir. The dynamic nature of the metal–ligand interaction in the presence of ACN would allow for rapid exchange and metal incorporation into the bulk of the material. Subsequent removal of the solvent would drastically lower the exchange rates of the metal–ligand interactions, resulting in solid materials with stable gradients of metal concentration and mechanical properties (Figure 4.2).

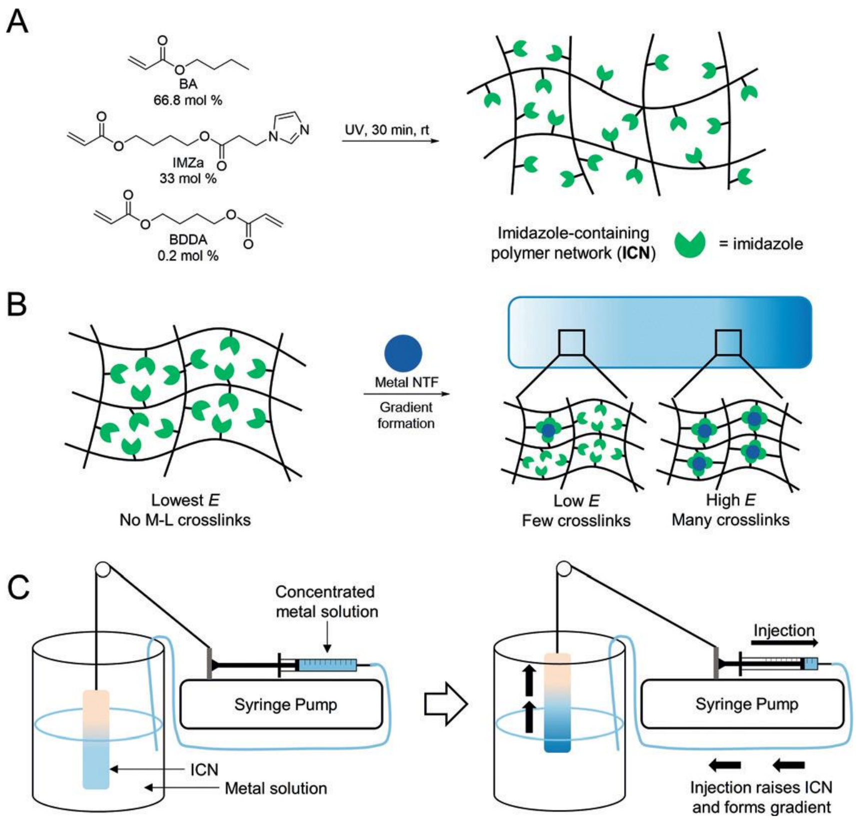

Figure 4.2 Design concept for gradient material. (A) Synthesis of the imidazole-containing network (ICN). (B) Cartoon depicting metal incorporation into the ICN to form gradient ICN-M. (C) Cartoon depicting the use of a common laboratory syringe pump, termed continuous gradient patterner (CGP), to fabricate the gradient sample.

4.2 Results and Discussion

4.2.1 Synthesis and characterization

The synthesis of the imidazole-containing network (ICN) is described in Figure 4.2A. An imidazole-containing acrylate monomer (IMZa) was copolymerized with butyl acrylate (BA) and 1,4-butanediol diacrylate (BDDA) via UV-initiated polymerization to achieve the ICN. BA was used to lower the glass transition temperature, enhance ligand mobility, and create an initial network with the desired mechanical properties. The BA, IMZa, and BDDA were used in a 66.5:33:0.5 molar ratio, respectively, to achieve the polymer network. The monomer feed ratios were selected based on our previous study, where IMZa incorporation over 35 mol% gave diminished returns of increased mechanical properties.[33] After the synthesis of the ICN, a metal salt (Zn, Cu, or Co) was incorporated via controlled diffusion to form ICN-metal complex (ICN-M). [Bis(trifluoromethylsulfonyl)-imide] (NTF) was selected as the counter ion for all metals due to its well-characterized behaviour, thermal stability, and high mobility in the solid state.

4.2.2 Gradient formation via continuous gradient patterner

To create the metal gradient in ICN (Figure 4.2B), a simple device was designed from a common laboratory syringe pump. The device, termed a continuous gradient patterner (CGP, Figure 4.2C) works by first attaching the polymer sample (3 x 0.8 x 25 mm) via string to the pusher block of the syringe pump and then suspending the sample in a graduated cylinder filled with a stirring solution of metal NTF salt dissolved in ACN. A 1 mL syringe containing a highly concentrated metal NTF salt solution in ACN was adjusted to the length of the sample, such that, while the additional metal solution was being injected into the graduated cylinder, the sample would be slowly raised out of the solution, allowing a gradient to be formed. All ICN-M gradient samples were formed starting with the molar ratio of 0.167 metal atoms per imidazole (i.e., [imidazole]/[metal]=6.0). During the CGP process, more metal salt was gradually added to finally raise the molar ratio to 0.25 metal atoms per imidazole (i.e., [imidazole]/[metal]= 4.0, details see Experimental section for detailed calculations). These selected values were determined experimentally, as both too much and too little added metal resulted in consistently weaker materials (Figure S4.1). The syringe pump was set on the lowest flow rate, which typically allowed the polymer sample to raise from the metal solution over 2 days, giving sufficient time for the metal to incorporate into the bulk of the sample. After completion of the CGP process, residual solvent was removed from the crosslinked samples in a vacuum oven.

4.2.3 Mechanical properties via instrumented indentation

After metal incorporation and removal of ACN, the bulk mechanical properties of ICN-M samples were studied via indentation using a Nanovea indenter. The Young's modulus (E) and local hardness were calculated based on the single indentation of a spherical tip (radius = 100 mm). Instrumented indentation was selected for characterization because it allows for small, precisely controlled testing areas. To ensure that bulk mechanical properties of samples were characterized, the indentation depth of the large tip was kept constant at 15 mm. This ensures any artificially stiff top layer was by-passed and the bulk sample was fully characterized.[35] Each ICN-M sample was tested along its length axis to characterize gradient formation.

Young's modulus results (Figure 4.3A) illustrate that the highest stiffness for all ICN-M samples occur at the end of the sample which remained in the metal solution the longest, and that all samples display gradual stiffness decrease along their length axis. ICN-Zn displayed the highest stiffness for all tested samples at 108:7 MPa (Table 4.1). Additionally, ICN-Zn possessed the largest and most gradually decreasing gradient span from 108 ± 7 to 0.59 ± 0.01 MPa. To the best of our knowledge, at over two orders of magnitude (230 fold increase), this stiffness gradient represents the largest continuous synthetic mechanical gradient made to date. In fact, this range in stiffness closely matches the magnitude of gradient observed in squid beaks, a benchmark for many gradient materials.[21] After ICN-Zn, ICN-Cu displayed the next highest maximum stiffness (46 ± 1 MPa), followed by ICN-Co (25 ± 2 MPa) (Table 4.1). To confirm that the indentation data represent bulk mechanical properties, non-gradient bulk (Bulk-M) samples were prepared for tensile testing. Bulk-M samples with identical polymer composition and thickness were swelled with metal salt to mimic the stiffest end of gradient samples ([imidazole]/[M^{2+}] = 4.0). The data showed strong agreement between indentation and tensile measurements (Table S4.2), validating the use of indentation for testing the mechanical properties. Given the fact that the CGP fabrication method relies on metal infiltration from the surface to the center of samples, there is likely a gradient of mechanical properties through the thickness of the sample, which is hard to measure by either indentation or tensile technique. Nevertheless, the final result is a continuous gradient in bulk mechanical properties along the length axis. The local hardness of all specimens was also determined via instrumented indentation (Figure S4.2). In general, the observed hardness gradients spanned over one order of magnitude. Interestingly, ICN-Co displays the highest hardness of all samples, rather than ICN-Zn. This may be because Co–imidazole complexes exist as ML_6 species, while Zn–imidazole complexes exist as ML_4 complexes. This higher degree of crosslinks per metal atom could lead to a higher resistance to permanent shape change (i.e., hardness).

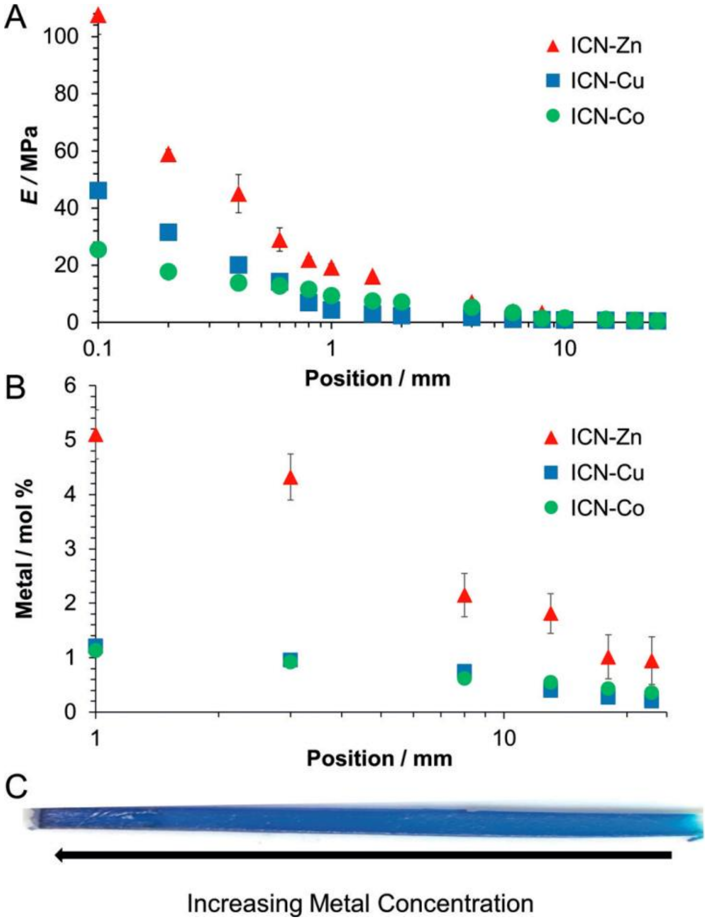

Figure 4.3 Spatial analysis of mechanical properties and metal concentration. (A) Gradient of Young's modulus (E) along the lateral axis of the samples as determined by instrumented indentation. (B) Relative metal concentration (with respect to C, N, O) along the lateral axis of the samples as determined by XPS (C) An image of the ICN-Cu sample.

Table 4.1 Minimal and maximal stiffness of each ICN material

Sample	Max. E[a]	Min. E[a]	Fold Increase
ICN-Zn	108 ± 7	0.47 ± 0.01	230
ICN-Cu	46 ± 1	0.38 ± 0.01	121
ICN-Co	25 ± 2	0.34 ± 0.01	74

[a] Young's modulus (E) is measured in MPa via instrumented indentation

4.2.4 Quantification of metal concentration in gradient samples via X-ray photoelectron spectroscopy

To confirm that the stiffness and hardness gradients were caused by the gradient of incorporated metal ions, X-ray photoelectron spectroscopy (XPS) was employed to determine relative metal concentrations along the lateral axis of the specimen. XPS was chosen because it can detect small metal concentrations, examine spatially distinct locations along the lateral axis, and is generally non-destructive to the sample. An argon gas cluster ion source (GCIS) was used to remove surface contaminants (Ar2000+, 5 keV). Region scans of the major atomic components (C, O, N) of the ICN were used to determine the relative abundance of the metal ions (Zn, Cu, Co) and confirm that the correct atomic ratios of elements were present for the ICN (see the Experimental section for details of XPS determination). Indeed, along the lateral axis of the specimen, gradients of all 3 metals were observed (Figure 4.3B). ICN-Zn contains the largest relative percentage of metal (ranging from 0.9–5.1 %, Table 4.2) while ICN-Cu and ICN-Co contain less relative metal (ranging from 0.20–1.21 % and 0.35–1.13 % respectively, Table 4.2). Determination of metal concentration closer than 1 mm from the edge of the sample was not possible due to signal interference from the sample holder. Due to the small penetration depth of XPS, energy-dispersive X-ray spectroscopy (SEM-EDX) spectra were obtained for ICN-Zn to confirm that the zinc salts could penetrate deep into the ICN sample. SEM-EDX measurements were performed on the surface and at the center of the cross-section at various locations along the length axis of the sample (Figure S3). SEM-EDX showed that metal concentration in ICN-Zn decreased by about 50 % from the surface to the center, indicating that a gradient along the thickness of the sample has also been formed. Presumably, this gradient is formed due to the decreased mobility of metal ions within the polymer network. While this gradient along the thickness does not compromise the formation of gradient mechanical properties in bulk along the length axis, reduction of this effect should be feasible through further engineering controls.

Table 4.2 Minimal and maximal relative metal amount of each ICN material

Sample	Max Metal mol %[a]	Min Metal mol %[a]	Fold Increase
ICN-Zn	5.1 ± 0.5	0.9 ± 0.4	5.7
ICN-Cu	1.21 ± 0.06	0.20 ± 0.02	6.1
ICN-Co	1.13 ± 0.07	0.35 ± 0.05	3.2

[a] Metal mol % was determined via XPS and is relative to the carbon, nitrogen and oxygen content of the polymer

4.2.5 Analysis of the relationship between metal concentration and mechanical properties

The excellent correlation between the metal concentration gradient and the mechanical gradient observed implies that metal–imidazole interactions cause the strengthening of the material. The mechanical gradient is not linear, which is in line with our previous observation that mechanical properties do not depend linearly on metal to ligand ratio. In our previous study of similar Zn^{2+}–imidazole networks,[34] we observed relatively small mechanical changes for a large range of [imidazole]/[Zn^{2+}] ratio until it approaches ~ 4.0, when a dramatic increase in mechanical properties was observed. In our CGP sample preparation, we aimed to reach [imidazole]/[Zn^{2+}] ~ 4.0 at the end of the sample. The similar dramatic increase in Young's modulus in the very end of the sample suggests that the [imidazole]/[Zn^{2+}] approaches this critical value at the end of the sample. This roughly agrees with the XPS data. As an example, incorporation of the Zn^{2+} into the polymer at [imidazole]/[Zn^{2+}] ratio of 4.0 would give roughly 7.5 mol % Zn^{2+}. The maximal [Zn^{2+}] of 5.1 mol % measured in the bulk sample is close to this amount.

While the same metal concentrations for M-NTf solutions were used for all samples during swelling, the gradient behavior for ICN-M samples differed based on metal selection. ICN-Zn formed a significantly larger gradient than both ICN-Cu and ICN-Co. This agrees with the XPS data, which demonstrates the ICN-Zn had higher metal incorporation across the lateral axis. While the exact reason for this is still unknown, we speculate that it is related to both the coordination geometry and ligand exchange kinetics for different metal–ligand complexes. While Zn^{2+} is known to form only ML_4 complexes with imidazole ligands, Co^{2+} and Cu^{2+} can form six coordinate species.[33,34] Additionally, the ligand exchange kinetics all differ between these metal complexes. Presumably, the higher coordination number and slower ligand exchange kinetics for Co^{2+} and Cu^{2+} hinder the metal uptake and affect network formation. Further studies are currently underway to understand the mechanism for the different behavior.

4.3 Conclusion

In summary, the ICN-Zn network demonstrated in this work represents the largest continuous gradient span in mechanical properties observed to date at over 2 orders of magnitude, representing a dramatic improvement in gradient materials. In addition, using only a two-step synthesis and a common laboratory syringe pump, the ICN-M gradient materials can be reliably produced showing their broad appeal and ease of synthesis. We anticipate that introduction of these types of monodentate, metallopolymer gradients will spur further studies into the biomimetic, dissipative properties of these synthetic materials. With more rigorous engineering control (pull rate, temperature, metal added), we believe materials with much larger mechanical gradients and more homogeneous metal incorporation along the thickness axis could feasibly be obtained. In addition, the flexibility of this system will allow for a variety of different mechanical gradients to be studied using different metals, labile ligands, and/or counterions. Ongoing studies pursuing these goals, as well as gaining more mechanistic insight, are currently being undertaken in our lab.

4.4 References

(1) Weaver, J. C.; Milliron, G. W.; Miserez, A.; Evans-Lutterodt, K.; Herrera, S.; Gallana, I.; Mershon, W. J.; Swanson, B.; Zavattieri, P.; DiMasi, E.; Kisailus, D. *Science.* **2012**, *336* (6086), 1275–1280.

(2) Suresh, S. *Science.* **2001**, *292* (5526), 2447–2451.

(3) Libanori, R.; Erb, R. M.; Reiser, A.; Le Ferrand, H.; Süess, M. J.; Spolenak, R.; Studart, A. R. *Nat. Commun.* **2012**, *3*, 1265.

(4) Ionov, L. *Mater. Today* **2014**, *17* (10), 494–503.

(5) Claussen, K. U.; Scheibel, T.; Schmidt, H.-W.; Giesa, R. *Macromol. Mater. Eng.* **2012**, *297* (10), 938–957.

(6) Claussen, K. U.; Giesa, R.; Schmidt, H.-W. *Polymer.* **2014**, *55* (1), 29–38.

(7) Fox, J. D.; Capadona, J. R.; Marasco, P. D.; Rowan, S. J. *J. Am. Chem. Soc.* **2013**, *135* (13), 5167–5174.

(8) Kim, J.; Mok, M. M.; Sandoval, R. W.; Woo, D. J.; Torkelson, J. M. *Macromolecules* **2006**, *39* (18), 6152–6160.

(9) Wang, Y.-Q.; Wang, Y.; Zhang, H.-F.; Zhang, L.-Q. *Macromol. Rapid Commun.* **2006**, *27* (14), 1162–1167.

(10) Zhang, X.; Hassanzadeh, P.; Miyake, T.; Jin, J.; Rolandi, M. *J. Mater. Chem. B* **2016**, *4* (13), 2273–2279.

(11) Lin, Z.; Gui, X.; Zeng, Z.; Liang, B.; Chen, W.; Liu, M.; Zhu, Y.; Cao, A.; Tang, Z. *Adv. Funct. Mater.* **2015**, *25* (46), 7173–7179.

(12) Wang, B.; Benitez, A. J.; Lossada, F.; Merindol, R.; Walther, A. *Angew. Chemie Int. Ed.* **2016**, *55* (20), 5966–5970.

(13) Yang, L.; Zhang, G.; Zheng, N.; Zhao, Q.; Xie, T. *Angew. Chemie Int. Ed.* **2017**.

(14) Wang, D.; Zhang, H.; Guo, J.; Cheng, B.; Cao, Y.; Lu, S.; Zhao, N.; Xu, J. *Macromol. Rapid Commun.* **2016**, *37* (7), 655–661.

(15) Karabanova, L. V.; Mikhalovsky, S. V.; Lloyd, A. W.; Boiteux, G.; Sergeeva, L. M.; Novikova, T. I.; Lutsyk, E. D.; Meikle, S. *J. Mater. Chem.* **2005**, *15* (4), 499.

(16) Qin, C. L.; Zhao, D. Y.; Bai, X. D.; Zhang, X. G.; Zhang, B.; Jin, Z.; Niu, H. J. *Mater. Chem. Phys.* **2006**, *97* (2–3), 517–524.

(17) Ahmed, A.; Smith, J.; Zhang, H. *Chem. Commun.* **2011**, *47* (42), 11754.

(18) Li, X.; MacEwan, M. R.; Xie, J.; Siewe, D.; Yuan, X.; Xia, Y. *Adv. Funct. Mater.* **2010**, *20* (10), 1632–1637.

(19) Karpiak, J. V.; Ner, Y.; Almutairi, A. *Adv. Mater.* **2012**, *24* (11), 1466–1470.

(20) Chai, H.; Lee, J. J.-W.; Constantino, P. J.; Lucas, P. W.; Lawn, B. R. *Proc. Natl. Acad. Sci.* **2009**, *106* (18), 7289–7293.

(21) Miserez, A.; Schneberk, T.; Sun, C.; Zok, F. W.; Waite, J. H. *Science.* **2008**, *319* (5871), 1816–1819.

(22) Fischer, S. F.; Thielen, M.; Loprang, R. R.; Seidel, R.; Fleck, C.; Speck, T.; Bührig-Polaczek, A. *Adv. Eng. Mater.* **2010**, *12* (12), B658–B663.

(23) Ruggeberg, M.; Burgert, I.; Speck, T. *J. R. Soc. Interface* **2010**, *7* (44), 499–506.

(24) Harrington, M. J.; Waite, J. H. *Adv. Mater.* **2009**, *21* (4), 440–444.

(25) Li, X.; Xie, J.; Lipner, J.; Yuan, X.; Thomopoulos, S.; Xia, Y. *Nano Lett.* **2009**, *9* (7), 2763–2768.

(26) Lowenstam, H. A.; Weiner, S. *On Biomineralization*; Oxford University Press, 1989.

(27) Lowenstam, H. A. *Science.* **1967**, *156* (3780), 1373–1375.

(28) Currey, J. D. *J. Exp. Biol.* **1999**, *202*, 3285–3294.

(29) Lichtenegger, H. C.; Schoberl, T.; Bartl, M. H.; Waite, H.; Stucky, G. D. *Science.* **2002**, *298* (5592), 389–392.

(30) Lichtenegger, H. C.; Schoberl, T.; Ruokolainen, J. T.; Cross, J. O.; Heald, S. M.; Birkedal, H.; Waite, J. H.; Stucky, G. D. *Proc. Natl. Acad. Sci.* **2003**, *100* (16), 9144–9149.

(31) Waite, J. H.; Lichtenegger, H. C.; Stucky, G. D.; Hansma, P. *Biochemistry* **2004**, *43* (24), 7653–7662.

(32) Khan, R. K.; Stoimenov, P. K.; Mates, T. E.; Waite, J. H.; Stucky, G. D. *Langmuir* **2006**, *22* (20), 8465–8471.

(33) Mozhdehi, D.; Ayala, S.; Cromwell, O. R.; Guan, Z. *J. Am. Chem. Soc.* **2014**, *136*, 16128–16131.

(34) Mozhdehi, D.; Neal, J. A.; Grindy, S. C.; Cordeau, Y.; Ayala, S.; Holten-Andersen, N.; Guan, Z. *Macromolecules* **2016**, *49* (17), 6310–6321.

(35) Fischer-Cripps, A. C. *Nanoindentation*; Mechanical Engineering Series; Springer New York: New York, NY, 2011.

4.5 Experimental

General materials and methods: ^{1}H NMR spectra were recorded at 500 MHz. All metal salts were stored and weighed in a nitrogen atmosphere glove box to minimize water absorption and ensure accurate measurements. $Cu(NTf_2)_2$ was purchased from Aldrich. $Zn(NTf_2)_2$ was purchased from Strem Chemicals, Inc. $Co(NTf_2)_2$ was purchased from Alfa Aesar. $Cu(NTf_2)_2$ was obtained in hydrate form and the water content, reported in the Certificate of Analysis (determined by Karl Fischer titration), was used to calculate the molecular weight of the copper hydrate.

For butyl acrylate, inhibitors were removed by passing through basic alumina column prior to polymerization. 1-hydroxycyclohexyl phenyl ketone, technical grade, was used as received.

UV polymerization was performed with a UVP BL-15 longwave UV lamp (P/N 95-0130-01, 0.305 amps, 120 V, 60 Hz) at a distance of approximately 1.5 inches.

The syringe pump used in the CGP was a Fisher Scientific model No. 78-01001.

Synthesis and characterization

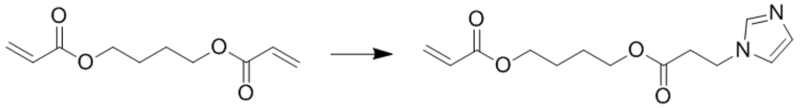

Synthesis of IMZa: The synthesis of IMZa was carried out as previously described and characterization matched previous literature values.[1]

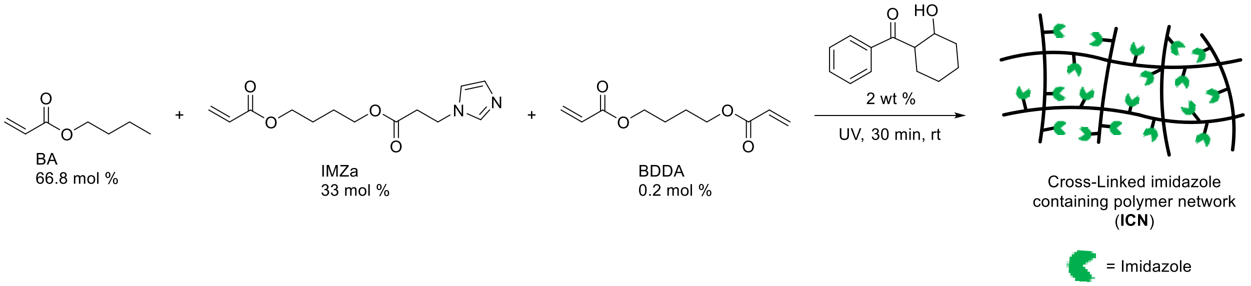

Polymerization of ICN: In a glass vial IMZa (7.44 mmol, 1.98 g, 33 mol%), butyl acrylate (13.7 mmol, 1.76 g, 66.8 mol%), butane diol diacrylate (0.0744 mmol, 0.0147 g, 0.2 mol%), and 1-hydroxycyclohexyl phenyl ketone (0.0751 g, 2 wt% w.r.t. total monomer) were combined. Next, reagents were purged with N_2 for 5 minutes. After purging, a small amount of monomer solution was saved for NMR analysis to determine the exact amount of IMZa in the monomer solution. The purged monomer solution was transferred to a Teflon dish (54 mm x 35 mm x 1.5 mm) and prepolymerized with UV light for 5 minutes. The viscous gel was then covered with a plastic overhead slip and weighted glass sheet, followed by UV irradiation for 30 min. After polymerization, the ICN sheet was peeled from the Teflon mold and plastic sheet, before being stored under vacuum to prevent imidazole oxidation. The mol % of IMZa in ICN was calculated from the monomer mixture via ^{1}H NMR, as the ratio of imidazole peaks to acrylate peaks. The final ICN thickness was 0.8 mm thick. Individual samples were cut to the final dimensions of 3 x 0.8 x 25 mm.

Formation of the Gradient Material: The polymer sample is suspended using tweezers in 90 mL of a stirring acetonitrile solution with the appropriate amount of metal (*vida infra*). The other end of the string is attached to the pusher arm of a syringe pump using tape. Using a 1 mL syringe and tubing, the amount of metal to be added (*vida infra*) is dissolved in an amount of acetonitrile equivalent to the swollen length of the polymer. For example, if the sample is 3 cm long while swollen, the plunger of the syringe (with the tubing attached, to account for the volume of the tubing) is drawn up 3 cm and that volume is used. The added solution concentration can vary slightly due to the adjustment for length for each sample. The end of the tubing is placed in the stirring solution, and the syringe pump is started. The syringe pump was set to a speed that allowed the sample to be slowly pulled up over 2 days. See Image of Apparatus below. After completion, the sample was dried under vacuum at 80 °C overnight.

Calculation of swell solution concentration: Since the mol % of IMZa is known, the mmol of imidazole per length can be determined using the mass and length of the polymer. Using equation S4.1 the total metal needed (in mmol) at length l to form the gradient can be calculated:

Equation S4.1: $Total\ mmol\ metal = \int_{l_f}^{l_i} x\left(y_f - \left(y_f - y_i\right)\frac{l}{l_i}\right) l\, dl$

Where:
x = mmol of IMZa per length
y_f = final metal atoms per IMZa
y_i = initial metal atoms per IMZa
l_i = initial length submerged in solution
l_f = final length submerged in solution

Then using equation S4.2 the initial amount of metal needed can be calculated:

Equation S4.2: $Initial\ mmol\ metal\ needed = x \times y_i \times l_i$

Finally Equation S4.3 is used to determine the amount to add via the syringe:

Equation S4.3: $mmol\ metal\ needed\ in\ syringe = Total\ mmol\ metal - Initial\ mmol\ metal$

Bulk characterization via instrumented indentation procedure of ICN-M samples: The hardness and modulus of elasticity were measured by instrumented indenter (Nanovea, Irvine, CA, USA) using a spherical-conical diamond indenter with tip radius and cone angle of 100 μm and 120° respectively. The depth and compliance of the instrument was calibrated with fused silica prior to testing, and all tests were performed at 40% humidity and 23 °C. In order to stay within the spherical zone of the indenter tip (0-28.5 μm), the applied load was based on the hardness of the sample at each test location. The indentation depth was held constant at 15 μm. The loading rate was based on the applied load so that loading and unloading would each take 30 seconds. The resting period at maximum load was always 2 minutes to reduce the effect of creep on the elastic modulus measurement. The applied load and loading rate ranged from 0.5-20mN and 1-40mN/min respectively. The hardness and elastic modulus were calculated using ASTM E2546 (the Oliver & Pharr method).

Instrumented indentation of preliminary ICN-M samples

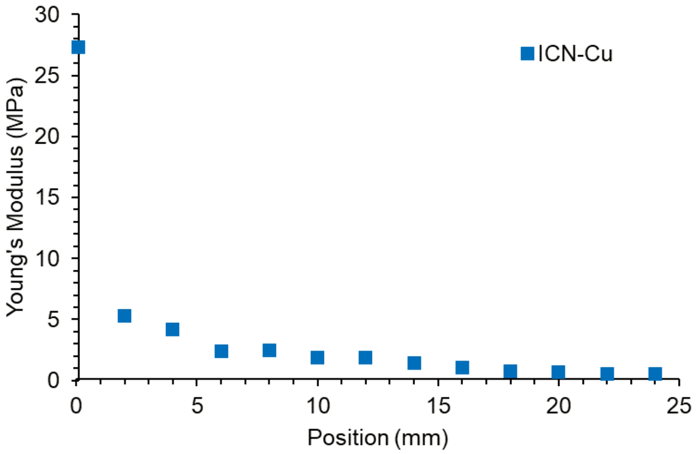

Figure S4.1 Preliminary data for higher metal content (0.1 copper per imidazole initial, 1 copper per imidazole final) ICN-Cu shows weaker ICN-Cu stiffness.

Table S4.1 Young's modulus of ICN-M samples associated with Figure 4.3A

	Young's modulus by Metal (MPa)		
Position (mm)	ICN-Zn	ICN-Cu	ICN-Co
0.1	108 ± 7	46 ± 1	25 ± 2
0.2	59 ± 2	32 ± 3	17.8 ± 0.6
0.4	45 ± 7	20 ± 2	14 ± 1
0.6	29 ± 4	14 ± 1	12.8 ± 0.8
0.8	22 ± 1	7.0 ± 0.6	12 ± 1
1	19 ± 1	4 ± 1	9.5 ± 0.2
1.5	16.3 ± 0.6	3.0 ± 0.1	7.6 ± 0.2
2	7.3 ± 0.6	2.5 ± 0.2	7.2
4	7.1 ± 0.5	1.8 ± 0.3	5.4 ± 0.1
6	4.0 ± 0.4	1.21 ± 0.05	3.52 ± 0.09
8	3.4 ± 0.2	1.05 ± 0.02	1.5 ± 0.2
10	1.49 ± 0.05	0.94 ± 0.01	1.6 ± 0.1
15	1.1 ± 0.1	0.85 ± 0.01	1.15 ± 0.02
20	0.63 ± 0.03	0.70 ± 0.01	0.87 ± 0.02
25	0.59 ± 0.04	0.61 ± 0.01	0.63 ± 0.01
30	0.51 ± 0.02	0.46 ± 0.01	0.52 ± 0.01
34	0.47 ± 0.01	0.38 ± 0.01	0.34 ± 0.01

Hardness data of ICN-M samples

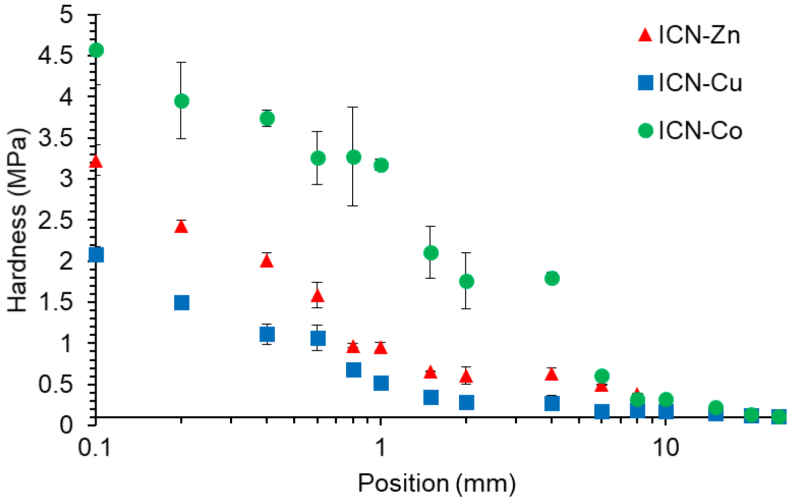

Figure S4.2 Gradient of Hardness along the lateral axis of the samples as determined by instrumented indentation.

Tensile testing: Bulk-M samples were fabricated to confirm that the indentation data represent bulk mechanical properties. Bulk-M samples were prepared as non-gradient bulk samples with identical polymer composition and sample thickness (0.8 mm) to gradient samples. These non-gradient bulk samples were fabricated to mimic the polymer compositions at the stiffest end of the gradient samples ([imidazole]/[M^{2+}] = 4.0). Good agreement between tensile and indenter Young's moduli confirm that the indentation method is reliable for probing the bulk mechanical properties.

The Young's moduli were measured using an Instron 3365 machine in standard stress/strain experiments. The samples were extended at 100 mm/min at room temperature. as follows. Samples were swelled in the appropriate metal/ACN solution at high concentration ([imidazole]/[M^{2+}] = 4.0) for 1 day (sample size: 3 x 0.8 x 10 mm). After swelling, the samples were dried at 80 °C for 1 day.

Table S4.2 Tensile Young's moduli of Bulk-M samples compared to indenter Young's moduli

Sample	Tensile Young's modulus (MPa)	Indenter max. Young's modulus (MPa)
Bulk-Zn	85	108
Bulk-Cu	76	46
Bulk-Co	51	25

XPS procedure: X-ray photoelectron spectra were obtained using a Kratos AXIS Supra device. All measurements were made at a vacuum of < 5 e -7 torr. All samples were mounted to glass microscope slides using double-sided carbon tape. Region scans were obtained using a monochromic aluminum source at an energy of 1486.69 eV, a magnification of 1 e 37, and a resolution of 20. All surfaces were cleaned using GCIS 2000 Ag^+ 5 keV etching over 12 minutes before region scans were collected. Regions scans of the Cu (3/2 2p), Zn (3/2 2p), Co (3/2 2p), O (1s), N (1s), and C (1s) were collected in the ranges of 965-925 eV, 1057-1012 eV, 810-773 eV, 543-525 eV, 410-390 eV, 300-277 eV respectively. Integrated regions from the C, O, N regions, as well as the appropriate metals were divided by their relative sensitivity factor to derive the mol % of each element. Region scans were taken at 1, 3, 8, 13, 18, and 23 mm from the hard end of the sample. Depth profiling studies were carried out using a more powerful GCIS (Ar 2000+ 20 eV) over 100 minutes. Etching was performed for 10 minutes then region scans were performed.

Table S4.3 Tabulated XPS data of figure 3B

Distance from hard end (mm)	mol % Zn[a]	St. Dev. Zn	mol % Cu[a]	St. dev. Cu	mol % Co[a]	St. dev. Co
1	5.1	0.5	1.21	0.06	1.13	0.08
3	4.3	0.4	0.95	0.05	0.92	0.08
8	2.1	0.4	0.74	0.05	0.62	0.07
13	1.8	0.4	0.40	0.03	0.54	0.07
18	1.0	0.4	0.27	0.02	0.42	0.07
23	0.9	0.4	0.20	0.02	0.35	0.05

[a] Relative to mol % of C, O, and N

SEM-EDX Procedure: Energy-dispersive X-ray spectroscopy (EDX) spectra were obtained using a Magellan FEI Scanning electron microscope (SEM) operating at 30 keV and 200 pA and an Oxford silicon drift detector (80 mm^2). All samples were mounted onto SEM stubs using double sided carbon tape and sputter coated with 5 nm of Iridium to ensure good conductivity. Spectra were analyzed using Oxford Instrument's AZtecEnergy software. Normalized weight percent were converted to relative mol % with respect to C, O, N for direct comparison with XPS data. Spectra were taken at 1, 3, 8, 13, 18, and 23 mm from the hard end of the sample on the surface (depth: ~2 μm) and on the cross section (depth: 400 μm).[2]

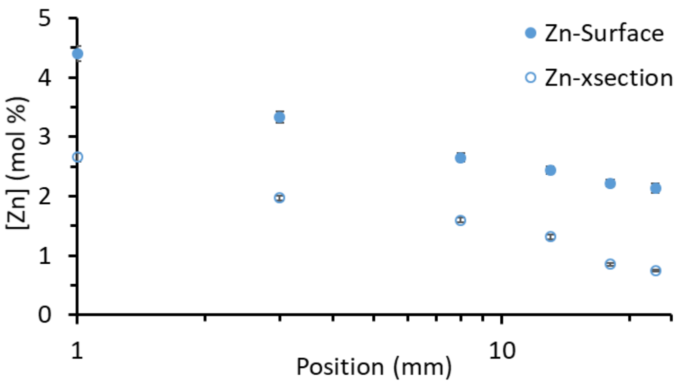

Figure S4.3 SEM-EDX measurement on surface and cross section of ICN-Zn. Cross sectional analysis was performed at the middle of the sample (~0.4 mm).

4.6 References for Experimental

(1) Mozhdehi, D.; Ayala, S.; Cromwell, O. R.; Guan, Z. *J. Am. Chem. Soc.* **2014**, *136*, 16128–16131.

(2) Bertin, E. P. *Principles and Practice of X-Ray Spectrometric Analysis*; Springer US: Boston, MA, 1975.

4.7 Chapter 4 Spectra

Monomer mixture from ICN polymerization. ^{1}H NMR (500 MHz, $CDCl_3$, 298 K). IMZa peak at 7.0 ppm was compared to BA peak at 0.9 ppm to determine IMZa percentage.

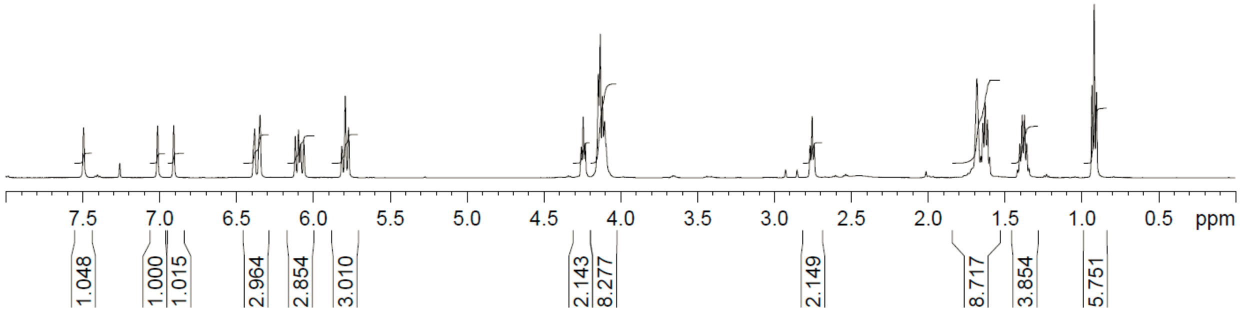

Chapter 5: Progress Towards Silyl Ether Vitrimers for Commodity Polymers

5.1 Introduction

5.1.1 The current state of vitrimer materials

Thermoset materials are strong, creep resistant, operable over a wide range of temperatures, and resilient to chemical attack. These traits come from covalent crosslinks that hold polymer chains together. These same crosslinks limit the material's ability to flow, leading to reprocessing issues. This limited flow makes these materials impossible to reshape, and therefore, unattractive for commercial use due to the environment impact of single-use plastics. On the other hand, thermoplastics are easy to process because they do not have crosslinks, but they are limited by low strength and failure at high temperatures. Incorporating dynamic crosslinks into a polymeric material provides an avenue to take the best traits of each material.

Vitrimers contain latent crosslinks that are static at service temperatures, but become dynamic at elevated temperature. The field of vitrimer materials has grown since 2011 and include dynamic crosslinks based on a variety of different motifs. These include silyl ether,[1] ester,[2–5] urethane,[6–9] triazolium salts[10], and frustrated Lewis pairs.[11] For vitrimers to become a material for everyday use they must address multiple challenges. First, they must be compatible with commercially relevant polymers such as polystyrene (PS), polyethylene (HDPE), and poly(methyl methacrylate) (PMMA). Second, they must process under conditions similar to thermoplastics for ease of preparation with existing machinery. Third, the dynamic motif must be robust over a range of conditions (time and temperature) so that the ability to reprocess withstands multiple “lifecycles.” To date, no vitrimer system has fulfilled all three of these requirements.

5.1.2 Our design for high performance vitrimers

We have focused on a silyl ether motif to achieve a vitrimer that is robust over a wide range of processing times and temperatures. Si–O bonds are thermally stable and appear in materials ranging from soft polydimethylsiloxane to brittle silicate glass. Additionally, the rate of silyl ether exchange is known to vary based on the catalytic environment of the system in bulk.[1] Herein, we report progress towards the development of a high performance vitrimer that relies on silyl ether exchange (Figure 5.1). Specifically, we envision the incorporation of silyl ether motifs into the backbone of commercial polymers and subsequent crosslinking via catalyst-mediated metathesis with a di-functional silyl ether molecule (1).

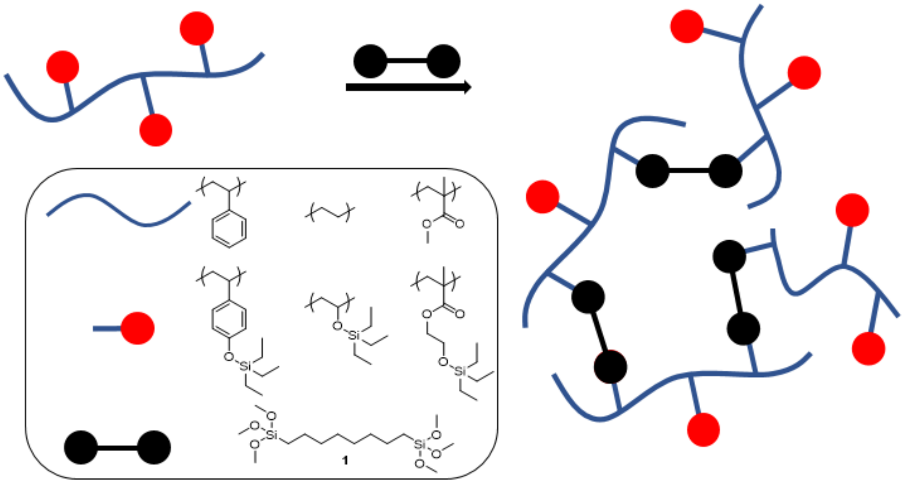

Figure 5.1 Design concept for silyl ether vitrimers. Commercially-relevant backbones, functionalized with silyl ether motifs, are mixed with di-functional crosslinker **1**.

5.2 Results and Discussion

5.2.1 Small molecule proof-of-concept

Silyl ether metathesis was identified as an exciting motif for vitrimeric properties for multiple reasons. First, Si-O bonds are thermally and oxidatively stable. Second, the lack of alcohol in the system minimizes the chance for unwanted side reactions. Specifically, primary alcohols undergo thermal dehydration at elevated temperatures and can react with PMMA backbones to irreversibly crosslink a material. Third, direct silyl ether exchange results in cleaner chemistry and minimizes the amount of "designer monomers" needed in the system.

To understand the possibilities of a silyl ether exchange reaction, a small molecule proof-of-concept was carried out. First, we prepared two, low molecular weight silyl ether molecules ($SiBu_3$ and $SiPn_3$) via alcoholysis of trichloroethylsilane. These silyl ethers were dissolved in dimethylacetamide under anhydrous conditions and mixed in the presence of catalyst (5 mol%). For the initial investigation, two lewis acids ($Zn(OTf)_2$ and $Sc(OTf)_3$) and two Bronsted acids (camphor sulfonic acid [CSA] and cyclohexanecarboxylic acid [cHCA]) were tested. The metathesis reaction was carried out for various times and temperatures, and followed via gas chromatography-mass spectrometry (GC-MS) (Figure 5.2a). No free alcohol species was observed under any reaction condition. Complete equilibrium is attained when the reaction reaches 1:3:3:1 product distribution.

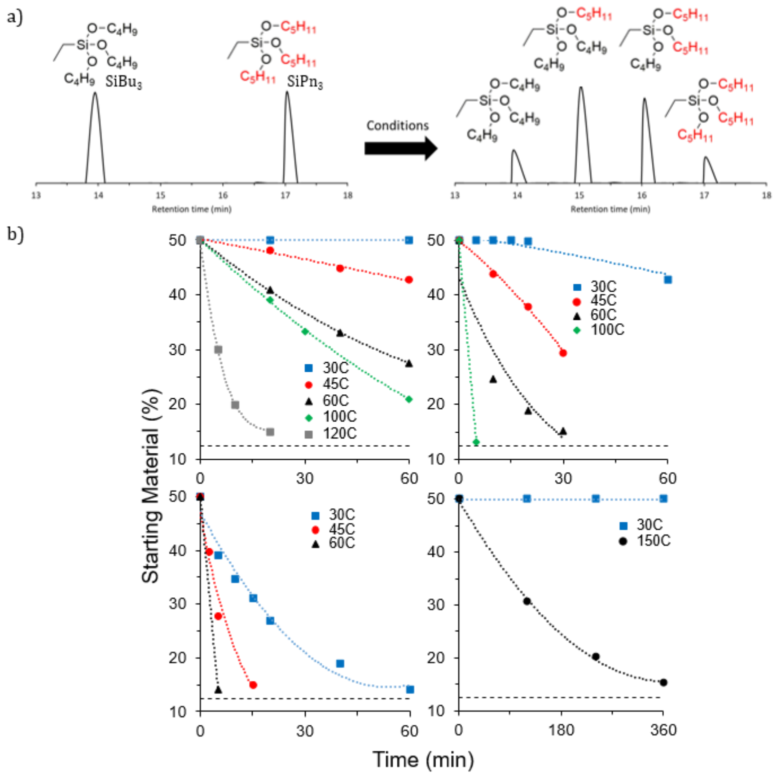

Figure 5.2 Small molecule study of silyl ether exchange. (A) Representative gas chromatography-mass spectrometry (GC-MS) of metathesis reaction between equimolar $SiBu_3$ and $SiPn_3$. Complete exchange reaches 1:3:3:1 stoichiometry. (B) GC-MS data of catalyst-mediated (5 mol%) silyl ether exchange at various times and temperatures. Catalysts studied: $Zn(OTf)_2$ [top left], $Sc(OTf)_3$ [top right], CSA [bottom left], cHCA [bottom right].

The metathesis reaction shows wide tunability based on catalyst selection (Figure 5.2b). Full equilibrium can be reached under numerous time and temperature conditions. CSA displayed the highest catalyst activity, nearly reaching equilibrium in 1 h at 30 °C or in 5 min at 60 °C. In contrast, cHCA displayed the lowest activity, requiring 6 h at 150 °C to nearly reach equilibrium. Interestingly, the Lewis acid catalysts demonstrated a wider temperature window to tune the reaction. For example, the zinc catalyst showed moderate activity between 40 °C and 120 °C. cHCA was not studied further due to its diminished catalytic activity.

5.2.2 Polymer synthesis and catalyst incorporation

After completion of the preliminary small molecule screening, the silyl ether motif was evaluated in bulk PS. PS was selected as an initial target due to its ease of synthesis, commercial relevance, and the belief that the aromatic side chain would limit the chance of side reactions. First, a silyl ether-functionalized styrene monomer (StyOS) was synthesized via two-step hydrolysis and silane condensation of 4-vinylbenzyl chloride (Scheme 5.1a). Next, radical polymerization of styrene and StyOS was carried to yield poly(Sty-StyOS) with 10 mol% incorporation of StyOS monomer (Scheme 5.1b). Poly(Sty-StyOS) was characterized via ^{1}H NMR and gel permeation chromatography (Table 5.1)

Scheme 5.1 Synthesis of (a) StyOS and (b) polymerization of poly(Sty-StyOS)

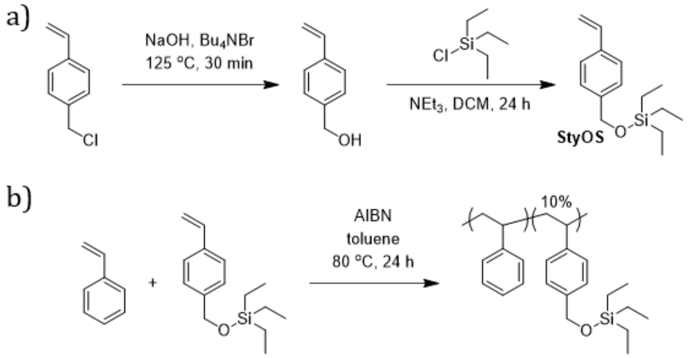

Table 5.1 Molecular characterization of poly(Sty-StyOS)

sample	mol % StyOS^a	$M_n{}^b$ (kDa)	$M_w/M_n{}^b$
poly(Sty-StyOS	10	15.9	1.93

^{a}Estimated from ^{1}H NMR. ^{b}Estimated from gel permeation chromatography using polystyrene standards in DMF.

To initially probe the behavior of this system in bulk, poly(Sty-StyOS) was crosslinked with 1 and various amounts of catalysts were added. Briefly, samples were prepared via dissolution of poly(Sty-StyOS), catalyst, and 1 in minimal amounts of dry acetone. Next, the solutions were homogeneously mixed and acetone was removed *in vacuo* at 40 °C for 3 h. Finally, the polymer sample was processed with a hot press at varying temperatures. Unfortunately, under all tested conditions the samples containing zinc and scandium catalysts displayed severe side reactions that discolored and irreversibly crosslinked the material (data not shown).

5.2.3 Vitrimer behavior of CSA catalyzed poly(Sty-StyOS)

An ideal vitrimer undergoes no side reactions and is processable above topology freezing transition temperature (T_V). To optimize the silyl ether vitrimer, the amounts of **1** and CSA were varied. Each sample was pressed at 125 °C for a selected amount of time and then fractured into small pieces. One small piece (~30 mg) was analyzed via gel fraction analysis to quantify the amount of crosslinking. Gel fraction refers to the amount of sample remaining after submersion in xylenes for > 12 h (100% gel fraction = 100% crosslinked). The remaining small pieces were pressed again at 125 °C in an attempt to reprocess the material and qualitatively analyze the reprocessability of the material.

To explore the relationship between amount of **1** and crosslink density, the amount of CSA was held constant at 0.25 mol % (with respect to total monomer repeats) and the amount of crosslinker was varied between 1-5 mol %. The samples were processed at 125 °C for 5, 15, and 30 min (Figure 5.3a). This data shows the clear, and expected, direct correlation between incorporation of **1** and amount crosslinked. Interestingly, the gel fraction increases over processing time. This points to two possiblities: first, the reaction between crosslinker **1** and the polymer backbone proceeds for > 30 min, or second, a side reaction leads to unwanted crosslinking over time.

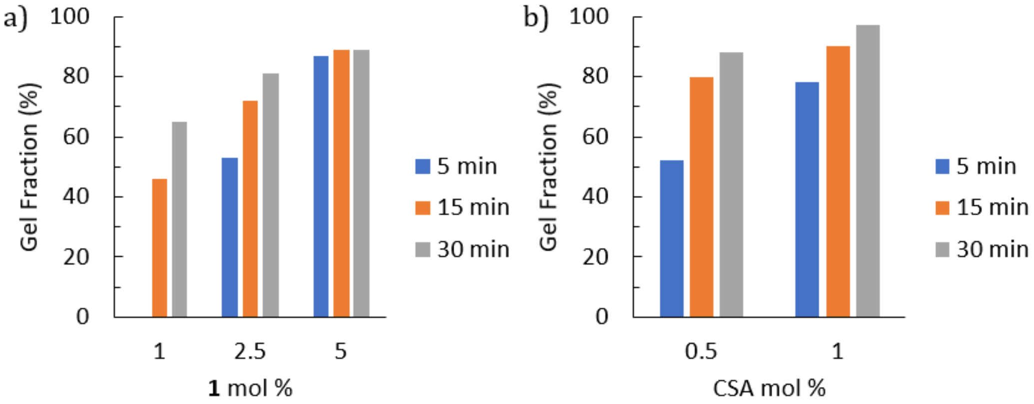

Figure 5.3 Gel fraction analysis. Quantification of poly(Sty-StyOS) crosslinking of samples pressed at 125 °C for 5, 15, and 30 min. (A) Samples contain 0.25 mol % CSA and varying amounts of crosslinker 1. (B) Samples contain 2.5 mol % 1 and varying amounts of CSA.

To further elucidate the vitrimeric behavior of poly(Sty-StyOS), the amount of **1** was held constant at 2.5 mol % and the CSA was incorporated at 0.5 and 1 mol % (Figure 5.3b). This experiment shows the trend that increased incorporation of catalyst leads to faster crosslinking. Again, this could point to the slow reaction time of poly(Sty-StyOS) with **1** in bulk or the presence of a side reaction. For both experiments mentioned above, it was observed that gel fraction > 85% lead to inhomogeneous reprocessability. Next, a study with reduced melt pressing times was completed to assess if reprocessability with between 70-80% gel fraction could be achieved.

Poly(Sty-StyOS) samples were incorporated with 2.5 mol % 1 and CSA incorporation of 0.75% and 1.0%. Samples were pressed at 125 °C for various time points between 1-8 min (Figure 5.4). Both samples displayed similar behavior with gel fraction near 75% after ~3 min. Unfortunately, these materials were not able to be reprocessed after 3 min. The diminished dynamics of the silyl ether crosslink after short processing times points to an irreversible side reaction. This side reaction could be due to an interaction between PS backbone and CSA or a hydrolysis reaction due to the hygroscopic nature of acetone.

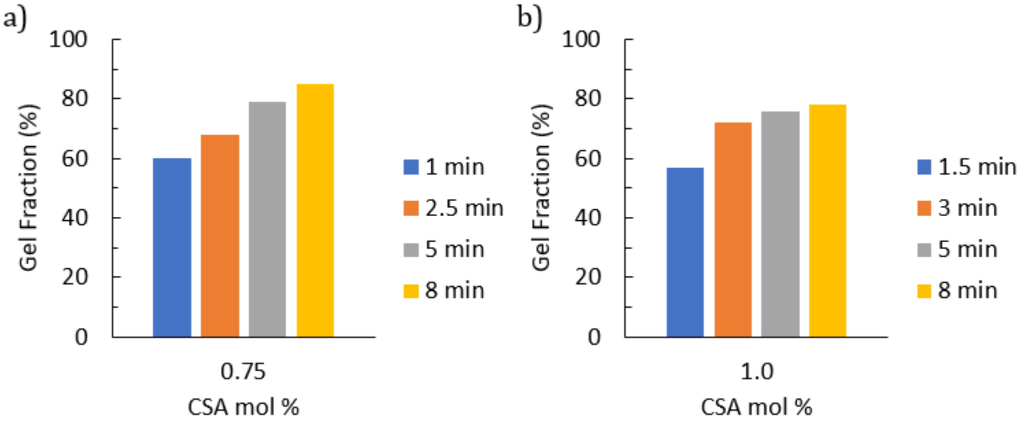

Figure 5.4 Refined gel fraction analysis. Quantification of poly(Sty-StyOS) crosslinking of samples containg 2.5 mol % 1 and pressed at 125 °C for various times. (A) Samples contain 0.75 mol % CSA. (B) Samples contain 1.0 mol % CSA.

5.3 Troubleshooting and future directions

The presence of a side reaction between CSA and PS has not been confirmed. One route to assess the presence of a side reaction would be to submerge the sample in excess methanol. Methanol would cleave the silyl ether crosslinks, but is unlikely to interact with other side reaction products. Additionally, researchers should also assess the crosslinking behavior of **1** with CSA in the presence of a different silyl ether containing polymer. HDPE would be an excellent choice for this study because the less reactive covalent C-C and C-H bonds would limit the chance of unwanted reactivity. We propose the synthesis of HDPE-OS from commercially available poly(ethylene-co-vinyl acetate) (EVA). Specifically, we propose the conversion of EVA to HDPE-OS via hydrolysis of acetate and subsequent alcoholysis of chlorotriethylsilane (Scheme 5.2).

Scheme 5.2 Proposed synthesis of HDPE-OS

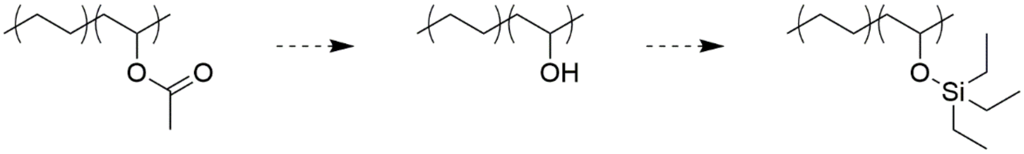

An additional possibility from unwanted side reaction comes from the preparation of silyl ether vitrimers with acetone. It is possible that some atmospheric water is scavenged by acetone during sample preparation, leading to eventual silyl ether hydrolysis and side reaction. To limit the potential issue of silyl ether hydrolysis, we propose the switch of solvents to anhydrous dichloromethane (DCM). DCM is considerably less hygroscopic than acetone. The initial study was not carried out with DCM due to solubility issues with some catalysts.

In conclusion, a silyl ether vitrimer for commodity polymers has the potential to disrupt the thermoset industry. The combination of materials that are strong, creep resistant, and operable over a wide range of temperatures, while combined with the convenient processing conditions of thermoplastics is an attractive proposition that should be pursued vigorously by polymer scientists. Unfortunately, progress towards silyl ether vitrimers has been impeded by the unknown cause for irreversible crosslinking reactions. If manipulation of preparation conditions and polymer backbone do not solve this issue, it may be necessary to identify alternative catalysts for silyl ether metathesis.

5.4 References

(1) Nishimura, Y.; Chung, J.; Muradyan, H.; Guan, Z. *J. Am. Chem. Soc.* **2017**, *139* (42), 14881–14884.

(2) Montarnal, D.; Capelot, M.; Tournilhac, F.; Leibler, L. *Science.* **2011**, *334* (6058), 965–968.

(3) Brutman, J. P.; Delgado, P. A.; Hillmyer, M. A. *ACS Macro Lett.* **2014**, *3* (7), 607–610.

(4) Yang, Y.; Pei, Z.; Li, Z.; Wei, Y.; Ji, Y. *J. Am. Chem. Soc.* **2016**, *138* (7), 2118–2121.

(5) Capelot, M.; Montarnal, D.; Tournilhac, F.; Leibler, L. *J. Am. Chem. Soc.* **2012**, *134* (18), 7664–7667.

(6) Denissen, W.; Rivero, G.; Nicolaÿ, R.; Leibler, L.; Winne, J. M.; Du Prez, F. E. *Adv. Funct. Mater.* **2015**, *25* (16), 2451–2457.

(7) Fortman, D. J.; Brutman, J. P.; Cramer, C. J.; Hillmyer, M. A.; Dichtel, W. R. *J. Am. Chem. Soc.* **2015**, *137* (44), 14019–14022.

(8) Zheng, N.; Fang, Z.; Zou, W.; Zhao, Q.; Xie, T. *Angew. Chemie Int. Ed.* **2016**, *55* (38), 11421–11425.

(9) Liu, W.-X.; Zhang, C.; Zhang, H.; Zhao, N.; Yu, Z.-X.; Xu, J. *J. Am. Chem. Soc.* **2017**, *139* (25), 8678–8684.

(10) Obadia, M. M.; Mudraboyina, B. P.; Serghei, A.; Montarnal, D.; Drockenmuller, E. *J. Am. Chem. Soc.* **2015**, *137* (18), 6078–6083.

(11) Wang, M.; Nudelman, F.; Matthes, R. R.; Shaver, M. P. *J. Am. Chem. Soc.* **2017**, *139* (40), 14232–14236.

5.5 Experimental

General materials and methods: ^{1}H and ^{13}C NMR spectra were recorded at 500 MHz and 125 MHz Bruker Instruments, respectively. Chemical shifts were reported in standard format as values in ppm relative to the signal of deuterated solvents. Gel permeation chromatography (GPC) was performed in DMF (1 mL/min) using an Agilent LC 1100 Series equipped with Agilent 5 μm mixed-C column to determine molecular weights and molecular weight distributions, M_w/M_n, with respect to polystyrene standards.

All chemicals were used as received unless otherwise stated. For styrene monomer, inhibitors were removed via vacuum distillation. Anhydrous solvents were purified through a column of alumina according to the method described by Pangborn *et al* before use.[1] Anhydrous acetone was obtained from Acros Organics 99.8%, extra dry, acroseal®.

Thin layer chromatography plates were stained by $KMnO_4$ for presence of double bonds. The monomer was purified using CombiFlash® Rf+ automatic column as described in the monomer synthesis section.

Synthesis and characterization

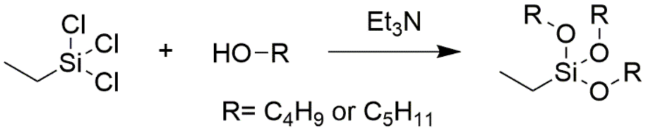

SiBu$_3$: R=C$_4$H$_9$ SiPn$_3$: R=C$_5$H$_{11}$

Representative synthesis of silanes (SiBu$_3$ shown). Under nitrogen, butanol (7.41 g, 5 eq, 100 mmol), triethylamine (10 g, 5 eq, 100 mmol), and toluene (30 mL) were charged into a two-neck, flame-dried flask. The flask was cooled to 0 °C and trichloroethylsilane (2.64 mL, 1 eq, 20 mmol) was slowly added. Next, the reaction was refluxed at 115 °C for 3 h. After cooling, the reaction mixture was filtered to remove the ammonium salt and the excess alcohol was removed via rotary evaporation. The crude reaction mixture was purified by distillation (butanol oil bath: 111 °C; pentanol oil bath: 130 °C) under high vacuum to yield SiBu$_3$ as a clear liquid (3.53 g, 64% yield). The identity of the product was confirmed by ^{1}H NMR and ^{13}C NMR.

SiBu$_3$ ^{1}H NMR (500 MHz, CDCl$_3$) δ 3.74 (t, J=6.7, 6H), 1.55 (m, 6H), 1.37 (sxt, J=7.6, 6H), 0.99 (t, J=8.0, 3H), 0.92 (t, J=7.4, 9H), 0.61 (q, J=8.0, 2H) ^{13}C NMR (125 MHz, CDCl$_3$) δ 62.60, 34.83, 19.07, 14.00, 6.70, 2.33.

SiPn$_3$ ^{1}H NMR (500 MHz, CDCl$_3$) δ 3.73 (t, J=6.8, 6H), 1.57 (m, 6H), 1.32 (m, 12H), 0.99 (t, J=8.0, 3H), 0.90 (m, 9H), 0.62 (q, J=8.0, 2H). ^{13}C NMR (125 MHz, CDCl$_3$) δ 62.92, 32.42, 28.10, 22.62, 14.21, 6.70, 2.33.

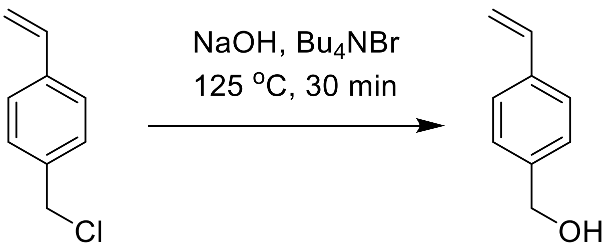

Synthesis of StyOH. The synthesis was adapted from a previously described procedure.[2] Tetrabutylammonium bromide (6.5 g, 1 eq, 20 mmol) and sodium hydroxide (0.08 g, 0.1 eq, 2 mmol) were dissolved in H_2O. To this solution, 4-vinylbenzyl chloride (3.05, 20 mmol) was added and the mixture was heated to reflux at 125 °C. After 30 min, the reaction was cooled to 0 °C and extracted with EtOAC (3 x 100 mL). After extraction, the combined organic layers were dried with $MgSO_4$, filtered, and concentrated *in vacuo*. The crude reaction was purified by column chromatography (0:100 – 30:70 ethyl acetate:hexanes) to yield a colorless oil (2.26 g, 74% yield). The identity of the product was confirmed by ^1H NMR and ^{13}C NMR.

^1H NMR (500 MHz, $CDCl_3$) δ 7.31-7.42 (m, 4H), 6.69-6.75 (m, 1H), 5.74-5.77 (m, 1H), 5.26 (m, 1H), 4.67 (s, 2H), 1.77 (s, 1H). ^{13}C NMR (125 MHz, $CDCl_3$) δ 143.37, 137.86, 137.24, 127.73, 126.98, 113.65, 64.55.

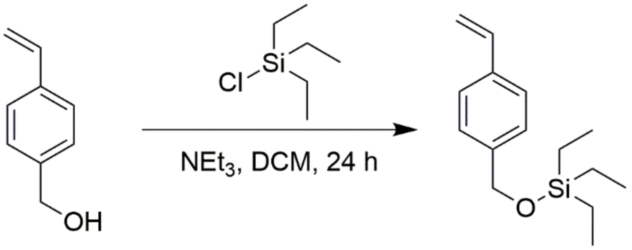

Synthesis of StyOS. Under nitrogen, a solution of StyOH (3.3 g, 1 eq, 25 mmol) in anhydrous DCM (100 mL) was cooled to 0 °C. To this solution, triethylamine (3.98 g, 1.6 eq, 39.4 mmol) was added, followed by slow addition of chlorotriethylsilane (5.56 g, 1.5 eq, 36.9 mmol). The reaction was allowed to slowly warm to room temperature and stirred for 24 h. Next, the reaction was diluted with DCM (100 mL) and washed with H_2O (3 x 100 mL). The organic layer was then dried with $MgSO_4$, filtered, and concentrated *in vacuo*. The crude reaction was purified by column chromatography (0:100 – 15:85 ethyl acetate:hexanes) to yield a colorless oil (5.28 g, 86% yield). The identity of the product was confirmed by ^{1}H NMR and ^{13}C NMR.

^{1}H NMR (500 MHz, $CDCl_3$) δ 7.29-7.39 (m, 4H), 6.69-6.74 (m, 1H), 5.72-5.75 (m, 1H), 5.21-5.23 (m, 1H), 4.73 (s, 2H), 0.98 (t, J=8.0 Hz, 9H), 0.66 (q, J=8.0 Hz, 6H). ^{13}C NMR (125 MHz, $CDCl_3$) δ 141.16, 136.85, 136.52, 126.54, 126.26, 113.47, 64.67, 6.93, 4.66.

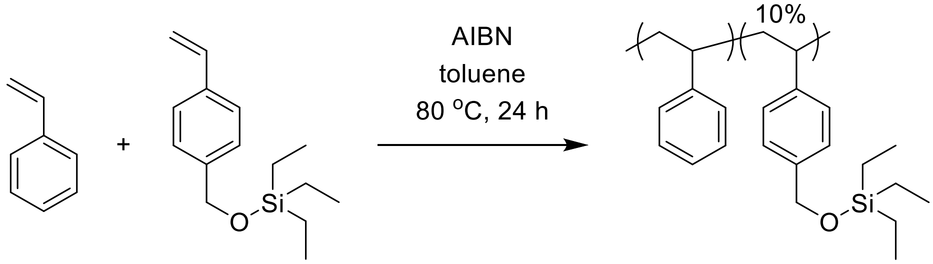

Representative polymerization of poly(Sty-StyOS): Styrene was purified via vacuum distillation before use. Styrene (17.14 g, 164.5 mmol), StyOS (5.31 g, 21.38 mmol), and toluene (25.82 mL) were charged into a Schlenk flask. Next, azobisisobutyronitrile (0.181 g, 1.12 mmol) and anisole (4 mL), as an internal standard, were added to the reaction vessel. The polymerization was carried out with a monomer:initiator ratio of 166:1 at a concentration of 7.2 M. After combination of the reagents, the vessel was sparged with nitrogen for 45 min. Next, an initial aliquot was taken and the vessel was sealed and stirred at 80 °C for 25 h. Polymerization progress was monitored via ^{1}H NMR by comparing the -CH_3 of anisole to the vinyl styrene protons. After 25 h, the reaction was diluted with toluene (25 mL) and precipitated into methanol (1000 mL). Finally, the polymer was dissolved in toluene (70 mL) and precipitated once more from methanol (1000 mL). After drying *in vacuo* overnight, the purified polymer was characterized via ^{1}H NMR and gel permeation chromatography (14.54 g, 10% StyOS).

^{1}H NMR (500 MHz, C_2D_2) δ 6.32-7.35 (m, 52H), 4.55-4.65 (m, 2H), 1.70-2.3 (m, 8H), 1.25-1.70 (m, 19H), 1.00 (br. s, 9H), 0.68 (br. s, 6H).

GPC (DMF eluent, PS standard) M_n: 15,900; M_W/M_n: 1.93.

Representative poly(Sty-StyOS) crosslinking procedure: To form a vitrimer, poly(Sty-StyOS) was mixed with crosslinker 1 and camphor sulfonic acid (CSA) in flame dried flasks under dry N_2. Poly(Sty-StyOS) (0.75 g) was dissolved in anhydrous acetone (3 mL). Next, CSA (1 mol %, 0.018 g) was dissolved in dry acetone (0.5 mL). Finally, crosslinker 1 (2.5 mol %, 0.056 g, 0.057 mL) was combined with the polymer solution and CSA solution was subsequently added. After homogeneous mixing, the solution was quickly transferred to a Teflon evaporation dish and placed in a vacuum oven (containing desiccant) at 40 °C. Acetone was slowly removed *in vacuo* and left to dry for 3 h. The resulting brittle film was broken into pieces and ready for processing.

Representative processing procedure: Vitrimer samples were press with a Specac West 6100+ High Temperature Hot Press. Samples were manually broken into small pieces and placed between preheated Teflon molds at 125 °C. The press was pressurized to 2 tons of force and the sample was heated for various times. After pressing, samples were quickly cooled to 100 °C and removed from the mold to cool to ambient conditions. After cooling, the sample was visually inspected for homogeneity and a small piece (~30 mg) was collected for gel fraction analysis.

Gel fraction analysis: A 30 mg polymeric sample was collected and added to a tared vial. Next, excess xylenes (~2.5 mL) was added and the sample was submerged under ambient conditions for > 12 h. After submersion, the xylene solution was decanted via pipet so that only the organic gel remained. The organogel was dried *in vacuo* at 125 °C overnight. The mass of the remaining dried solid was obtained and gel fraction calculated.

$$Gel\ Fraction = \frac{mass_{dried}}{mass_{original}} * 100$$

5.6 References for Experimental

(1) Pangborn, A. B.; Giardello, M. A.; Grubbs, R. H.; Rosen, R. K.; Timmers, F. J. *Organometallics* **1996**, *15* (5), 1518–1520.

(2) He, R.; Toy, P. H.; Lam, Y. *Adv. Synth. Catal.* **2008**, *350* (1), 54–60.

5.7 Chapter 5 Spectra

SiBu$_3$. ^{1}H NMR (500 MHz, CDCl$_3$, 298 K)

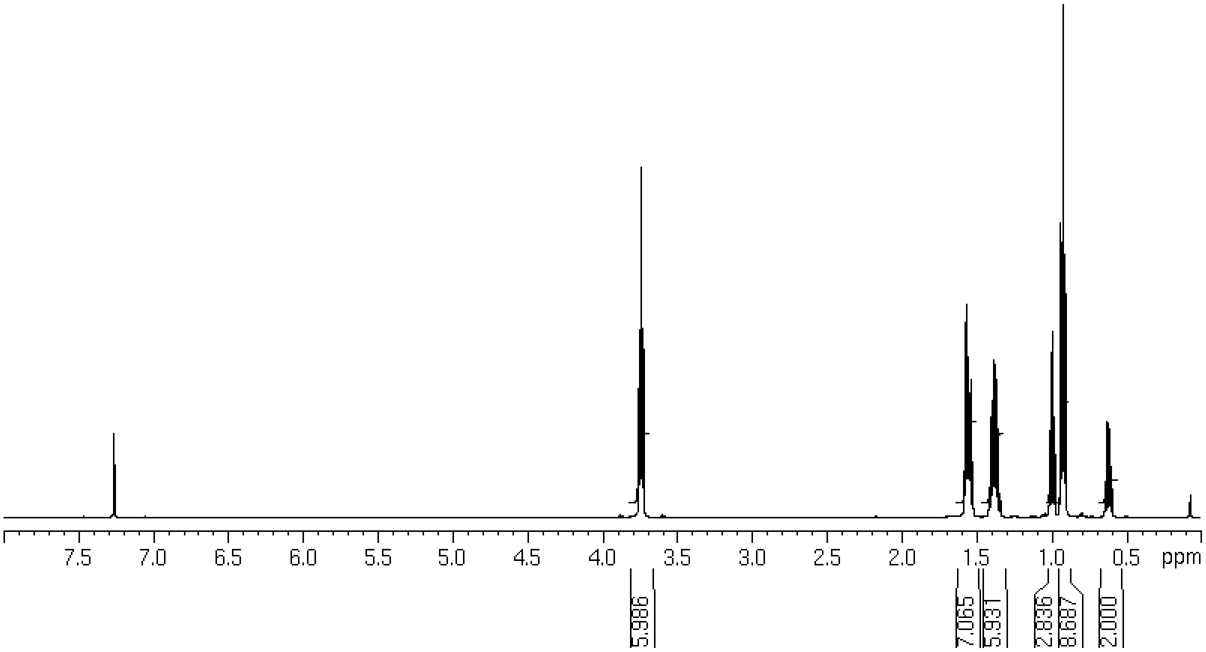

SiBu$_3$. ^{13}C NMR (125 MHz, CDCl$_3$, 298 K)

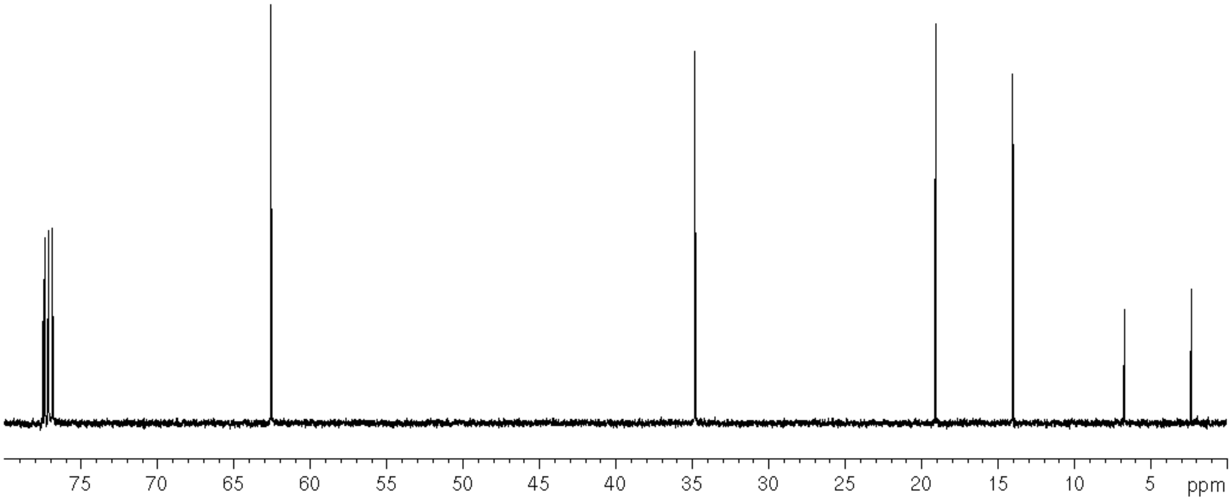

SiPn$_3$. ^{1}H NMR (500 MHz, CDCl$_3$, 298 K)

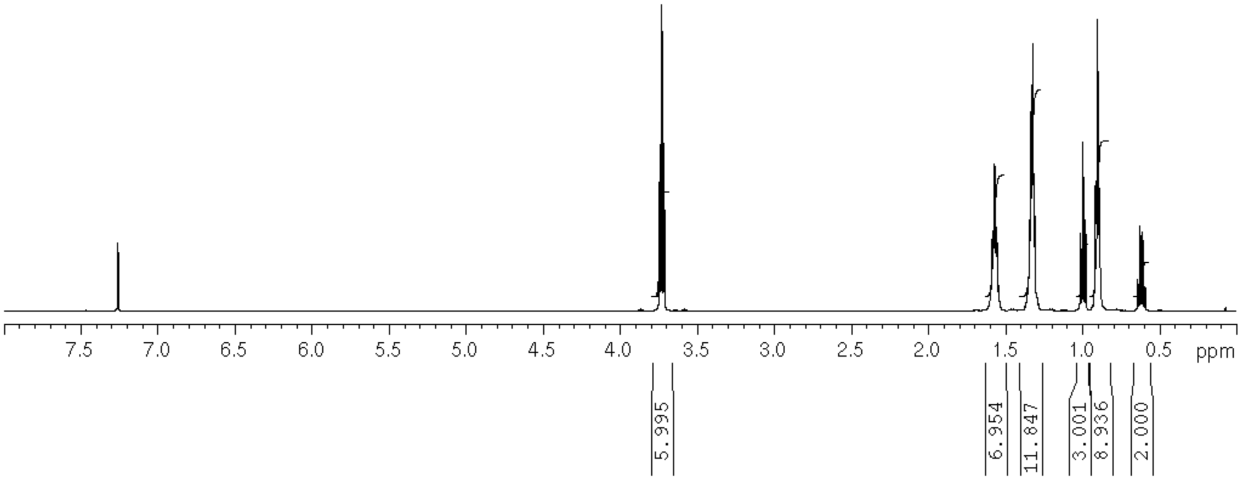

SiPn$_3$. ^{13}C NMR (125 MHz, CDCl$_3$, 298 K)

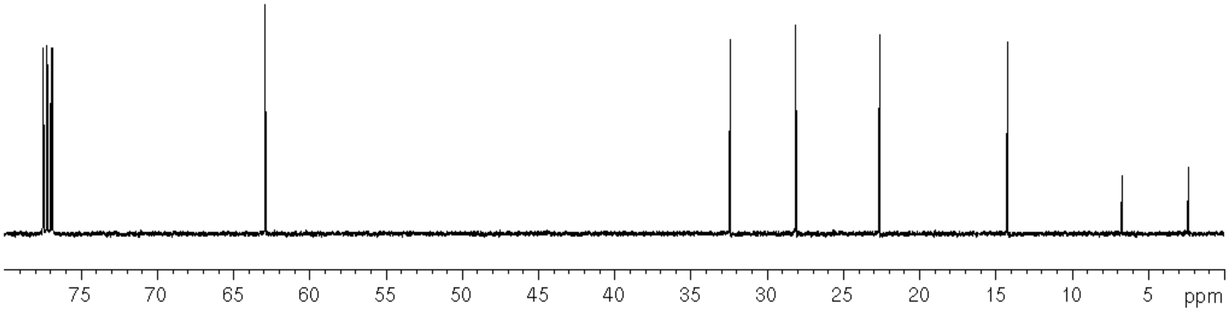

StyOH. ^{1}H NMR (500 MHz, CDCl$_3$, 298 K)

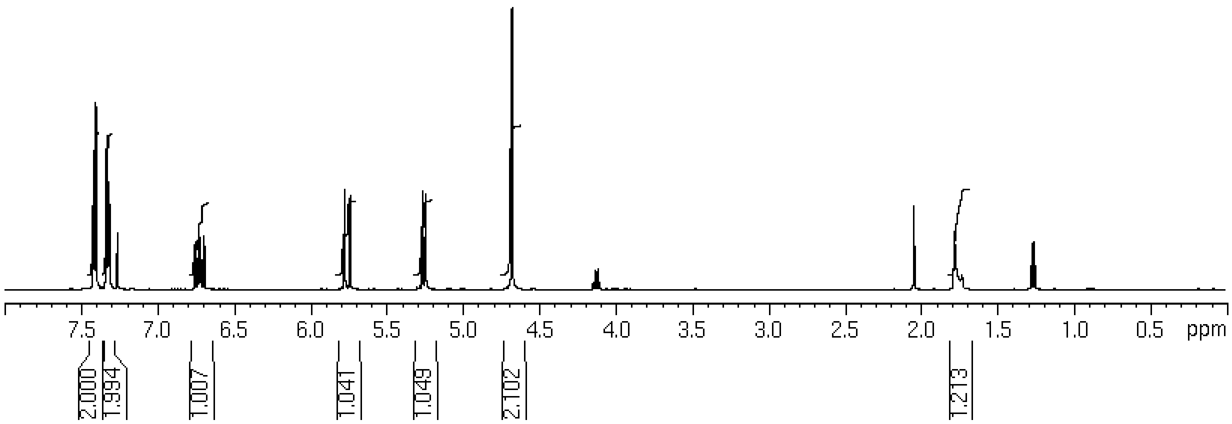

StyOH. ^{13}C NMR (125 MHz, CDCl$_3$, 298 K)

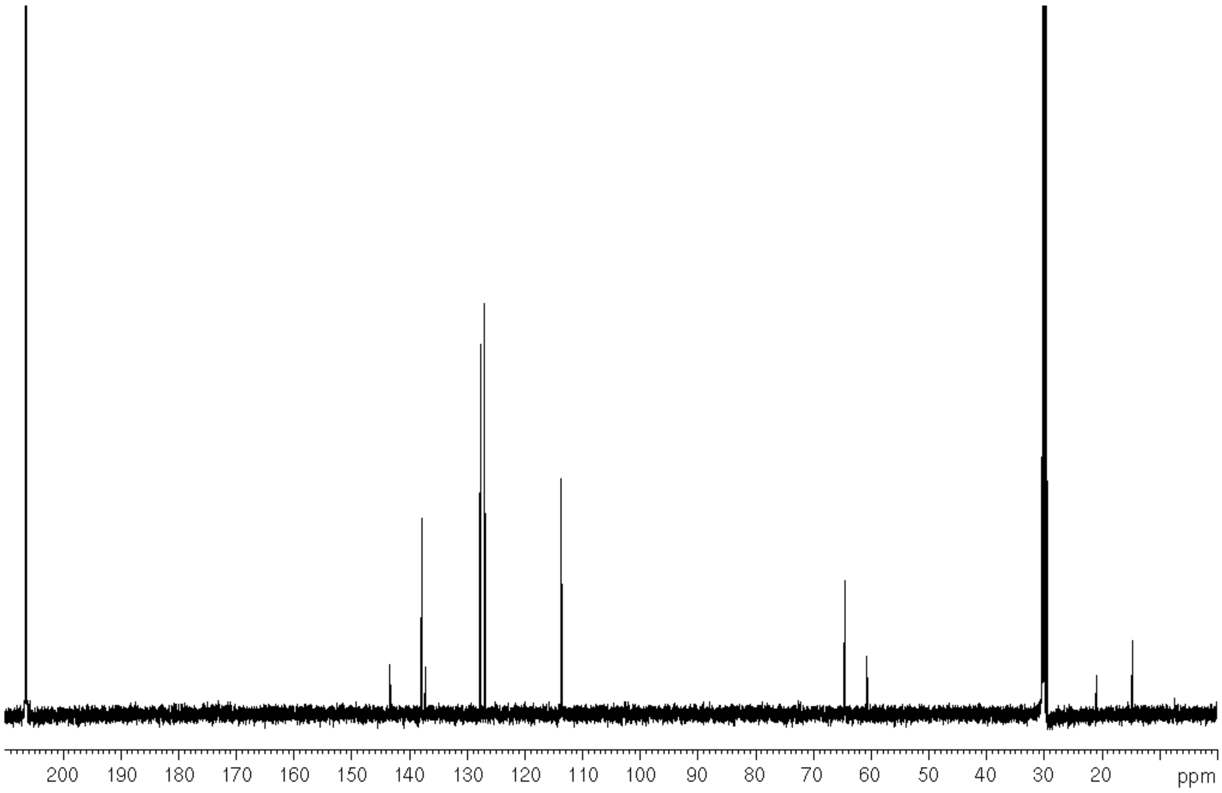

StyOS. ^{1}H NMR (500 MHz, CDCl$_3$, 298 K)

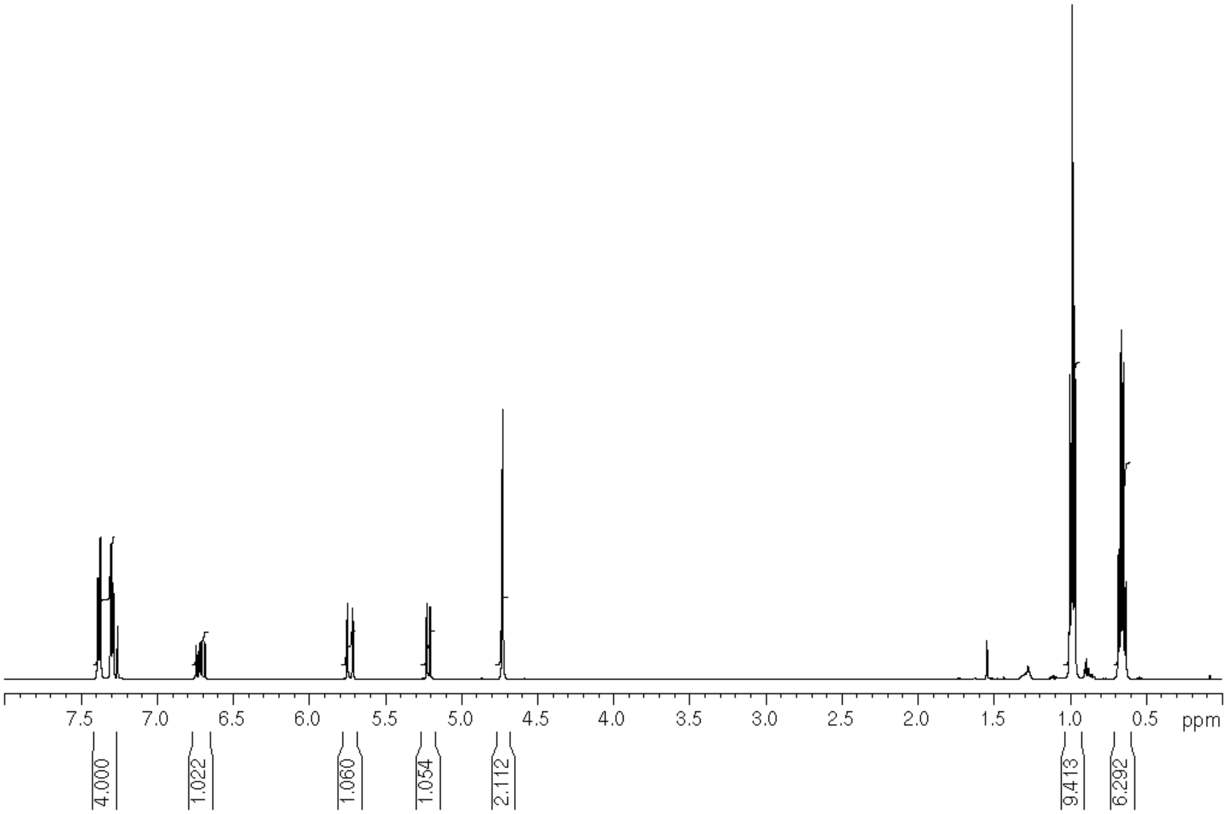

StyOS. ^{13}C NMR (125 MHz, CDCl$_3$, 298 K)

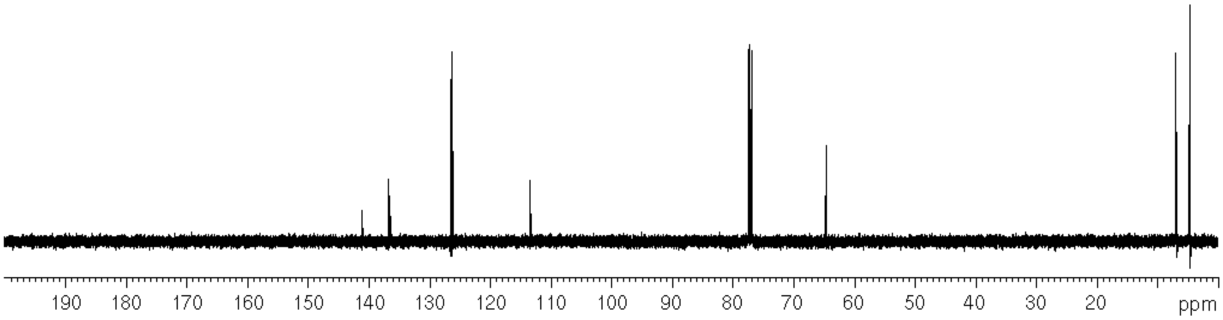

Poly(Sty-StyOS). ^{1}H NMR (500 MHz, C_2D_2, 298 K)

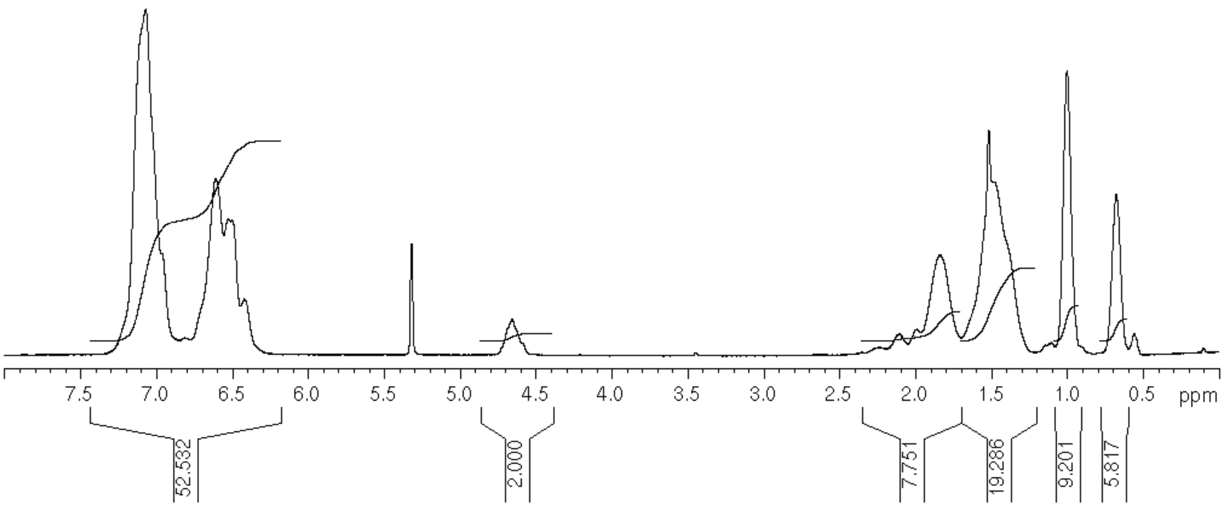

GPC Trace of poly(Sty-StyOS). GPC (DMF eluent, PS standard) M_n: 15,900 M_w/M_n: 1.93